UNIVERSITY OF SOUTHAMPTON

Intrusions and Mixing in the Western Equatorial Pacific Ocean

Helene Theresa Banks

Submitted for the degree of Doctor of Philosophy

Department of Oceanography

December 1996

UNIVERSITY OF SOUTHAMPTON

ABSTRACT

FACULTY OF SCIENCE
OCEANOGRAPHY
Doctor of Philosophy

INTRUSIONS AND MIXING IN THE
WESTERN EQUATORIAL PACIFIC OCEAN
by
Helene Theresa Banks

This thesis presents a study of intrusive features in the Western Equatorial Pacific and the role mixing plays in determining the large-scale structure of the Equatorial Pacific. In the thermocline of the Western Equatorial Pacific, intrusions appear as interleaving layers of warm/salty water and cold/fresh water. Using SeaSoar and CTD data, we describe the characteristics of these features; their vertical, meridional and zonal scales, their slopes across isopycnals and their temperature-salinity ratio. Approximately half of the features are shown to be consistent with a mechanism of double-diffusive interleaving, with the diffusive interface dominating the vertical fluxes.

Assuming the small-scale variance drives the medium scale intrusion motion, we estimate the fluxes of heat and salt due to double-diffusive interleaving. We show that the estimated fluxes produced by interleaving are comparable with fluxes produced by mesoscale eddies as calculated from mooring measurements in the Western Equatorial Pacific. The effective lateral diffusion coefficient due to interleaving is estimated to be 1×10^3 m^2 s^{-1}, a value which is believed to be significant in large-scale models of the Equatorial Ocean. Using the linear stability theory for double-diffusive interleaving on an Equatorial beta plane, we derive the functional form of the vertical and cross- frontal interleaving fluxes. The transfer of tracers produced by interleaving is proportional to the buoyancy frequency and the lateral salinity gradient.

Experiments are performed using a two-dimensional model to assess the impact of mixing parameterizations on the large-scale circulation. We find that both the lateral mixing of momentum and tracers influences the characteristics of the resulting tracer and dynamic fields; the Sea Surface Temperature can be changed by O(1°C) and the speed of the Equatorial Undercurrent by O(50%). The heat-salt flux ratio is not important in the Equatorial region. The parameterization scheme is effective at confining the circulation to the Equator when implemented geodesically, isopycnally and assuming that diffusive fluxes dominate above the salinity maximum and finger fluxes below. Allowing diffusive or finger fluxes to dominate everywhere leads to asymmetry in the Equatorial circulation. Lateral mixing also plays a role in the transients of the system when, for example, the zonal wind field reverses direction, via the interplay with vertical mixing.

To my parents

Acknowledgements

I would like to thank Dr. Kelvin Richards for his inspiration and scientific advice throughout this project. Also Dr. Harry Bryden, who has encouraged me and helped me at various stages. Dr. Mark Inall and Dr. Angus Graham both gave advice on data analysis. The dedication of the crews and scientific staff of Le Noroit and Charles Darwin contributed to the quality of the datasets. The TAO data was provided by Dr. M. J. McPhaden.

This project was supported by the Natural Enviroment Research Council. Woods Hole Oceanographic Institute gave me the opportunity to participate in WOCE cruise P21 and the GEFD Summer School. This project does not include work undertaken during those times, but the experiences helped me develop as an oceanographer.

Many people have encouraged and supported me during this project. I would like to thank Mark, Tom and my officemates, Lisa and Mark, for stimulating scientific discussion. My many other friends in the department (Lauri, Jae, Stuart, Steve, Greg, Mai-Mai etc) provided moral support. Neil Edwards did some thorough proofreading. Amanda Tyler deserves a special mention for her help with my many computer problems.

I would like to especially thank my parents and my sister for their love and support over the last six years of my education. Words cannot express how deeply appreciative I am of all three of them. Finally, my love and thanks to Stuart who shared the highs and lows of the last eighteen months.

Contents

Chapter 1

Introduction

1.1 Motivation

The El-Nino Southern Oscillation (ENSO) phenomenon is known to many scientists as one of the strongest manifestations of the interaction between the atmosphere and the ocean. The devastating effects ENSO events can have on human and economic interests has seen the prediction of these events become a high priority among the scientific community (Philander 1990).

Much work at present is devoted to the prediction of ENSO events using coupled ocean-atmosphere models (McCreary and Anderson 1991), yet these models are not always successful in predicting ENSO events. In an intercomparison of seven models of the Equatorial Pacific Ocean, Stockdale et al. (1993) suggested that the differences between the models could be attributed to the sensitivity of the models to the parameterization schemes, which represent the fluxes of heat, salt and momentum fluxes produced by sub-grid scale processes, and to the variations in the horizontal resolution of the models. These factors all have a significant impact upon the Sea Surface Temperature (SST). However, due to the uncertainties in the appropriate surface heat flux it is difficult to assess the skill of the various models. The feedback of SST on the atmospheric model can quickly lead to large errors in coupled models (Neelin et al. 1992). Since parameterization schemes may have dramatic effects on the dynamics, to enhance our ability to predict ENSO using numerical models, we must parameterize sub-grid scale physics based on the physical processes which are taking place (McPhaden 1985). This thesis will focus on the representation of one physical process which is not explicitly represented in numerical models of the Equatorial ocean. In this chapter we will review features of the large-scale circulation in the Equatorial Pacific and the existing sub-grid scale parameterizations and then outline

the aims of the present work.

1.2 The large-scale circulation in the Equatorial Pacific

In the last fifteen years, due to our interest in El Nino, hydrographic surveys have focussed on the Equatorial Pacific. This began in 1979 with EPOCS (Equatorial Pacific Ocean Climate Study), which was centered in the Eastern Equatorial Pacific, and consisted of hydrographic measurements and current meter moorings. EPOCS was closely followed by the Hawaii-Tahiti shuttle experiment in the Central Equatorial Pacific which consisted of approximately 15 monthly hydrographic surveys during 1979 and 1980.

Since 1984, at least four hydrographic programmes have been undertaken to look at the Western Equatorial Pacific: SURTROPAC (Surveillance Trans-Oceanique du Pacifique, 1984-1991), US/PRC (United States / Peoples Republic of China program for Air-Sea Interaction Studies, 1986-1990), WEPOCS (Western Equatorial Pacific Ocean Circulation Study, 1985-1988) and TOGA (Tropical Ocean Global Atmosphere, 1985-1995). All the programmes consisted of hydrographic surveys and in addition the TOGA programme established a mooring array (Tropical Atmosphere Ocean (TAO) array) across the entire basin in the Equatorial region (5°N - 5°S).

Several authors have presented views of the 'mean' velocity and tracer fields in the upper ocean of the Equatorial Pacific, notably Wyrtki and Kilonsky (1984) for the Central Equatorial Pacific and Gouriou and Toole (1993) for the Western Equatorial Pacific. Figure 1.1 is reproduced from Gouriou and Toole (1993), who computed averaged fields at a longitude of 165°E using data from SURTROPAC and US/PRC between 1984 and 1991. Near the surface in figure 1.1 (A,B) we see the warm pool of the Western Equatorial Pacific associated with sea surface temperatures in excess of 29°C and sea surface salinity below 34.5 psu, due to the high precipitation in this region. Below 100 metres, (A) shows the characteristic spreading of the isotherms associated with the Equatorial Undercurrent (EUC). South of the Equator in (B) we observe a salinity maximum, at a depth of approximately 200 metres. This maximum is the signature of South Tropical Water (Tsuchiya et al. 1989). North of the equator, there is a weaker salinity maximum (North Tropical Water) above the salinity minimum of North Pacific Intermediate Water (Reid 1965). In the mean zonal velocity fields (C,D) we observe the Equatorial Undercurrent flowing eastward at a depth of approximately 200 metres. The maximum speed of the undercurrent is approximately

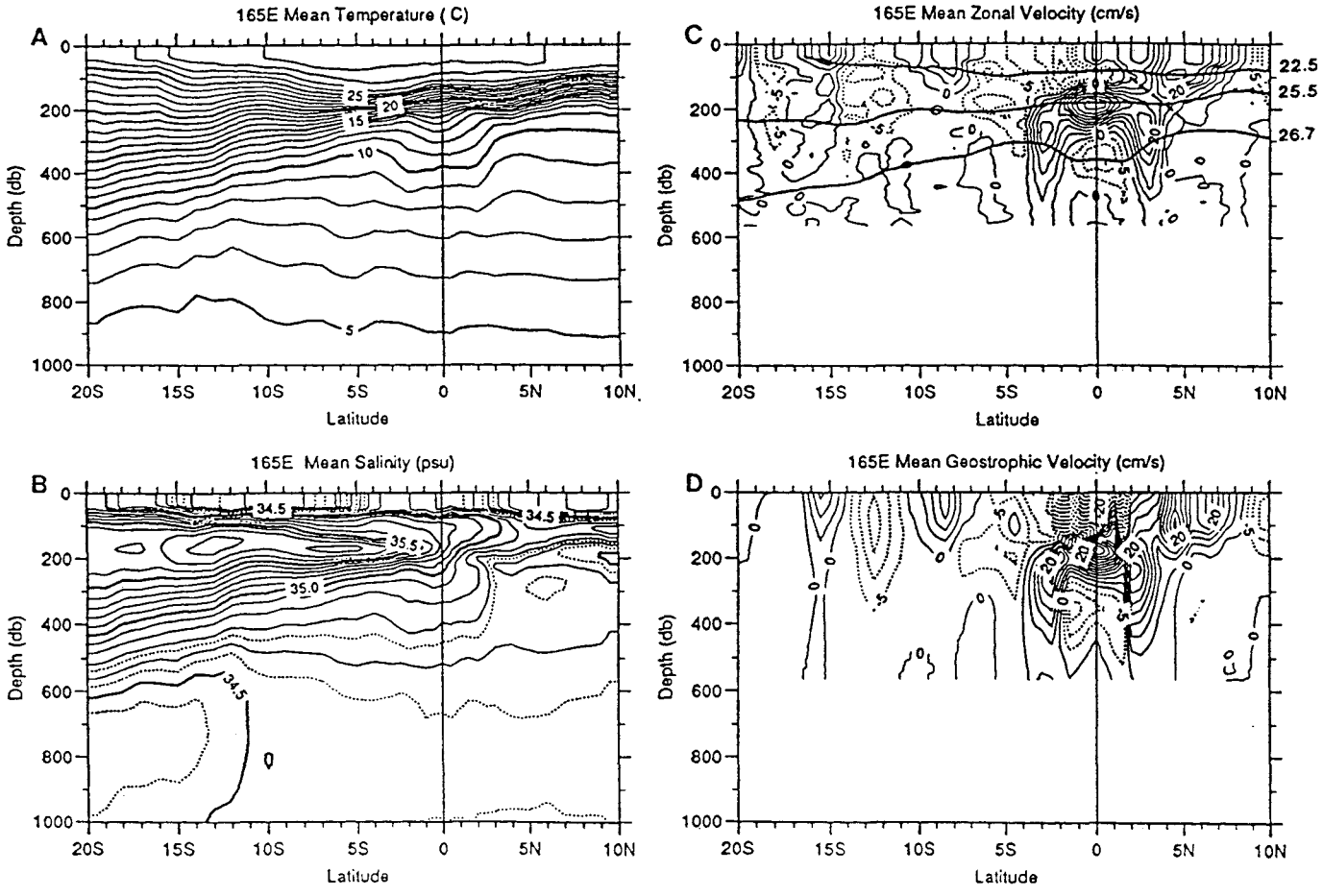

Figure 1.1: Figure 3 from Gouriou and Toole (1993). Mean meridional sections are shown for (A) temperature, (B) salinity, (C) zonal velocity and (D) geostrophic velocity.

45 cm s^{-1}. Above the EUC, the South Equatorial Current (SEC) flows westward and the North Equatorial Countercurrent (NECC) flows eastward. Associated with these currents is a circulation in the meridional-vertical plane; Ekman divergence at the surface, driven by an easterly wind stress, is compensated by convergence at the depth of the EUC. While this simplistic picture is useful in envisaging the flow patterns, in three dimensions the EUC flows eastward and shallows (Bryden and Brady 1985). The thermocline also shallows towards the east which implies that the flow is predominantly along isopycnals. Assuming a hydrostatic balance, this shallowing of the thermocline would suggest that an westward pressure gradient exists in response to the predominantly easterly zonal windstress. The westward pressure gradient drives geostrophic equatorward flow at the depth of the thermocline, which balances the Ekman divergence in the surface layers, and, near the Equator, where geostrophy no longer holds, there is both upwelling (to balance the surface divergence) and eastward flow. This eastward flow was once considered to be due to potential vorticity conservation (Fofonoff and Montgomery 1955) but Killworth (1991) has shown that this is not the case. This argument may hold in the inertial regime of the EUC close to its origins in the Western Pacific (Wacongne 1988), while as the current travels eastward the role of dissipation and mixing may become more important.

The Eastern and Central Equatorial Pacific are forced by near constant easterly winds and the steady state described above prevails. In the Western Equatorial Pacific transient states are equally common. The Western basin is subject to strong changes in the atmospheric forcing — the wind field often reverses (the much discussed Westerly Wind Burst (WWB)) and the freshwater flux is large due to frequent and heavy precipitation. The duration of a typical WWB is between 10 days and 2 months (McPhaden et al. 1990) and is believed to be a precursor to ENSO events (Miller et al. 1988). The ocean response to a WWB is characterised by an eastward surface jet, a westward current below this and a remnant of the EUC at the depth of the thermocline (Hisard and Merle 1970), which reflects the change in the zonal pressure gradient due to forced Equatorial waves (Zhang 1995). It is not clear how important the role of mixing is to the transient response of the ocean.

1.3 Mixing processes

Mixing is commonly referred to as a process which changes the properties of fluid parcels due to molecular diffusion, in contrast to processes which simply rearrange the position of

fluid parcels which are referred to as stirring processes (Eckart 1948). While the distinction between mixing and stirring processes is useful, any process which makes a significant contribution to fluxes of heat, salt and momentum and is not explicitly represented in a numerical model should be parameterized. Features created by stirring processes in the ocean (e.g. eddies) are usually subject to subsequent processes which mix their properties to the finest scale in the ocean. Observations of mixing and stirring processes have been made in the Equatorial Pacific via various datasets and methods, parameterization schemes have been proposed and numerical studies have taken place. In this section we review this work.

1.3.1 Observations

Mesoscale eddy fluxes of heat and momentum

Bryden and Brady (1989) estimated the eddy fluxes of heat and momentum directly from mooring data in the Eastern and Central Equatorial Pacific, while Lukas (1987) estimated the Reynolds stresses from mooring data in the Central Equatorial Pacific. These authors suggested that the source of the observed variability was probably barotropic instability between the EUC and the SEC, leading to tropical instability waves with a timescale of approximately 20 days and similar to features observed in satellite images (Legeckis 1977). Brady (1990) suggested that the waves propagated energy downwards while the momentum fluxes were sufficient to accelerate the EUC above the core and decelerate it below the core. In the mean fields there appears to be no source for barotropic instability in the Western Equatorial Pacific, since the potential vorticity does not change sign (Gouriou and Toole 1993). This may suggest that the contributions of small-scale processes to the large-scale dynamics are different in different regions of the Equatorial Pacific, with momentum fluxes reduced in the Western basin.

Eddy-resolving models (e.g. Cox (1980)) are able to simulate the tropical instability waves with similar characteristics to the observations. A more interesting result for the purposes of this work is the model of Semtner and Holland (1980) which represented small-scale processes via biharmonic friction. Using this representation rather than the more usual Laplacian formulation increases the eddy energy. They found three primary sources for instability in the Equatorial region; a first baroclinic mode planetary wave which appeared to originate in the Eastern Equatorial Pacific, a low-frequency meandering

of the EUC due to the barotropic instability of the EUC in the Eastern Equatorial Pacific and high frequency, high baroclinic mode equatorially trapped waves which were responsible for a large amount of dissipation due to their small length scale.

Turbulence and Microstructure measurements

Microstructure measurements have shown that turbulent dissipation is strongest in the regions with large vertical shear (Crawford 1982). In the surface layer, the measurements show that turbulent dissipation changes over a diurnal cycle (Moum et al. 1989) and it has been possible to derive relationships between the Richardson number and the turbulent mixing (Peters et al. 1988). Below the surface layer, in the EUC core turbulent dissipation is generally small (Moum et al. 1989), while above and below the core dissipation is generally patchy. Moum et al. (1989) suggest that above the EUC core the observed turbulence is produced by breaking internal waves. Below the EUC core, Gregg et al. (1985) suggest that the observed turbulence is associated with thermohaline intrusions and irreversible finestructure, yet the analysis of Peters et al. (1988) found only one example of such a correlation over a $4\frac{1}{2}$ day period.

Finestructure and Intrusive features

The term finestructure is used to describe features in the thermohaline and velocity fields which have a vertical scale less than 100 metres and horizontal scales less than the Rossby radius of deformation (approximately 100 kilometres in the Equatorial waveguide). Three previous authors have examined finestructure in data collected with a Conductivity Temperature Depth (CTD) probe. These data are particularly useful in the study of intrusive features whose water mass signature differs from the surrounding water. Intrusions are examples of irreversible finestructure (McPhaden 1985) and, as pointed out by Stommel and Federov (1967), are probably responsible for significant cross-frontal exchange of heat and salt. The first study, by Toole (1981a), focussed on the Eastern Equatorial Pacific at a longitude of 110°W. Toole's measurements showed coherent temperature and salinity anomalies at a wavelength of 20 metres. He suggested a complex interaction between double-diffusion and internal waves as a mechanism for the observed intrusive features. McPhaden (1985) has analysed data from the Central Equatorial Pacific at a longitude of 150°W. Similar features were observed with a vertical scale O(10 metres). McPhaden's cal-

culations showed that intrusive features accounted for more than fifty percent of the salinity variance in the upper 200 metres. The observations were not sufficient to determine the mechanism for the intrusions, but he suggested that, in addition to the mechanisms suggested by Toole (1981a), baroclinic instability and shear instability might also produce the observed features.

Most recently, Richards and Pollard (1991) were able to collect high resolution measurements using a SeaSoar in the Western Equatorial Pacific at a longitude of 165°E. The picture which emerged from the data was that the features were horizontally coherent over meridional scales O(100 kilometres). No detailed analysis was performed but a further paper by Richards (1991) at least suggested that the characteristic scales of the features appeared to be consistent with a linear stability theory for double-diffusive interleaving. Intrusive features also appear to be present in many of the hydrographic observations collected as part of SURTROPAC (Rual et al. 1995), although the finestructure in these observations has not been analysed. At many of the oceans' frontal regions intrusions are often attributed to double-diffusive interleaving (Schmitt 1994). In the Equatorial Pacific further work is required to establish the characteristics of the intrusions and suggest the dominant process responsible for the features. This would be useful in clarifying the results of Toole, McPhaden and Richards.

1.3.2 Parameterization schemes

Numerical Ocean General Circulation Models (OGCMs) are limited in horizontal and vertical grid resolution by computational resources. It is therefore not always possible to explicitly resolve the momentum and tracer fluxes due to processes which take place at scales less than the grid scale. The fluxes due to such processes must be parameterized. One means of parameterizing fluxes of momentum and tracers due to mixing processes is in terms of a diffusion coefficient on the basis of a downgradient transfer:

$$\overline{u_i'\tau'} = -\kappa \frac{\partial \overline{\tau}}{\partial x_i}$$

where τ is the property being mixed, κ is the diffusion coefficient, u is the velocity field and x_i denotes the direction of interest. Before the 1980s, both the vertical and horizontal diffusion coefficients were taken to be constant. Since then considerable progress has been made in prescribing temporally and spatially varying vertical diffusion coefficients and also in prescribing the transfer in an alternative manner (e.g. Gent and McWilliams (1990)).

Vertical mixing processes

Chen et al. (1994) categorize the three major processes contributing to vertical mixing in the upper ocean as wind stirring, shear instability and convective overturning. One of the first parameterization schemes introduced for vertical mixing was due to Pacanowski and Philander (1981), and was based on an empirical relationship between the vertical diffusion and the Richardson number originally suggested by Munk and Anderson (1948). Various alternatives to the Pacanowski and Philander (1981) scheme have been suggested: mixed layers have been employed (Schopf and Cane 1983) based on the formulation of Kraus and Turner (1967). Peters et al. (1988) based their scheme on observations of the turbulent dissipation rate. Price et al. (1986) suggested a scheme based on dynamic stability. Blanke and Delecluse (1993) suggested a higher order turbulence closure model and Chen et al. (1994) implemented a hybrid vertical mixing scheme, which combined the best aspects of the Kraus-Turner and the dynamical stability model.

Horizontal mixing processes

To date, in all the numerical models of the Equatorial Pacific the horizontal diffusion coefficient has been taken to be constant, but there is an apparent discrepancy over what the appropriate value is. There have been seven estimates deduced from observations of the value of the lateral diffusion coefficient in the Equatorial region (Pacific and Atlantic) which are summarised in table 1.1. The table lists the authors, the region, the type of observation, the proposed mechanism for the fluxes and the suggested values for the coefficients.

With the exception of Toole (1981a), all the estimates suggest a value $O(10^3\ m^2 s^{-1})$. This seems satisfactory, in the sense that the values appear to converge to the same order of magnitude. However, as we will discuss in the next section, the Equatorial dynamics are sensitive enough to the value of the lateral diffusion coefficient that a factor of two or three may be important. Further, each of these estimates are based on different physical processes. Whether a process takes place in a numerical model depends on the resolution of the particular model and it is therefore not an easy task to reconcile the estimates. Even more disconcerting is the fact that the estimates of Lukas (1987) and Bryden and Brady (1989) do not necessarily support the hypothesis of downgradient transfer. Harrison (1978) also showed that in an eddy-resolving model the eddy fluxes and the mean gradient were not always well correlated.

Authors	Region	Type of Observation	$\mid A_H \mid$ x 10^3 m^2 s^{-1}	$\mid K_H \mid$ x 10^3 m^2 s^{-1}	Proposed Mechanism
Katz et al. (1980)	Eq. Atlantic	Mass budget	2	-	?
Toole (1981)	Eastern Eq. Pacific	CTD	600	-	Internal waves
Hansen and Paul (1984)	Eq. Pacific	Drifting buoys	40	-	Barotropic instability
McPhaden (1985)	Central Eq. Pacific	CTD	1	-	?
Fahrbach et al. (1986)	Eq. Atlantic	Drifting buoys	0.65	-	?
Lukas (1987)	Central Eq. Pacific	Mooring/ADCP	-	3-17	Barotropic instability
Bryden and Brady (1989)	Eastern Eq. Pacific	Mooring	0.5-5	0.3-3	21 day oscillation
Richards and Pollard (1991)	Western Eq. Pacific	SeaSoar	3	-	Double-diffusive interleaving

Table 1.1: Summary of previous estimates of the lateral diffusion coefficients for tracers (A_H) and momentum (K_H)

1.3.3 Modelling studies

Given the large number of available parameterization schemes for vertical mixing it is not surprising that many studies have addressed the effects of these schemes on the large-scale circulation. In particular, a study by Schneider and Muller (1994) highlighted the sensitivity of the upper 100 metres to the form of the vertical mixing. When the Price et al. (1986) dynamical adjustment scheme was implemented, downwelling was implied at the Equator in response to Easterly winds which is the exact reverse of the upwelling we expect. The schemes of Blanke and Delecluse (1993) and Chen et al. (1994) appear to be more successful at reproducing shear-induced mixing below the mixed layer than many of the other schemes where this mixing is limited to the mixed layer.

That the lateral mixing might also play an important role in determining the large-scale structure in numerical models of the Equatorial ocean was suggested by Pacanowski and Philander (1981). They note that when they increased the horizontal diffusion coefficient for momentum in their model by a factor of two, the maximum speed of the EUC was reduced by approximately twenty per cent. Yin and Sarachik (1993) also noted a similar result. Maes et al. (1996) have studied the role of the lateral diffusion coefficient in a three-dimensional model taking the diffusion coefficient to be constant. The diffusion coefficients for momentum and tracers were taken to be equivalent, even though there is no strong evidence to suggest that the Prandtl number in the ocean is unity. Figure 1.2 is reproduced from Maes et al. (1996). The figure shows a snapshot of the zonal, meridional and vertical velocity fields when the lateral diffusion coefficient is $O(10^4\ m^2s^{-1})$ (their experiment H), $O(10^3\ m^2s^{-1})$ (their experiment M) and $O(10^2\ m^2s^{-1})$ (their experiment L). The most apparent differences between the three experiments are in the increasing strength of the EUC and the decreasing magnitude of the vertical velocity, following through experiments H to L. They found that there was a non-linear interplay between the horizontal and vertical mixing. They suggest in their conclusions that observations of the mixing processes at the depth of the EUC core would help in determining the appropriate value of the horizontal diffusion coefficient.

1.4 Objectives of this study

A number of important issues relating to mixing in the Equatorial Pacific have been identified in the previous work. These can be summarised as follows:

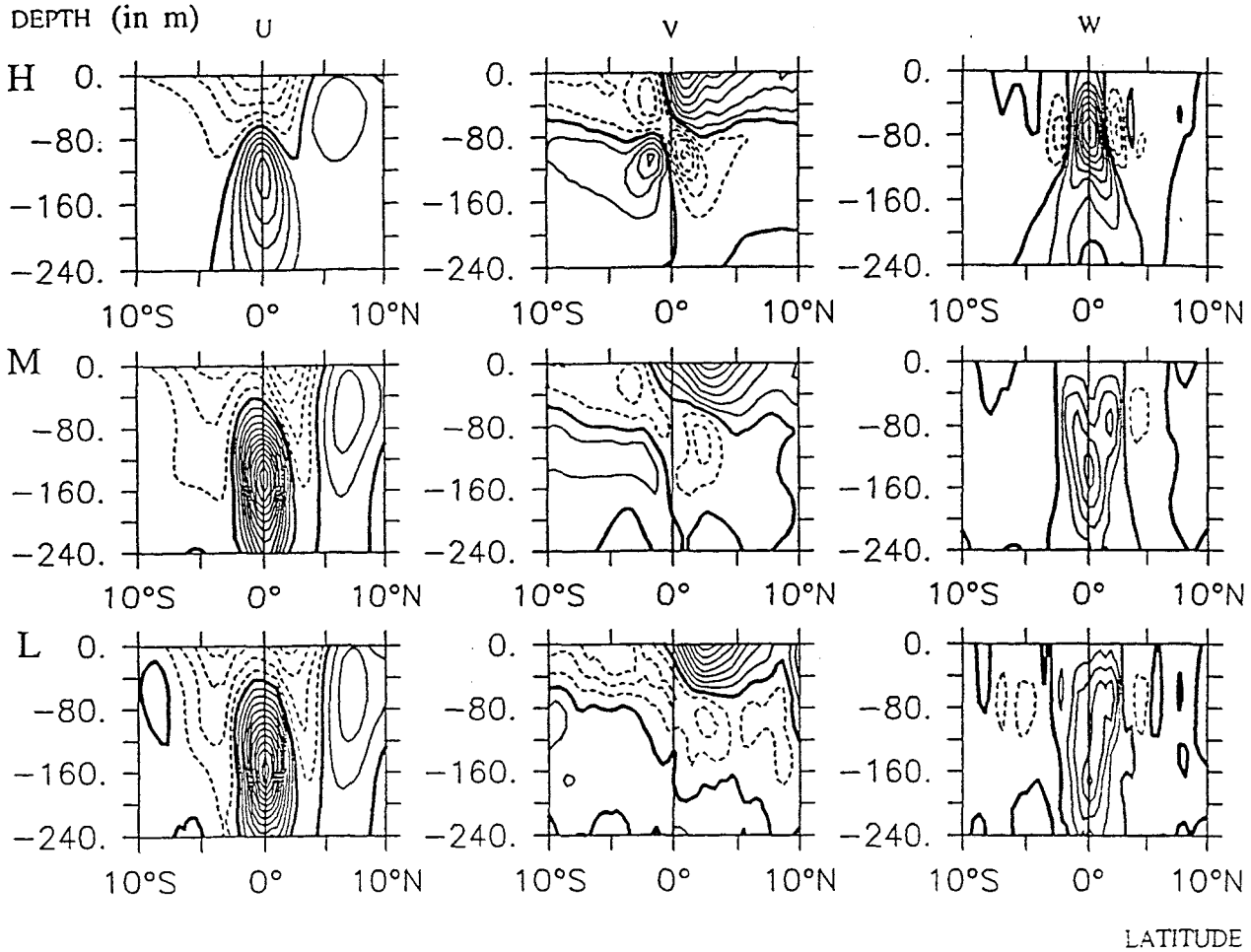

Figure 1.2: Figure 7 from Maes et al. (1996). The upper panels show the velocity fields (left panels are zonal, middle panels are meridional and right panels are vertical velocity) with the lateral diffusion coefficients $O(10^4\ m^2s^{-1})$, the middle panels show the velocity fields with the diffusion coefficients $O(10^3\ m^2s^{-1})$ and the lower panels show the velocity fields with the diffusion coefficients $O(10^2\ m^2s^{-1})$.

- unlike vertical mixing, the mechanisms for lateral mixing in the Equatorial Pacific (particularly in the Western basin) are not well understood.
- intrusions, which are believed to be a signature of lateral mixing, appear to be a common feature of the Equatorial finestructure.
- the characteristics of intrusive features in the Equatorial Pacific have not been well-documented and the mechanisms producing the features have not been determined.
- the sensitivity of models to the value of the lateral diffusion coefficient highlights the lateral mixing as requiring further study.
- one way to proceed in improving ENSO predictions may be to improve the representation of the sub-grid scale physics.

Broadly these issues fall into two categories: the mechanisms mixing heat, salt and momentum and the impact of mixing on the large-scale circulation. Mixing is usually thought of as being produced by turbulence and mesoscale eddies. This thesis will focus on intrusive features and the role they play in producing mixing in the Equatorial Pacific. We will study the features in detail and examine the mechanisms for their production. We will then consider the role of mixing on the large-scale structure of the Equatorial ocean. The objectives of the work presented here are:

1. To determine the characteristics of the intrusive features in the Equatorial Pacific.
2. To deduce the mechanism(s) responsible for intrusive features.
3. To develop a parameterization scheme for the lateral (and vertical) mixing due to the intrusive features.
4. To study the effects of lateral mixing and the parameterization scheme on the largescale dynamics.

This thesis will focus on observations from the Western Equatorial Pacific. The applicability of the results to other regions of the Equatorial Pacific will be discussed later. The remainder of this thesis is outlined as follows; in chapter II, intrusive characteristics from two experiments will be presented and the mechanisms responsible for these features will be deduced; in chapter III we estimate the appropriate value of the lateral diffusion coefficient due to different processes and develop a parameterization scheme for the representation of intrusive mixing in numerical models; in chapter IV we study the sensitivity

of model dynamics to the parameterization schemes and finally in chapter V we present our conclusions, put the work into perspective and suggest future work.

Chapter 2

Intrusive features in the Western Equatorial Pacific

2.1 Introduction

Vertical profiles of temperature and salinity often show features which have a different water-mass signature to the surrounding water. For example, figure 2.1 shows the temperature and salinity measured by a CTD in the thermocline of the Equatorial Pacific; the high salinity water from the South Pacific converges with the fresher water from the North Pacific.

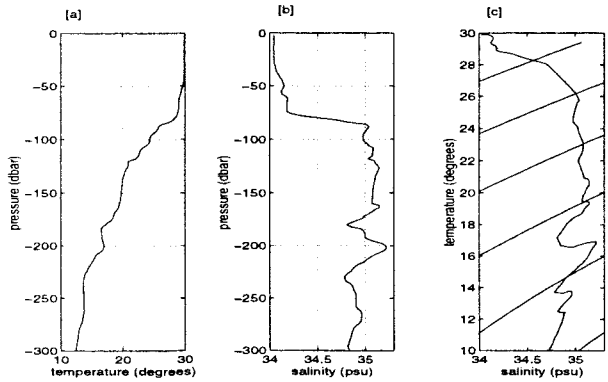

Figure 2.1: Temperature-salinity profiles from a CTD cast on the Equator in the Western Equatorial Pacific. [a] shows the temperature profile against depth, [b] shows the salinity profile against depth and [c] shows the temperature-salinity profile with surfaces of constant potential density contoured.

Features with a vertical scale O(20m) are apparent in both the temperature and the salinity profiles. The temperature-salinity profile shows that these features are aligned almost parallel to isopycnals. Such features are referred to as intrusions. Intrusive features are now considered to be common characteristics in frontal regions (Schmitt 1994). However,

the process by which intrusive features are produced is still a matter of some debate and may depend to a certain extent on the local dynamics.

Stommel and Federov (1967) were the first investigators to observe intrusive layers at an oceanic front; they noticed density-compensated temperature inversions in CTD casts. Since that time many observations have followed. Among others, Joyce et al. (1978) and Toole (1981b) have observed intrusions and lenses in the Antarctic polar front, Barton and Hughes (1982) have observed interleaving off Northwest Africa and recently Armi et al. (1989) observed intrusive features leading to the destruction of a Mediterranean salt lens (Meddy Sharon) over a two year period. The vertical scale of the features is usually between 10 and 50 metres. Gregg (1980) was able to map an intrusion in three dimensions by towing a SeaSoar on an appropriate gridded area. The intrusion mapped by Gregg was 7 km long in the cross-front direction and only 2 km wide in the along-front direction.

All the observations described have been made at water mass boundaries (fronts), which have several common properties:

A. cross-frontal thermohaline gradients exist.

B. (possibly weak) cross-frontal density gradients exist, which drive a geostrophic current with vertical and possibly cross-frontal shear.

Laboratory experiments which attempt to model frontal intrusions usually approximate fronts by assuming only property A. An analogy is made between the heat/salt system and the salt/sugar system; the ratio of molecular diffusivities of the two components in each case is different (2 for heat/salt and 1.2 for salt/sugar). The experiment usually involves separating a tank into two regions with a dam in place and filling each side of the tank with a stably stratified solution of one component; the density difference between the two is minimised. The difference in molecular diffusivities between the two components allows double-diffusive interfaces to form and quasi-horizontal intrusions are produced. In the experiments of Ruddick and Turner (1979), intrusions can be observed to slope across isopycnals (which are initially horizontal). Experiments such as these give insight into the formation of interleaving layers by double-diffusion - salt fingers form at one interface, diffusive convection takes place at the opposite interface and the resulting vertical buoyancy flux (produced by the difference in vertical transfer of heat and salt) drives a lateral motion which slopes across isopycnals, depending on which interface dominates, as illustrated in figure 2.2. The experiments by Ruddick and Turner (1979) are examples of finger driven layers while those of Thorpe et al. (1969) are examples of

diffusive driven layers. Evidence for double-diffusive interfaces between intrusions in the ocean was provided by Williams (1981) who was able to photograph finger and diffusive interfaces on Gulf Stream intrusions.

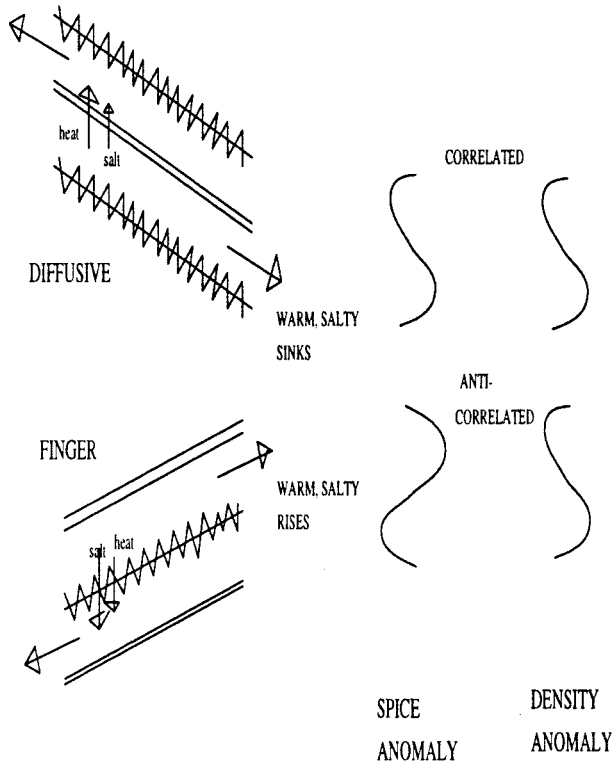

Figure 2.2: Schematic of double-diffusive interleaving; the jagged lines represent finger interfaces, the double lines represent diffusive interfaces. In the top panel fluxes due to the diffusive interface dominate and warm, salty layers sink. The feature will be characterised by a positive spice anomaly and, because it is 'heavy' (due to the vertical fluxes), a positive density anomaly. In the lower panel fluxes due to the finger interface dominate and warm, salty layers rise. A positive spice anomaly will be correlated with a negative density anomaly.

The criticism of models such as the above for oceanic fronts is that they ignore property B. To the author's knowledge, all laboratory experiments which model property B ignore property A and are therefore not subject to double-diffusion. While many experiments model the classical baroclinic instability, experiments by Calman (1977) have shown that double-diffusion is not always a prerequisite for layering to form. McIntyre (1970) has shown that a baroclinic vortex is unstable to unequal diffusivities of mass and momentum, which may produce axisymmetric layers. Although we will discuss baroclinic instability, we will not discuss McIntyre's instability, since Hebert (1988) and Ruddick (1992) have argued that the scales of McIntyre's instability are too small to relate to oceanic intrusions.

In the Western Equatorial Pacific, Richards (1991) has suggested that the scales predicted by the linear stability analysis for double-diffusive interleaving on an Equatorial beta plane were consistent with the scales of the features which were briefly described in Richards and Pollard (1991). Although no detailed analysis was performed, the observations were found to be consistent with this hypothesis. Toole (1981a), in an analysis of finestructure in the Eastern Equatorial Pacific, suggested that not all of the observed features were consistent with such a hypothesis and suggested low frequency internal waves may have produced the observed finestructure. McPhaden (1985) analysed data from the Central Equatorial Pacific and suggested that the origins of the features may be from multiple mechanisms (baroclinic instability, double-diffusion, shear instability, etc). We will focus on the characteristics and origins of features in the thermocline of the Western Equatorial Pacific.

In section 2.2 we will give brief details of two cruises, which took place in the Western Equatorial Pacific. In section 2.3 the large-scale fields will be presented for comparison between the different climatic states the ocean was experiencing. In section 2.4 the finestructure fields will be presented and in section 2.5 we will describe the characteristics of the intrusions; their vertical, meridional and zonal scales, their slopes across isopycnals and their temperature-salinity ratio. In section 2.6 we compare the results with the double-diffusive interleaving model and in section 2.7 we discuss the results.

2.2 The data

The observations derive from two hydrographic datasets in the Western Equatorial Pacific, which will for future reference be known as POI and CD32. The locations of the two cruises are shown on figure 2.3 and the spatial and temporal details of the cruises are summarised in table 2.1.

The POI measurements will be analysed extensively in this chapter. They were collected as part of the TOGA Coupled Ocean Atmosphere Response Experiment (TOGA-COARE) during the Intensive Observation Period. Data was collected aboard R/V Le Noroit, a French ship based at the ORSTOM research centre in Noumea, New Caledonia, from December 7th 1992 to February 24th 1993. The cruise consisted of eighteen meridional sections, along 156°E, from 5°S to 5°N. Hydrographic observations were taken by CTD for six sections and SeaSoar for the remaining twelve. An ADCP (Acoustic Doppler

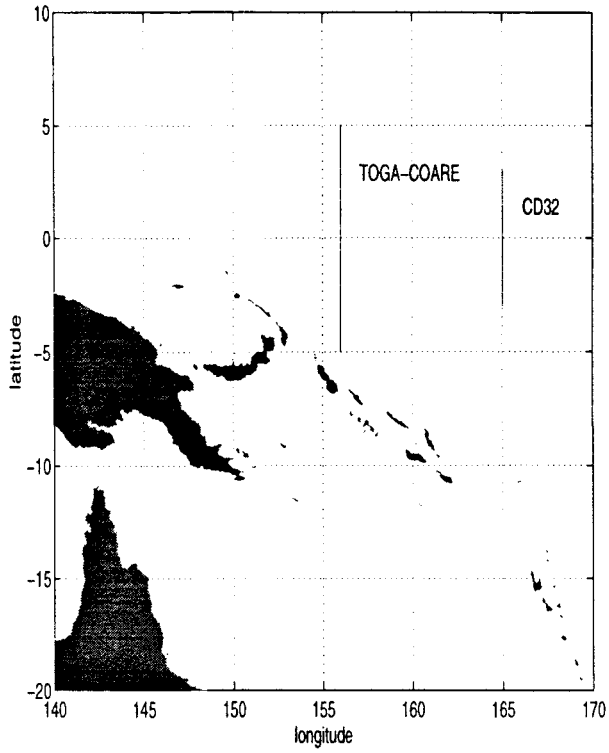

Figure 2.3: Map to show the latitudes and longitudes of data collection during CD32 and POI (TOGA).

Current Profiler) provided continuous current measurements. Details on data collection and processing are given in the cruise report (Richards et al. 1993). During the first seven SeaSoar sections measurements were taken to a depth of 250 metres, while an instrumentation problem during the next five sections meant that measurements were sparse during the eighth and ninth section and limited to a depth of 200 metres during the final three sections.

The CD32 measurements, which will be used to a lesser extent, were collected on board RRS Charles Darwin between 3rd April and 2nd May 1988. The observations which will be used are SeaSoar measurements which were taken between 3°S and 3°N along 165°E and the survey which was taken centred on the Equator at 165°E. Further details of the data collection are given in the cruise report (Richards et al. 1988).

2.3 Large-scale fields

In this section we will look at the large-scale temperature, salinity and velocity fields observed during TOGA-COARE and CD32. It will be important later to our discussion of

Reference Name	Instrument Type	Longitude °E	Latitude °N	Start time year/jday	End time year/jday
CT321	SeaSoar	165	-3-3	1988/102	1988/104
CT32B	SeaSoar	164.3-165	-0.5-0.5	1988/106	1988/114
CT322	SeaSoar	165	-3-3	1988/115	1988/118
POICTD	CTD	156	-5-5	1992/337	1993/60
POI1	SeaSoar	156	-5-5	1992/365	1993/3
POI2	SeaSoar	156	-5-5	1992/3	1993/7
POI3	SeaSoar	156	-5-5	1993/7	1993/10
POI4	SeaSoar	156	-5-5	1993/14	1993/17
POI5	SeaSoar	156	-5-5	1993/17	1993/20
POI6	SeaSoar	156	-5-5	1993/20	1993/23
POI7	SeaSoar	156	-5-5	1993/23	1993/27
POI8	SeaSoar	156	-5-5	1993/27	1993/29
POI9	SeaSoar	156	-5-5	1993/34	1993/37
POI10	SeaSoar	156	-5-5	1993/37	1993/41
POI11	SeaSoar	156	-5-5	1993/41	1993/44
POI12	SeaSoar	156	-5-5	1993/44	1993/47

Table 2.1: Summary of spatial and temporal details of observations in the Western Equatorial Pacific during experiments POI and CD32.

the time-history of the finestructure and will allow us to put into context the limits to our knowledge of the intrusive features in a complex and time-dependent background state.

2.3.1 TOGA-COARE

Temperature,salinity and density fields

Figure 2.4 shows the mean temperature, salinity and density fields which were calculated by averaging all CTD and SeaSoar sections from the COARE period onto a 4 m (in the vertical) by 50 km (in the horizontal) grid. The surface layer is characterised by the warm pool (with temperatures in excess of 28 °C and salinities less than 34.5 psu). The mixed layer depth is approximately 60 m. In the thermocline, there is a bowing of the isotherms and isopycnals associated with the Equatorial Undercurrent (EUC). The salinity field gives us a better indication of the water masses in the region. Centred at 150 m south of the Equator we observe the salinity maximum associated with the Subtropical Thermocline Waters (STW). During the cruise period, the maximum salinity of the STW was 35.4 psu. There appears to be a northward extension to this water mass, centred at 100m, which reaches a maximum of 35.0 psu north of the equator. There is some debate as to the origin

of this northward extension but it is believed to be associated with the El Niño which was taking place during TOGA-COARE. The position of the salinity maximum and the strength of the front, defined as the meridional salinity gradient, is also seen to shift during the period of the observations. We will refer to this in detail in section 2.5.1.

Velocity fields

Figure 2.5 shows the corresponding mean zonal and meridional velocity sections. We see the zonal velocity field during the COARE period is different to the long term mean suggested by Gouriou and Toole (1993). The near surface currents are generally westward, except for a strong countercurrent at 4°S. The westward flow reaches a subsurface maxima of 30 cm s^{-1} at a depth of 100 metres. Below this, the EUC is centred at 200 metres, with a maximum velocity of 30 cm s^{-1}, and there is some evidence for a westward Equatorial Intermediate current below. North and South of the EUC, there are maxima in the eastward velocity. These currents have been identified by Eldin et al. (1994) as the North and South Subsurface Countercurrents. In the meridional velocity field, the surface Ekman divergence, associated with upwelling, appears to be centred at 3°S and mid-depth convergence appears to be at a depth of 150 metres on the Equator.

There are obvious difficulties in interpreting a 'mean' field during a period when the zonal wind field was highly variable, leading to reversals in the surface velocity fields and transmitted to depth by the reversal of the zonal pressure gradient. Figure 2.6 taken from Eldin et al. (1994) shows the wind stress and current velocity vectors for the surface layer (0-60 m), the upper thermocline (60-150m) and below the thermocline (150-280 m).

The wind stress shows that during December, strong westerlies prevailed, by mid-January the trade winds (easterlies) returned and a second westerly wind burst took place north of the Equator in February. The surface layer appears to respond rapidly to the local wind stress (on a timescale of a few days), with eastward and westward Yoshida jets centred on the Equator and an indication of Ekman dynamics off the Equator corresponding to surface divergence/convergence. In the upper thermocline the currents appear to be more stable and only partially affected by the surface wind stress; the flow is generally westward on the Equator, reversing only in early February. The flow below the thermocline is dominated by eastward flow associated with the EUC and shows little indication of being affected by local surface forcing. In chapter 4 we will examine the response of the ocean to

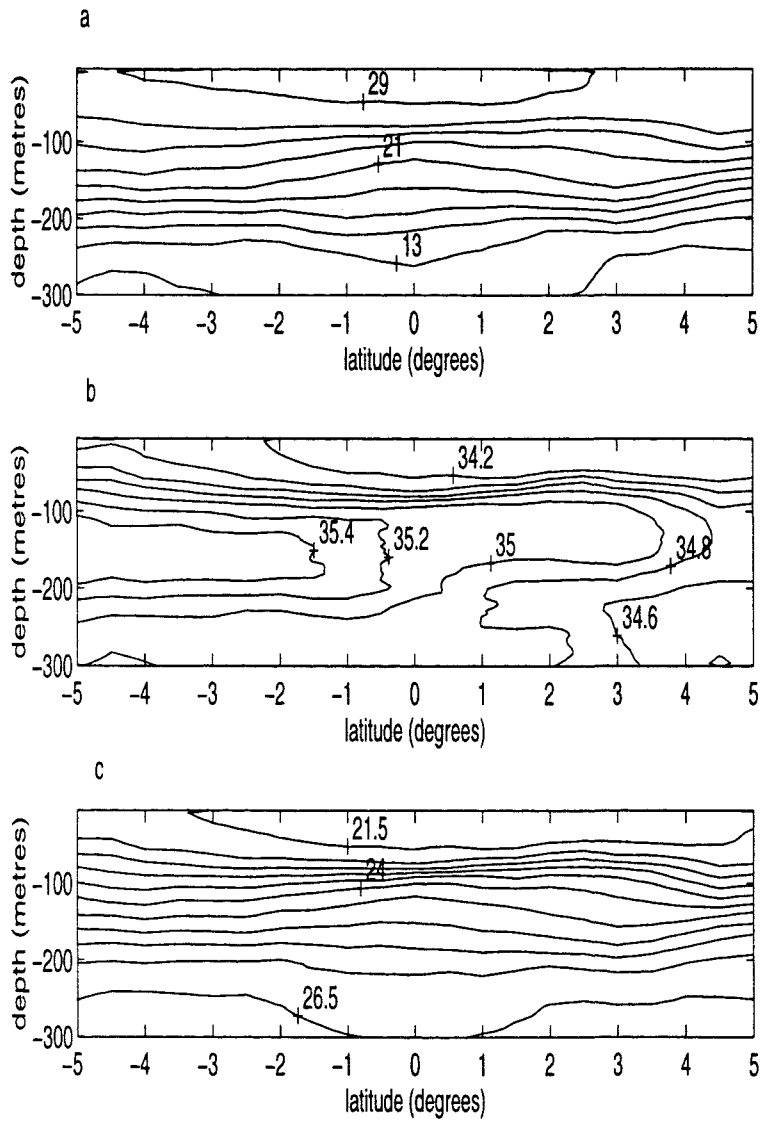

Figure 2.4: [a]Mean temperature section (° C) (upper panel),[b]Mean salinity section (psu) (middle panel), [c]Mean potential density section (kg m^{-3}) (lower panel) for POI. Means are calculated using 12 SeaSoar sections and six CTD sections.

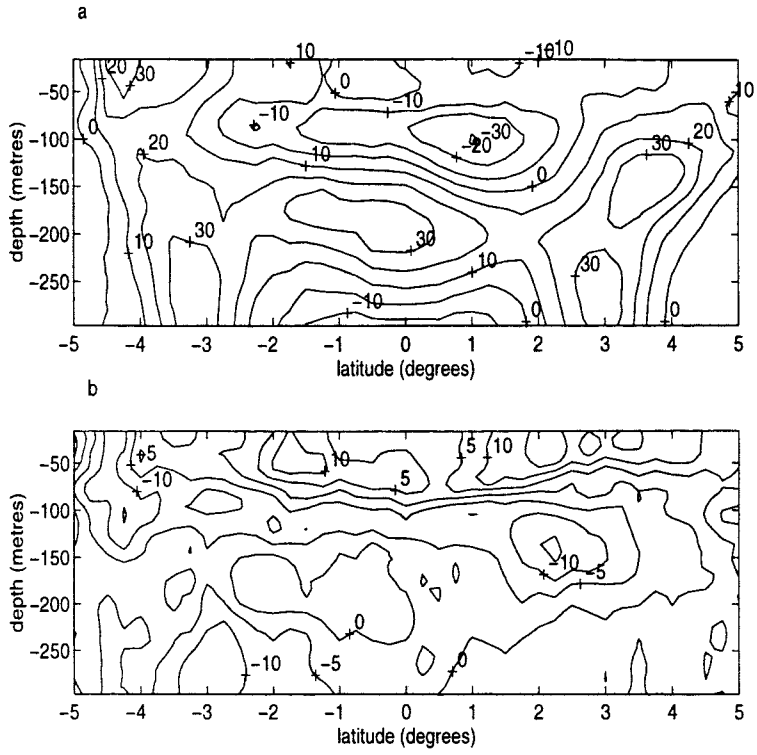

Figure 2.5: [a]Mean zonal velocity (cm s^{-1}) (upper panel), [b]Mean meridional velocity section (cm s^{-1}) (lower panel) for POI calculated from ADCP data.

a WWB in more detail.

2.3.2 CD32

Temperature,salinity and density fields

Figure 2.7 shows the temperature, salinity and density fields observed during one north-south section of this cruise. Once again we observe bowing of the isotherms/isopycnals associated with the EUC. Compared with the mean sections from TOGA-COARE, the potential density fields suggest that upwelling, associated with easterly winds, was predominant in the upper ocean during this period, which is indicative that the ocean was experiencing La Niña during this period. This should be compared with the COARE period which was subject to strong changes in the zonal wind field (Eldin et al. 1994) associated with El Niño . The salinity maximum, associated with STW is centred at 170 m and attains a maximum salinity of 35.8 psu, 0.4 psu higher than that observed 44 months later during TOGA-COARE. The northward extension to this maximum was not present and this is consistent with the idea that this is related to El Niño .

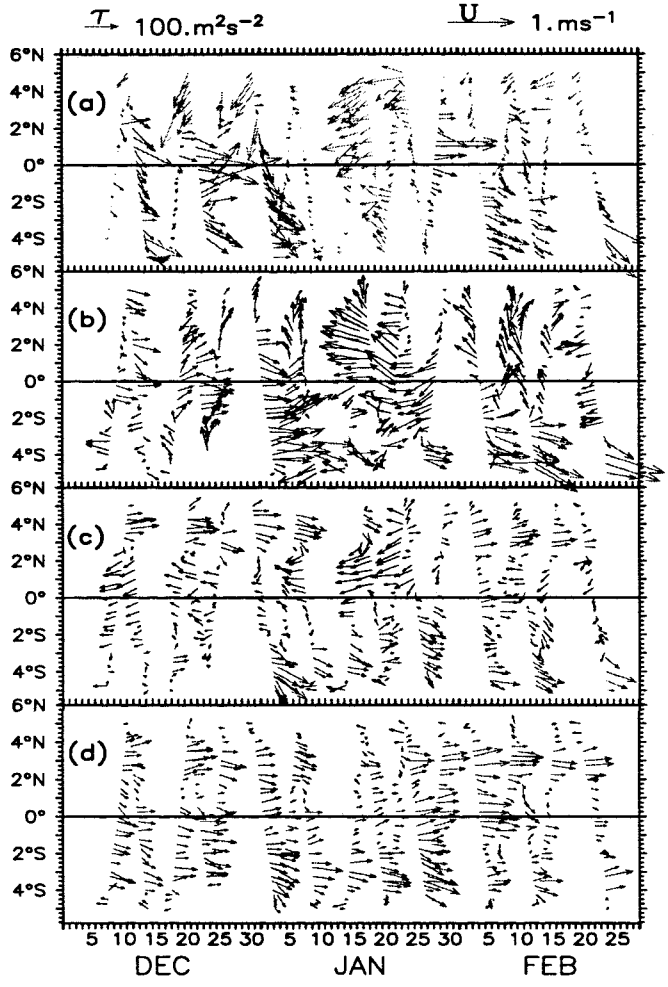

Figure 2.6: Figure 4 from Eldin et al. (1995). The upper panel shows the wind stress vectors, the second panel shows the current vectors for the 16-60 m layer, the third panel shows the current vectors for the 60-150 m layer and the bottom panel shows the current vectors for the 150-280 m layer.

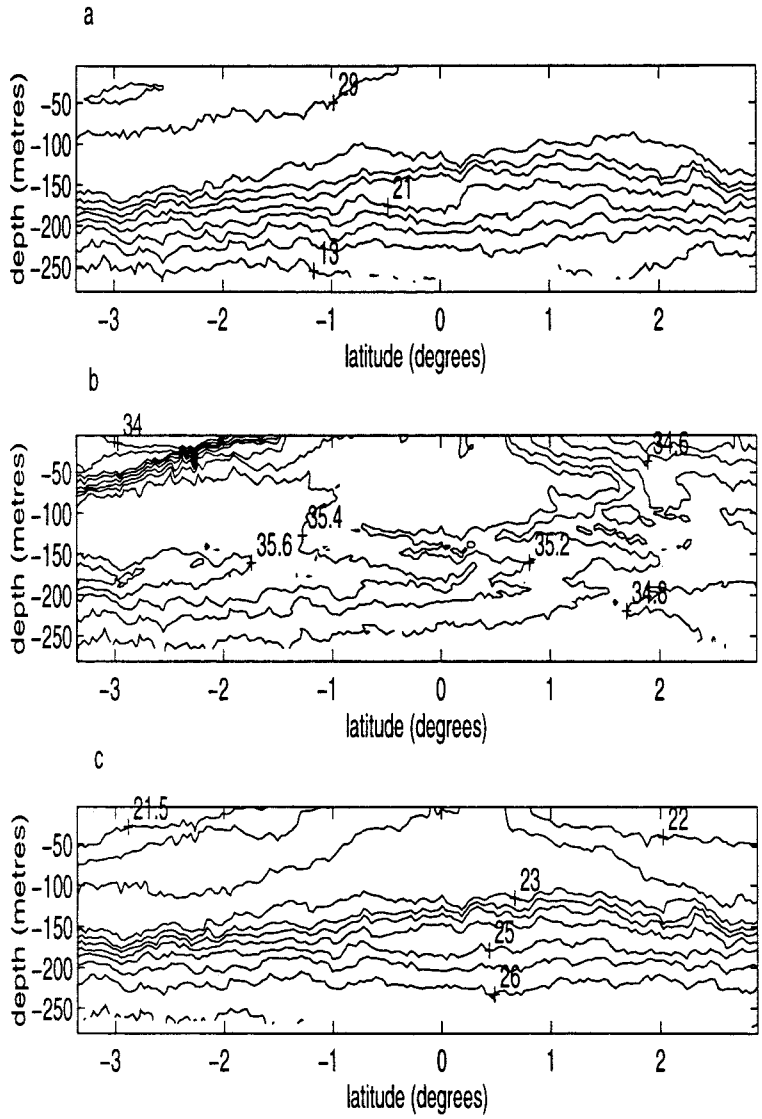

Figure 2.7: [a]Temperature section (°C) (upper panel), [b] Salinity section (psu) (middle panel), [c]Potential density section (kg m^{-3}) (lower panel) for CD32 section 1.

2.4 Finestructure fields

The SeaSoar data was gridded onto a 2 m (in the vertical) by 4 km (in the horizontal) grid. The SeaSoar descends to a depth of approximately 250 m and returns to the surface every 2-3 kilometres, which implies that any coherence observed will not be due to aliasing of measurements. Figure 2.8 shows a waterfall plot of salinity and potential temperature profiles for a 40 km section taken during CD32; the local maxima and minima in the salinity field are very pronounced (O(0.2 psu)), while the temperature profiles have a more steplike structure, except for the strongest features which show some evidence for a temperature inversion. To examine the finestructure further we need to calculate variables which will give us insight into the mechanism.

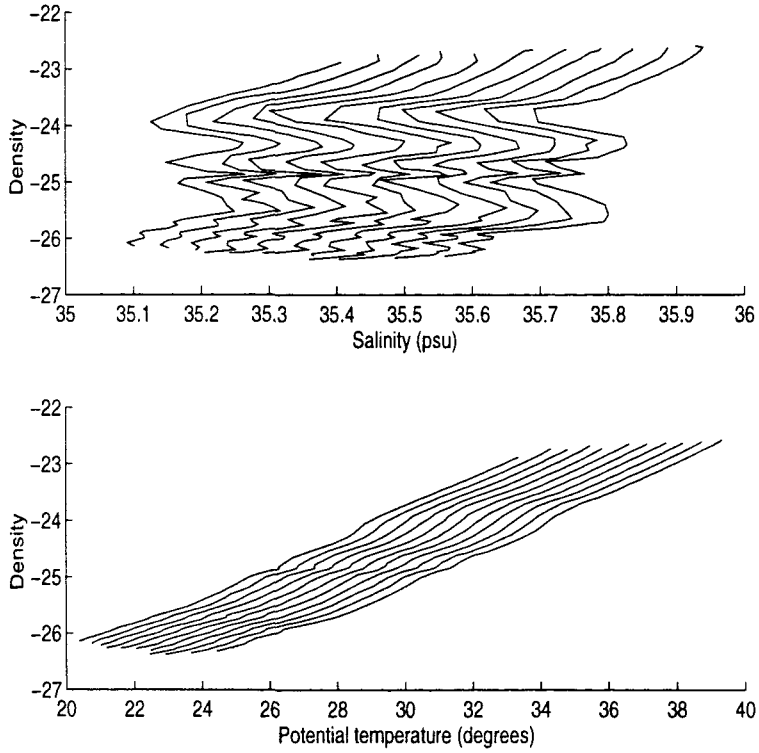

Figure 2.8: [a]Salinity profiles offset by 0.05 psu (upper panel), [b]Potential temperature profiles offset by 0.1 °C (lower panel) taken from SeaSoar profiles between 0.1°S and 0.5°S of CD32 section 1.

2.4.1 Finestructure variables

Spice anomaly

The gridded Seasoar and CTD data was processed as a sequence of vertical profiles. The potential density and salinity ($S(\sigma)$) profiles were low-pass filtered using a fourth order Butterworth filter with an 80m cutoff, in a similar manner to that described by Ruddick and Walsh (1994) to give $\overline{S}(\overline{\sigma})$. The spice anomaly (Jackett and McDougall 1985) is then calculated:

$$Sp = S(\sigma) - \overline{S}(\overline{\sigma}). \tag{2.1}$$

This differs from the definition of Jackett and McDougall (1985) by a factor of 2β.

The spice anomaly is related to the salinity anomaly, but the difference is taken at constant potential density rather than constant depth (or pressure). As noted by Ruddick and Walsh (1994), internal wave noise will not affect the calculation of the spice anomaly, since internal waves will alter the isopycnal depth but not the $S - \sigma$ relation.

Associated with the spice anomaly, we can define a density anomaly, given by:

$$\sigma' = \sigma - \overline{\sigma} \tag{2.2}$$

and we would expect this variable to contain some signature of internal waves.

A positive spice anomaly indicates a warm, salty anomaly and a negative spice anomaly indicates a cool, fresh anomaly, while positive density anomaly indicates relatively heavy water and a negative density anomaly indicates relatively light water. Figure 2.2 shows the relationship between spice anomaly and density anomaly we expect to observe if double-diffusive interleaving is responsible for the observed features. If the temperature and salt fluxes are dominated by the diffusive interface then warm, salty anomalies (a positive spice anomaly) will sink (i.e., relatively heavy and associated with a positive density anomaly) and the spice anomaly and density anomaly will be correlated. Conversely if the finger interface dominates then warm, salty anomalies will rise (i.e., relatively light and associated with a negative density anomaly) and the spice anomaly and the density anomaly will be anti-correlated.

Turner angle

The Turner angle is defined:

$$Tu = \arctan(\alpha\frac{\partial\theta}{\partial z} - \beta\frac{\partial S}{\partial z}, \alpha\frac{\partial\theta}{\partial z} + \beta\frac{\partial S}{\partial z}). \tag{2.3}$$

The Turner angle is an extension of the definition of the stability ratio, R_ρ ($=\alpha\theta_z/\beta S_z$, where α is the thermal expansion coefficient and β is the saline contraction coefficient). It is particularly useful in defining regimes of double-diffusive convection. Figure 2.9 illustrates how the Turner angle is interpreted; between -45 and 45 degrees the stratification is stable, between 45 and 90 degrees the stratification is in the salt finger regime, between -90 and -45 degrees the stratification is in the diffusive regime and beyond $\pm$ 90 degrees the stratification is statically unstable.

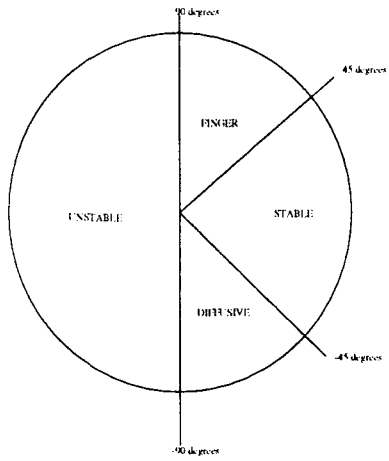

Figure 2.9: Diagram to illustrate interpretation of Turner angle.

2.4.2 CTD profiles

The finestructure variables have been calculated for 136 CTD profiles taken during POI between 5°S and 5°N. The profiles are then placed into five categories according to the correlation (by eye) between the spice anomaly and the density anomaly:

- no apparent correlation (U)
- positive correlation (P)
- negative correlation (N)
- positive correlation in upper part, negative correlation in lower part (PN)
- negative correlation in upper part, positive correlation in lower part (NP).

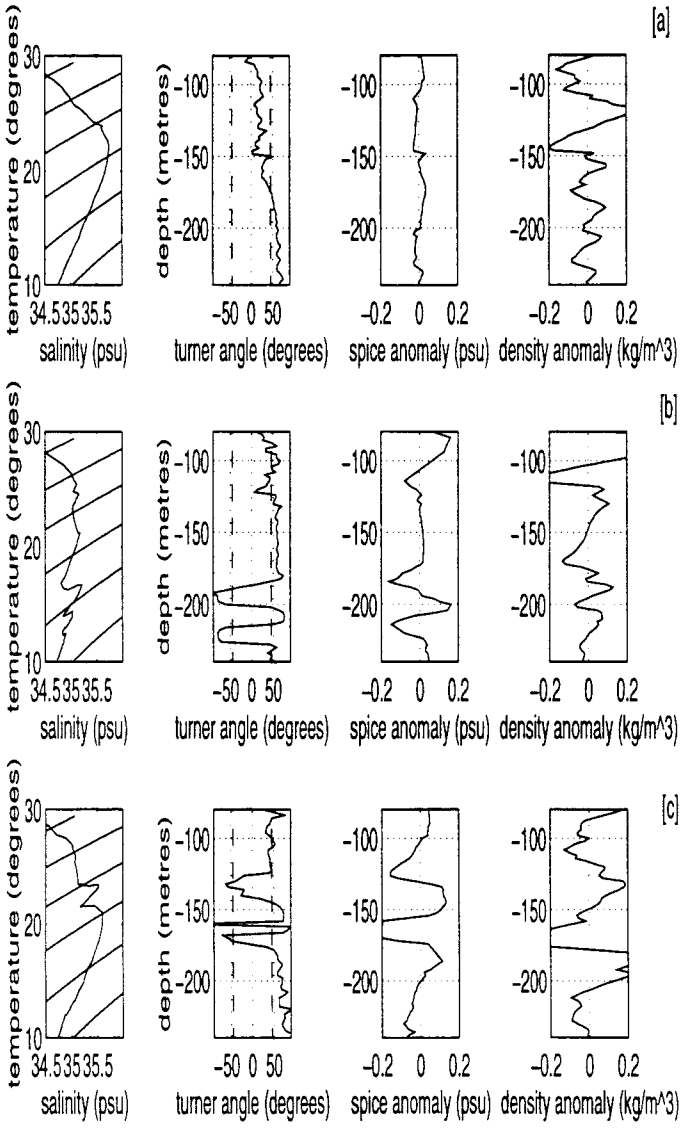

Figure 2.10: [a]T-S relation, turner angle, spice and density anomaly for CTD profile 1 (category U) (upper panels), [b]for CTD profile 2 (category PN) (middle panels), [c]for CTD profile 3 (category P) (lower panels) from POI.

To illustrate this we show three CTD profiles in figure 2.10; the first (CTD1) was taken at 5°S, 156°E on 7th December 1992, the second (CTD2) was taken on the Equator at 156°E on 9th December 1992 and the third (CTD3) was taken at 2.5°S , 156°E on 13th December 1992. For each profile the left-hand panel shows the $\theta - S$ profile with isopycnals marked, the second panel shows the Turner angle with the vertical lines indicating the boundaries between the diffusive, stable and finger regimes and the final two panels show the spice anomaly and density anomaly respectively. CTD1 is an example from category U; the spice anomaly is very small, suggesting that there is little intrusive activity at this latitude, while the density anomaly contains some variability which is presumably due to internal wave strain. The Turner angle is in the stable regime above 150 m and in the finger regime below 200m which is as we expect for the background stratification. CTD2 is an example from category PN; above 180 m the spice anomaly and density anomaly appear to be correlated, while below 180 m the spice anomaly and the density anomaly appear to be anti-correlated suggesting that intrusions may be driven by vertical double-diffusive fluxes with diffusive fluxes dominating in the upper part of the profile and finger fluxes dominating in the lower part of the profile (comparable to the situation Ruddick (1992) identified in Meddy Sharon). The Turner angle is much more variable in this profile; it appears to be generally in the finger regime with regions when it moves into the stable and diffusive regime. Below 150 m the diffusive layers appear to be O(10 m) thick, while above 150 m the Turner angle is never in the diffusive regime which may be due to the fact that diffusive layers may be very thin. CTD3 is an example from category P; the profiles appear to be reasonably well correlated at all depths, except for a small phase shift above 150m, suggestive of diffusive fluxes dominating. This is consistent with the Turner angle which oscillates between the finger and diffusive regime between 100 and 200m.

In table 2.2 we summarise the number of profiles in each of the categories in latitude bands. The results suggest that poleward of 3° of latitude, the density anomaly and spice anomaly are uncorrelated (c.f. CTD1). The observed signal in the density anomaly may be produced by internal waves. Equatorward of 1° of latitude there is indication of positive/negative correlation (c.f. CTD2) consistent with diffusive/finger fluxes dominating depending on the background stratification (the salinity gradient changes sign at approximately 170 m) and also some negative correlation which may be associated with finger fluxes dominating. In the region between 3° S and 1° S the profiles appear to show both positive correlation and negative/positive correlation. The positive correlation may be as-

Start latitude	End latitude	Number of CTDs in category				
		U	N	P	NP	PN
5°S	3.5°S	15	0	1	0	0
3°S	1°S	17	5	10	11	1
0.5°S	0.5°N	6	7	2	0	5
1°N	3°N	10	12	3	2	2
3.5°N	5°N	21	5	0	1	0

Table 2.2: Summary of the number of CTD profiles in each correlation class (U, N, P, NP, PN) in five latitude bands.

sociated with diffusive fluxes dominating, while the negative/positive correlation would suggest that if the intrusions are produced by double-diffusion, finger fluxes would dominate where the stratification is stable with respect to salinity (above the salinity maximum) and diffusive fluxes would dominate where the stratification is unstable with respect to salinity (below the salinity maximum). This is in contrast to the situation in Meddy Sharon (Ruddick 1992). In the region between 1° N and 3° N the profiles show negative correlations suggesting that finger fluxes would dominate.

We have also calculated correlation coefficients between the density anomaly and the spice anomaly. Approximately 50% of the profiles indicate a positive correlation between the density and the spice anomaly at the 95% significance level. Although caution should be applied when interpreting this result, it is highly suggestive of diffusive fluxes driving the intrusions during this period within a few degrees of the Equator.

2.4.3 SeaSoar sections

Figure 2.11 shows the salinity as measured by the SeaSoar, the mean salinity (low-pass filtered) and the spice anomaly for the thermocline region of the first POI SeaSoar section (we show the depth range 80-240 m).

In the initial salinity field some evidence for intrusions is present, particularly in the vicinity of the Subtropical Thermocline Water (STW). When this field is low-pass filtered we can easily identify the large-scale field, with some evidence of internal wave noise. The spice anomaly, when compared with the initial salinity field, can now be seen to be a good indicator of the presence of warm/salty and cool/fresh anomalies. This figure gives a striking picture of the meridional coherence, vertical scales and general abundance of intrusive features.

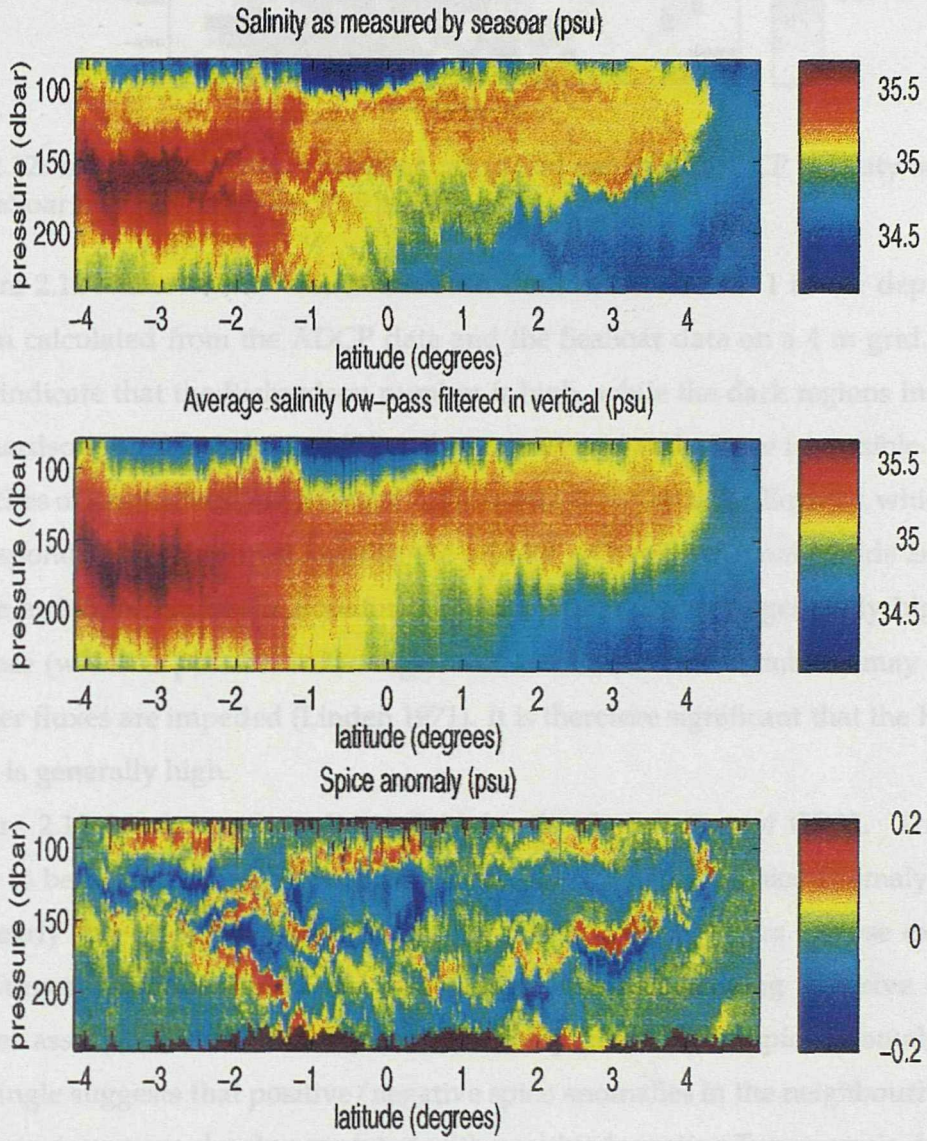

Figure 2.11: [a]Salinity as measured by SeaSoar (upper panel),[b] Mean salinity applying Butterworth filter (middle panel),[c]Spice anomaly (lower panel) for the first POI SeaSoar section.

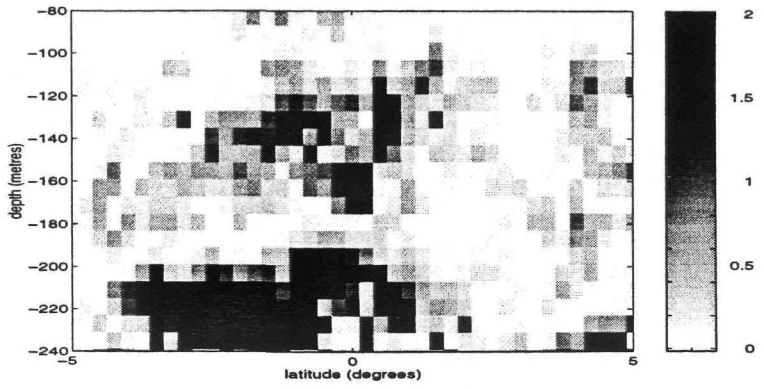

Figure 2.12: Inverse Richardson number calculated using the ADCP velocity and density from SeaSoar measurements for POI section 1.

Figure 2.12 shows the inverse Richardson number for section 1 in the depth interval 80-240 m calculated from the ADCP data and the SeaSoar data on a 4 m grid. The light regions indicate that the Richardson number is high, while the dark regions indicate that the Richardson number is low and that shear generated turbulence is possible. There are two patches of low Richardson number; one centred at 140 m on the Equator, which appears to correspond to a well-mixed layer in the salinity and spice anomaly fields and another at 220 m at 2°S. North of the Equator the Richardson number is generally high. Strong turbulence (which is possible in the regions of low Richardson numbers) may imply that salt finger fluxes are impeded (Linden 1971). It is therefore significant that the Richardson number is generally high.

Figure 2.13 (a) shows the salinity field for the first section of CD32. The layering appears to be better defined during this period than POI1. The spice anomaly (b) shows more clearly the warm, salty layers and the cooler, fresher layers. Close examination of the Turner angle (c) shows that there appear to be alternating diffusive and finger interfaces associated with the intrusions. A comparison of the spice anomaly with the Turner angle suggests that positive/negative spice anomalies in the neighbourhood of the salinity maximum are closely correlated with positive/negative Turner angle, while away from this region a correlation is not obvious. A lagged correlation shows a correlation coefficient of approximately 0.6 over most of the section, which is significant at the 95 % confidence level. The correlation also shows a phase lag of 10 metres, which is not surprising since the Turner angle is maximum at the interfaces and the spice anomaly is maximum at the centre of the intrusive layer.

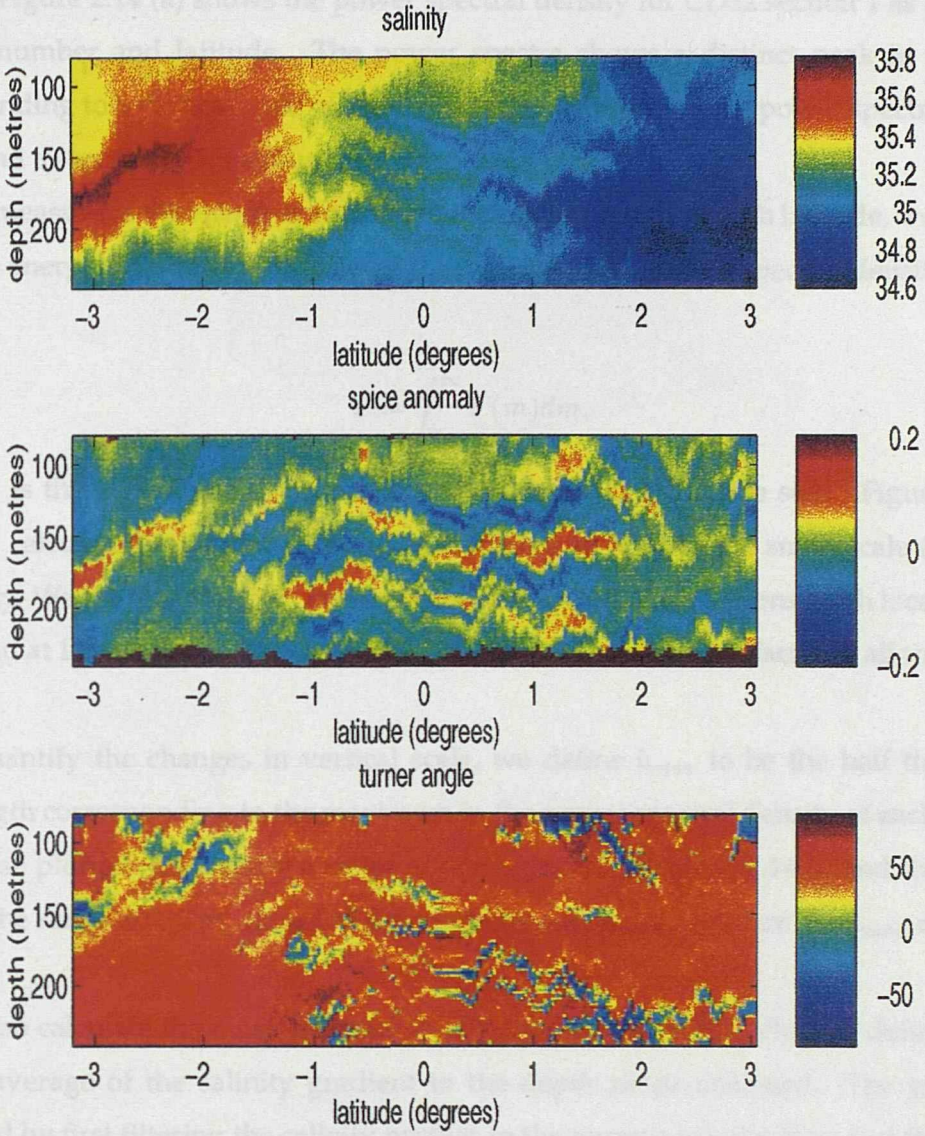

Figure 2.13: [a]Salinity as measured by SeaSoar (upper panel),[b] Spice anomaly (middle panel), [c]Turner angle (lower panel) for CD32 section 1.

2.5 Characteristics of the intrusions

2.5.1 Vertical scales and total spice energy

The spice anomaly is used to estimate the vertical scales of the intrusive features. A one-dimensional Fourier transform was applied to each vertical profile of spice in the section. Figure 2.14 (a) shows the power spectral density for CD32 section 1 as a function of wavenumber and latitude. The power spectra shows a distinct peak in the range corresponding to a vertical scale of 20-30 m with a maximum in the power spectral density at 1°N and a secondary maximum at 1°S.

As a measure of the energy contained in the spice anomaly at each latitude, we calculate the spice energy, E, which is defined as the integral of the power spectral density ($F(m)$), i.e.

$$E = \int_0^\infty F(m)dm,$$

where m is the wavenumber. In practice this integral is a discrete sum. Figure 2.14 (b) shows E calculated for CD32 section 1 and filtered to remove the small scale (<100 km) variability. We see that the spice energy is concentrated in local regions, with local maxima at 1°N and at 1°S. As we will see later, this localization is a common factor in all the sections analysed.

To quantify the changes in vertical scale, we define h_{max} to be the half the vertical wavelength corresponding to the maximum in the power spectral density at each latitude. This is also plotted (divided by a factor of one hundred) in figure 2.14(b) and shows h_{max} to be in the range 20-30 m, except at the southernmost latitude where the h_{max} reaches 40 m.

We also calculate the mean meridional salinity gradient $<\overline{S_y}>$, which is defined as the vertical average of the salinity gradient in the depth range analysed. The gradient is calculated by first filtering the salinity profiles in the meridional direction and then taking a horizontal separation of 100 km when evaluating the gradient. While this is an adequate representation of the large-scale gradient, the maximum value of the local salinity gradient may be underestimated by this quantity by a factor of two. $<\overline{S_y}>$ is plotted in (b) (multiplied by 0.5×10^6). The peaks in the spice energy and the salinity gradient appear to be correlated, which suggests that the features are associated with salinity fronts.

The results of the same calculations for CD32 section 2 are shown in figure 2.15. In this

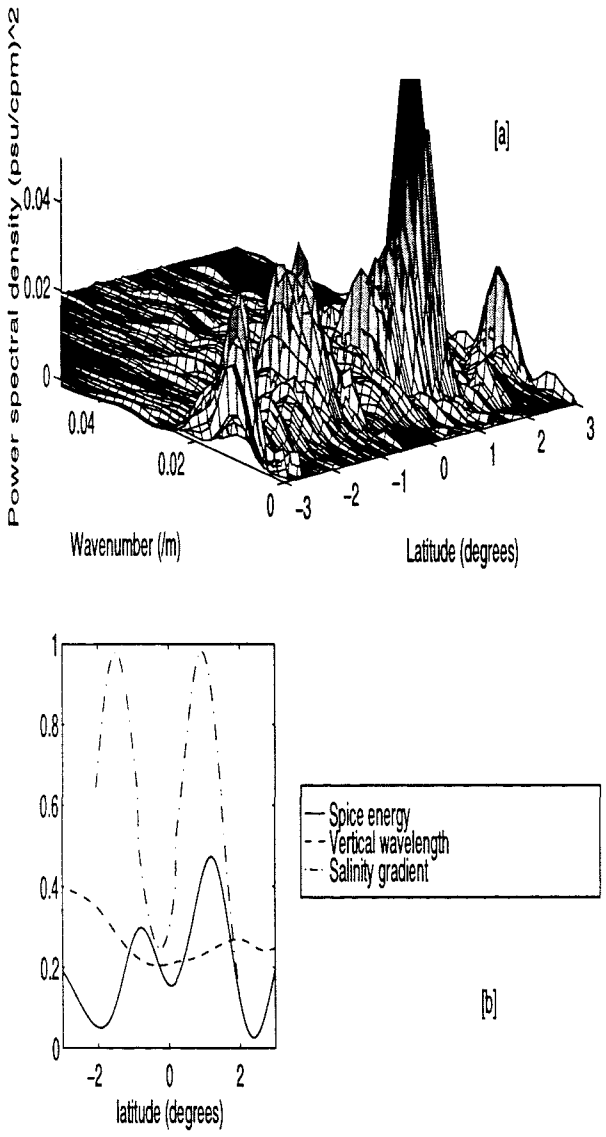

Figure 2.14: [a]Spectrum of spice anomaly (upper panel),[b] Half vertical wavelength, h_{max}, (10^{-2} m) , meridional salinity gradient, $< \overline{S_y} >$, (2×10^{-6} psu m^{-1}) and spice energy, E ((psu/cpm)^2) (lower panel) for CD32 section 1.

section, the peaks in the spice energy have shifted northwards by approximately a degree, to 2°N and 0°N, and appear to be associated with the edge of the region of maximum meridional salinity gradient, which is still situated at 1°N. The second maximum is reduced in magnitude to just above half its previous value. The vertical wavelength is similar to that observed during the previous section. However, in this section there is no clear correlation between the salinity gradient and the spice energy.

This analysis has been repeated for the POI sections (with the exception of sections 8 and 9, when the amount of missing data made the analysis difficult). The maximum depth of the SeaSoar was reduced during sections 10-12 and therefore we changed the depth range of the analysis to 30-190 m. While it is not ideal to include the mixed layer (which may be as deep as 70 m) in the analysis for calculating the spice anomaly, a similar depth interval was chosen for comparison. However, it is worth noting that the Butterworth filter is relatively insensitive to the depth interval over which it is employed. Figure 2.16 shows the spice energy, E, and the vertical wavelength, h_{max}, as a function of latitude for each of the sections.

As for the CD32 sections, there is evidence for localisation of the spice energy; generally with two peaks either side of the Equator and occasionally one centred on the Equator. Qualitatively, the figures suggest that the the position and intensity of the spice energy may persist over 3 sections (sections 1-3 and sections 10-12 are very similar). In table 2.3 we have summarised the mean and maximum spice energy for each section with the approximate time each section was taken. This suggests that the features may be coherent over seven or more days.

There appears to be some evidence for a separation in scales; the peaks in spice energy near the Equator in sections 1-3 are associated with vertical wavelengths of approximately 40 m, while the other peaks are associated with a shorter vertical wavelength O(20-30 m). This shift to a larger vertical scale is probably associated with the region of low Richardson number leading to a well-mixed layer.

Figure 2.17 shows the mean salinity gradient, $<\overline{S_y}>$, and the spice energy, E, for each of the sections. The peaks in spice energy are often associated with the regions of high salinity gradient. Notably, in sections 1-3, the peaks in spice energy near the Equator, which were related to shifts to a larger wavelength, do not appear to be related to maxima in the salinity gradient but to the edges of the maxima. The correlation between the two fields in sections 10-12 is particularly notable. The correlation coefficients between the salinity gradient,

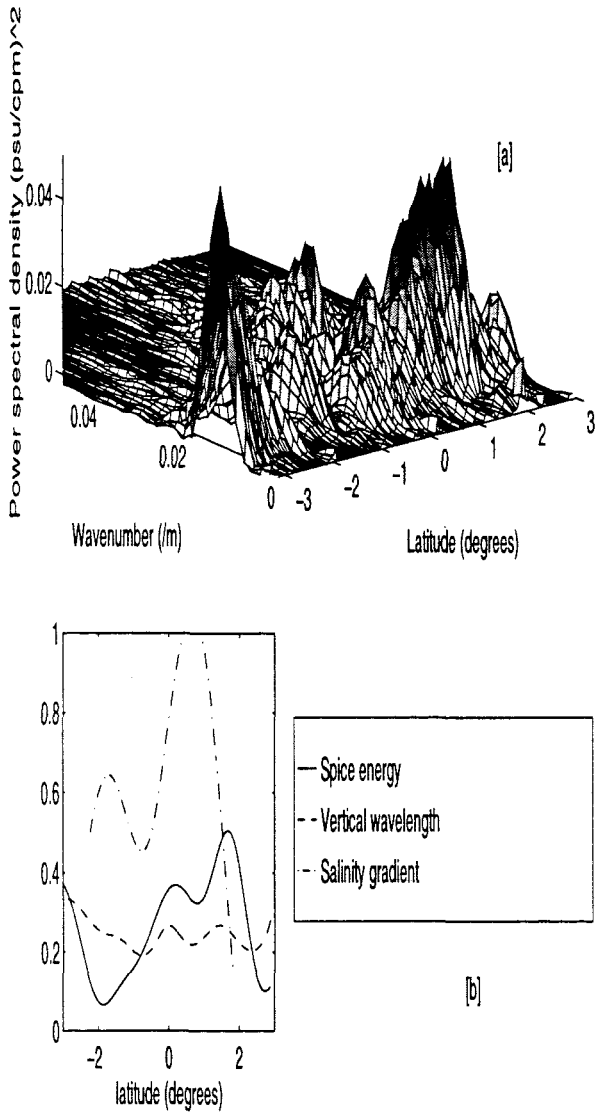

Figure 2.15: [a]Spectrum of spice anomaly (upper panel),[b] Half vertical wavelength, h_{max}, (10^{-2} m) , meridional salinity gradient, $< \overline{S_y} >$, (2×10^{-6} psu m^{-1}) and spice energy, E ((psu/cpm)^2) (lower panel) for CD32 section 2.

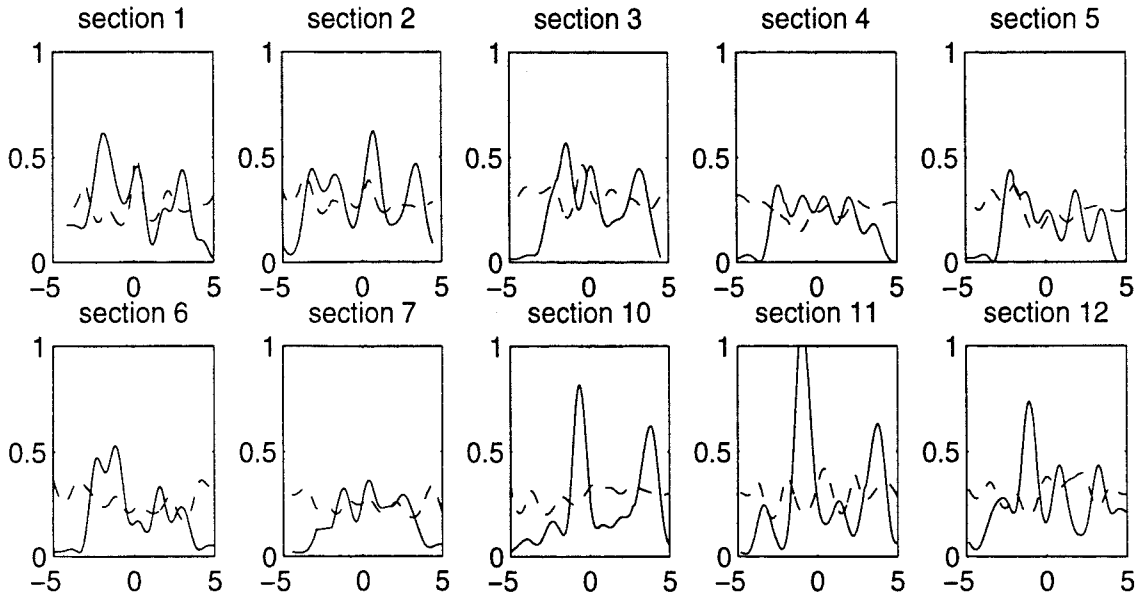

Figure 2.16: Spice energy (solid line) ((psu/cpm)^2) and vertical wavelength (dashed line) ($\times$ 10^{-2} m) as a function of latitude for ten of the POI SeaSoar sections.

Section number	Approximate Julian day at Equator	$\overline{E}$ $(psu/cpm)^2$	E_{max} $(psu/cpm)^2$	Number of layers (>50 km)	$C(E, <\overline{S_y}>)$
1	1	0.2817	0.6151	35	0.2487
2	4.5	0.2989	0.6231	30	-0.4410
3	8.5	0.2511	0.5698	27	0.3194
4	15.5	0.1831	0.3681	44	0.7005
5	18.5	0.1724	0.4398	48	0.1438
6	22	0.1940	0.5294	40	-0.1027
7	25.5	0.1800	0.3621	37	0.4437
10	39	0.2449	0.8164	20	0.1999
11	42.5	0.3012	1.1174	17	0.3131
12	45.5	0.2727	0.7362	18	0.3393

Table 2.3: Summary of the mean and maximum spice energy, the number of layers observed and the correlation coefficient between spice energy and the meridional salinity gradient for each of the POI SeaSoar sections.

$<\overline{S_y}>$, and spice energy, E, varies between -0.44 (for section 2) and 0.70 (for section 4). The variability in the correlation is not surprising given the amount of averaging which each quantity contains.

2.5.2 Meridional coherence

The spice anomaly in figures 2.11 and 2.13 suggests that the features are meridionally coherent over large scales (in particular, larger scales than those associated with similar features at mid-latitudes). It is important to quantify this coherence for two reasons; the first is for comparison with existing theory and the second is for estimating the implied fluxes. In order to do this we have developed a method similar to that described by Graham and Hall (1996), for describing the distribution of bubbles in sonar data. We will outline the method and then discuss the observed meridional coherence.

Feature analysis

The method can be summarised as follows:

1. grid spice anomaly on isopycnals.
2. reduce the spice anomaly to maxima and minima.
3. multiple points defining a single maximum or minimum in the vertical are reduced to a single point.

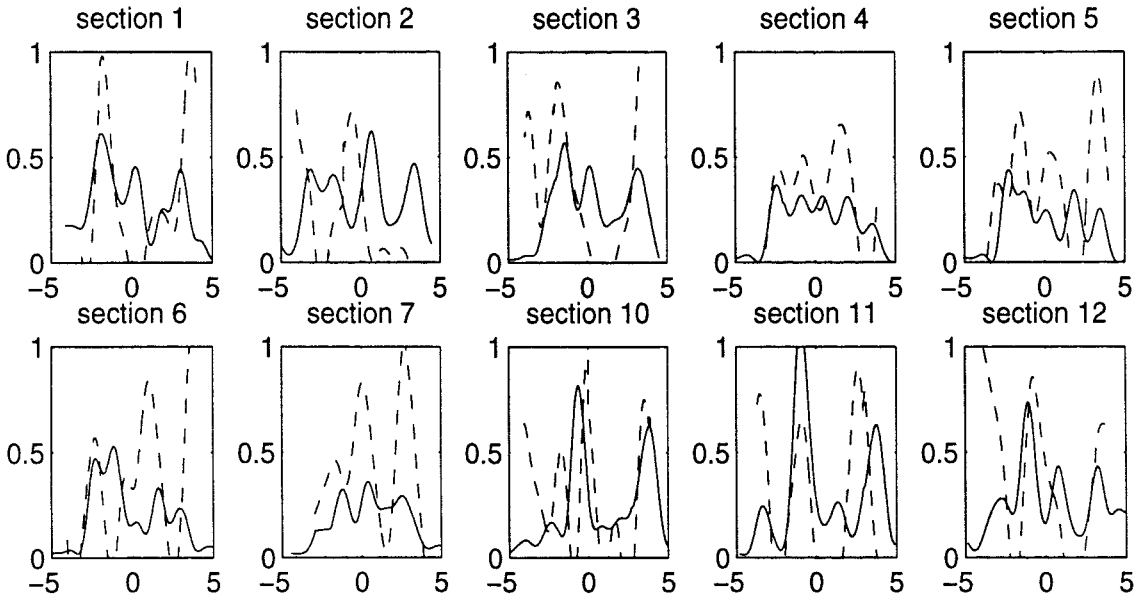

Figure 2.17: Spice energy (solid line) ((psu/cpm)^2) and meridional salinity gradient (dashed line) (2 x 10^{-6} psu/m) as a function of latitude for ten of the POI SeaSoar sections.

4. coherent structures are searched for, moving one grid point in the horizontal and one grid point in the vertical.
5. features with an observed length below the critical level (in this case thirty kilometres) are then discarded.

The results are most sensitive to the discretisation of the densities; in this example, we have used a grid spaced at 0.1 kg m^{-3}. If the grid is made sufficiently fine, features will not be 'connected' within the search radius, while if the grid is sufficiently coarse, positive and negative features will merge. This implies that there is an optimal grid given the horizontal spacing.

Results

Figure 2.18 shows the resulting maps of the features (plotted with potential density as the vertical axis and latitude as the horizontal axis) for (a) section 1 from CD32 and (b) section 1 from POI, with black denoting layers associated with negative spice anomaly and red denoting layers associated with positive spice anomaly. This gives a striking picture of the positions, slopes and lengths of the features. When compared with the previous figures of the spice anomaly, the feature analysis appears to be accurate in highlighting the layers which one would choose by eye.

During POI the layers are localised, with three distinct regions south of the Equator and one north of the Equator. The layers slope both upwards and downwards across isopycnals, but in the region centred at 2°S the layers have a definite slope downwards across isopycnals except for one layer at 24 kg m^{-3}. The isopycnal slopes appear to be consistent with the picture suggested by the CTD profiles in the region of the salinity maximum; there is some indication of finger driven layers rising across isopycnals above the salinity maximum while diffusive layers dominate and sink across isopycnals below the salinity maximum. During CD32 the layers which appear to originate around 2°S slope upwards at densities less than 25 kg m^{-3} and downwards at greater densities. Northwards of this region, the layers are generally oriented along isopycnals, which may suggest either that the vertical fluxes are weaker in this region driving less cross-isopycnal motion or that the features are the result of advection along isopycnals.

In order to quantify the length scales of the observed features and the variability, we have calculated the lengths of the observed features for the CD32 and POI sections. The

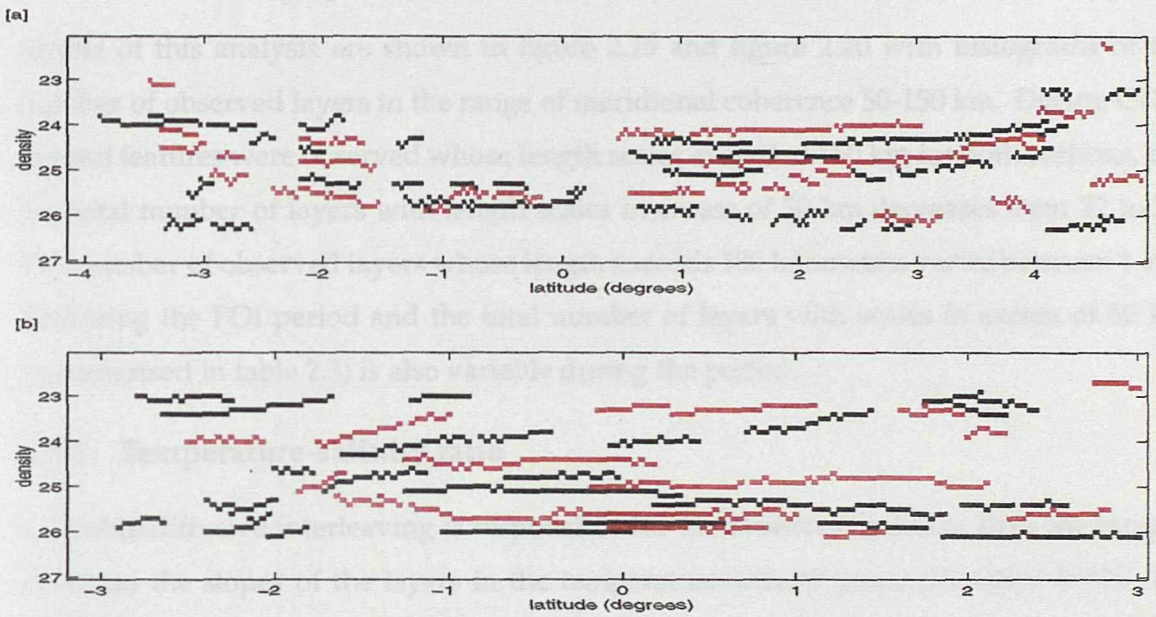

Figure 2.18: [a] shows the positive (black) and negative (red) layers for POI section 1 in latitude-potential density space, [b] shows the layers (with the same colour scale) for CD32 section 1.

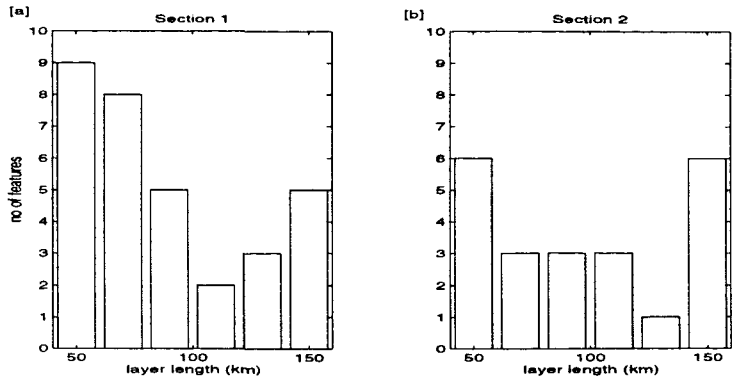

Figure 2.19: Histograms of the distribution of the lengths of coherent meridional structures for the two CD32 SeaSoar sections. The divisions start at 40 km and are in 20 km steps.

results of this analysis are shown in figure 2.19 and figure 2.20 with histograms of the number of observed layers in the range of meridional coherence 50-150 km. During CD32 several features were observed whose length scales exceeded 150 km for both sections, but the total number of layers with length scales in excess of 50 km decreases from 32 to 22. The number of observed layers whose length exceeds 100 kilometres varies between 1 and 10 during the POI period and the total number of layers with scales in excess of 50 km (summarised in table 2.3) is also variable during the period.

2.5.3 Temperature-salinity ratio

If double-diffusive interleaving is responsible for the observed features, then we can put limits on the slopes of the layers in the temperature-salinity plane (Ruddick 1992). Let us consider only the conservation equations for heat and salt and assume a steady-state balance (which may not be appropriate for the timescales involved). If the layers are driven by double-diffusion, then when finger fluxes dominate, the steady-state is described by the equations:

$$\frac{D\theta}{Dt} = v\theta_y + w\theta_z = \gamma_f \frac{\beta}{\alpha} K_s \frac{\partial^2 S}{\partial z^2} \tag{2.4}$$

$$\frac{DS}{Dt} = vS_y + wS_z = K_s \frac{\partial^2 S}{\partial z^2} \tag{2.5}$$

where v and w are the meridional and vertical velocities respectively, K_s is the interface diffusion coefficient for salt and γ_f is the heat to salt flux ratio for salt fingers. The double-diffusive fluxes are represented here by Laplacian terms although this is not strictly necessary. When diffusive fluxes dominate the second equation becomes the equation

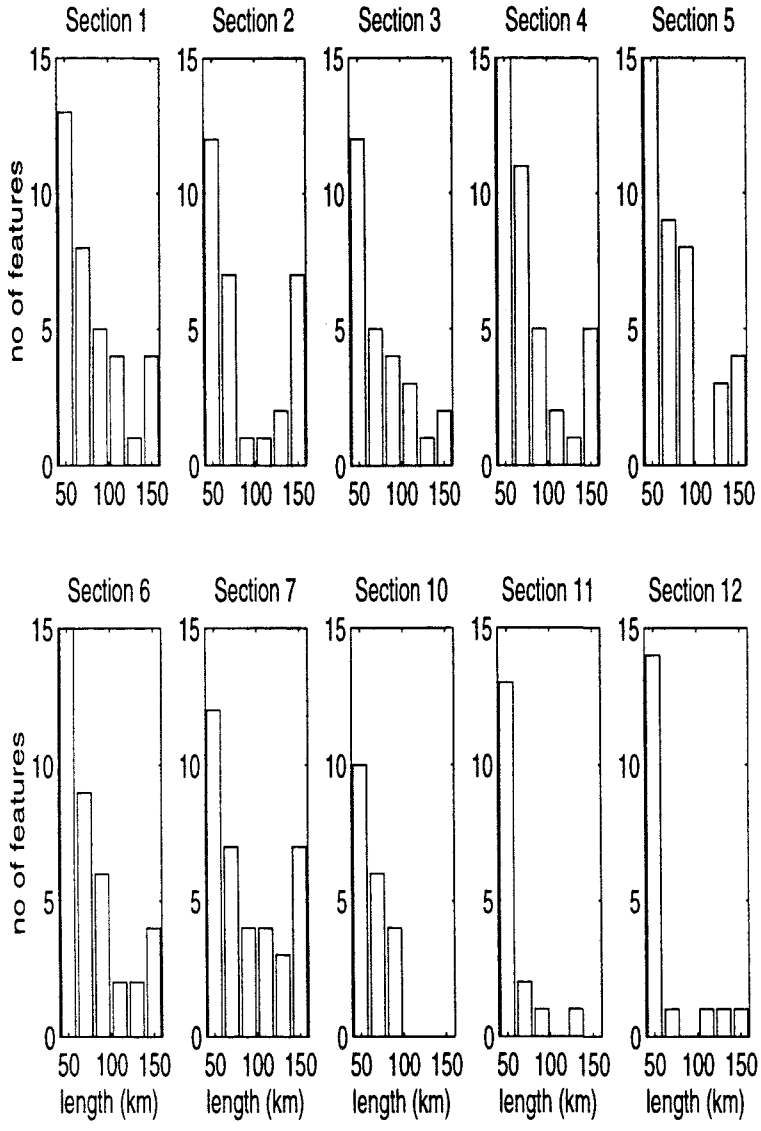

Figure 2.20: Histograms of the distribution of the lengths of coherent meridional structures for ten of the POI SeaSoar sections. The divisions start at 40 km and are in 20 km steps.

for heat and the first equation becomes the equation for salt, with $\gamma_f\beta/\alpha$ replaced by $\gamma_d\alpha/\beta$ (where γ_d is the salt to heat flux ratio for diffusive interfaces). Then the Lagrangian advective ratio should lie between the diffusive flux ratio and the finger flux ratio (Ruddick 1992):

$$\frac{1}{\gamma_d} < \frac{d(\alpha\theta)}{d(\beta S)} < \gamma_f \tag{2.6}$$

or

$$1 - \frac{1}{\gamma_d} < \frac{1}{\rho}\frac{d\rho}{d(\beta S)} < 1 - \gamma_f \tag{2.7}$$

Using the values $\gamma_f = 0.5$ and $\gamma_d = 0.15$ and taking $\rho\beta = 0.765$, this implies that to be consistent with double-diffusive interleaving the ratio should lie in the range:

$$-4.3 < \frac{d\rho}{dS} < 0.38 \tag{2.8}$$

where the lower bound is that for diffusive interfaces dominating and the upper bound is that for finger layers dominating. If turbulent mixing produces intrusions then we might expect that:

$$\frac{d(\alpha\theta)}{d(\beta S)} = R_\rho \tag{2.9}$$

(Schmitt 1994) or

$$\frac{d\rho}{dS} = \rho\beta(1 - R_\rho). \tag{2.10}$$

In the stable regime, R_ρ is less than zero, which would imply that the ratio should be greater than 0.765. In the finger regime, R_ρ is greater than one, which would imply that the ratio should be less than zero. If advection or internal waves produce the features isopycnally, then:

$$\frac{d\rho}{dS} = 0. \tag{2.11}$$

We can attempt to distinguish these mechanisms using both the CD32 and POI SeaSoar data. The data is divided into sets of six profiles and salinity is plotted against density. An example is shown in figure 2.21 [a] for a section between 0.3°S and 0.1°S for CD32. The maxima and minima (the cores of the intrusions) are identified for each profile, as illustrated

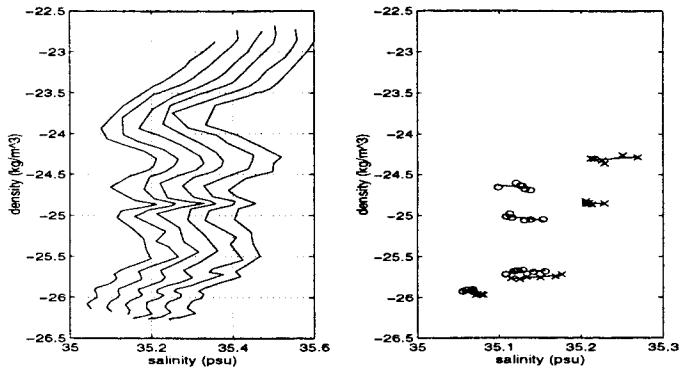

Figure 2.21: [a] shows the six salinity profiles from CD32 SeaSoar section 1 (0.3°S - 0.1°S) plotted against density with an offset of 0.05psu for each profile (left panel). [b] shows the salinity maxima (x) and minima (o) plotted and joined with the line of best fit in the least squares sense (right panel).

Latitude range	Max/ min	Density	Ratio	95% c.i.
-0.3S - -0.1S	+	24.30	-0.7382	1.3869
-0.3S - -0.1S	+	24.85	0.4304	1.4897
-0.3S - -0.1S	+	25.75	-0.6913	0.4496
-0.3S - -0.1S	+	25.97	0.2602	1.5609
-0.3S - -0.1S	-	24.70	0.8215	2.1755
-0.3S - -0.1S	-	25.00	1.2779	1.2300
-0.3S - -0.1S	-	25.60	-0.3383	1.0331
-0.3S - -0.1S	-	25.92	-0.3222	2.6040

Table 2.4: Summary of ratios calculated between 0.3°S and 0.1°S for CD32 section 1.

in [b]. A straight line is then fitted to the points corresponding to the same intrusion (with a least squares fit) and the ratios of the intrusions are then calculated. These are then compared to the theoretical limits. The results for this example are summarised in table 2.4, with the confidence limits. The results for POI (and particularly the rather large confidence intervals) are similar to those which have been obtained for CD32.

In figure 2.22 we show the results (ignoring the confidence intervals) as a histogram for [a] CD32 section 1 (between 1°S and 1°N) and [b] POI section 1 (between 2.7°S and 0°N). The histograms both show two peaks; one for a ratio less than zero but consistent with double-diffusive interleaving and one for a ratio greater than zero and outside the upper limit given by double-diffusive processes. If isopycnal advection were responsible for the observed features, then we would expect the histograms to show a peak at a ratio of zero

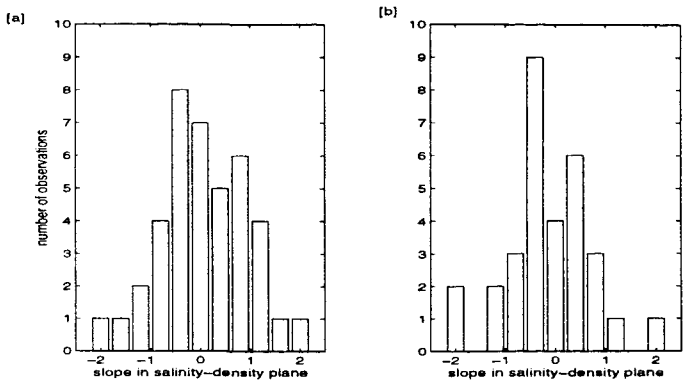

Figure 2.22: [a] histogram of ratios calculated for intrusions in CD32 section 1 (between 1°S and 1°N). [b] histogram of ratios calculated for intrusions in POI section 1 (between 2.8°S and 0°N).

(see equation 2.11). The combined results for CD32 and POI indicate that approximately 60% of the observed intrusions have ratios consistent with double-diffusive interleaving. If we discount those features which are not consistent with the hypothesis, then the ratio is -0.53 ± 0.57 kg m^{-3} psu^{-1} for CD32 and -0.63 ± 0.79 kg m^{-3} psu^{-1} for POI. The standard deviations indicate that there is a large range in the observed ratios. The layers are either driven by the diffusive interface (equation 2.8) or by the effects of turbulence (equation 2.10) with a value of $R_\rho \approx 2$, which is in the finger regime. The observations which are not consistent with double-diffusive interleaving give a ratio of 0.94 kg m^{-3} psu^{-1} for CD32 and 1.00 kg m^{-3} psu^{-1} for POI. Turbulence could be responsible for the features, with a value of $R_\rho \approx$ -0.4, which is in the stable regime. It is unclear how features produced by double-diffusive interleaving will subsequently interact with turbulence and internal waves. This may lead to the structures we observe being more complicated than theory suggests.

The criticism of this analysis is that the confidence interval is large enough to include all the above mechanisms and the null hypothesis of random Gaussian ratios cannot be rejected. The large uncertainties may be due in part to the gridding of the SeaSoar data and a similar analysis performed on closely spaced CTD stations might be more accurate. The analysis is not inconsistent with the other evidence (also highly suggestive of diffusive layers) but should be given less weight.

2.5.4 Zonal scales

So far we have looked only at the meridional sections. This enables us to study the features in the cross-front direction (meridional-vertical plane) but this can be misleading and it is easy to forget that the features are in fact three-dimensional. We will attempt to redress the balance and consider the zonal scale of the features.

During CD32 the SeaSoar was towed along a 'butterfly' grid. We have picked one of the zonal sections from this survey which covered a 70 km section. Figure 2.23 shows the spice anomaly plotted against depth and longitude. Most of the features in the spice anomaly appear to be coherent over the whole section. This is confirmed by applying the image analysis technique of the previous section. The results of this are shown in figure 2.24. At least three layers appear to be coherent over the total section with many other layers merging and splitting. This implies that their scale is at least 70 km in the zonal direction, which is of the same order of magnitude as the meridional scales. This differs from the results of Gregg (1980), who was able to map an intrusion in three dimensions and found that the intrusions had a greater cross-front scale than along-front scale. Is it possible that during subsequent POI sections we will observe the same features? Assuming that features are advected eastward by the EUC with a velocity of 50cm s^{-1} and the time between Equator crossings is 3 days, then, if the layers have a zonal scale in excess of 130 km, it is likely that the same features may be sampled more than once. This inference of the persistence of features is in agreement with the spice energy profiles from both CD32 and POI which suggested that the broad features of the finestructure were persistent on timescales O(10 days).

2.5.5 Summary

In the above analysis, several results suggest that double-diffusive interleaving is playing a role in the production of the observed features. These are:

- the Turner angle is observed to lie in the finger and diffusive regimes.
- the regions of high spice energy appear to be related to thermohaline gradients.
- the intrusions are observed to cross isopycnals.
- the intrusion ratios are consistent with double-diffusive fluxes driving over 50% of the intrusions.

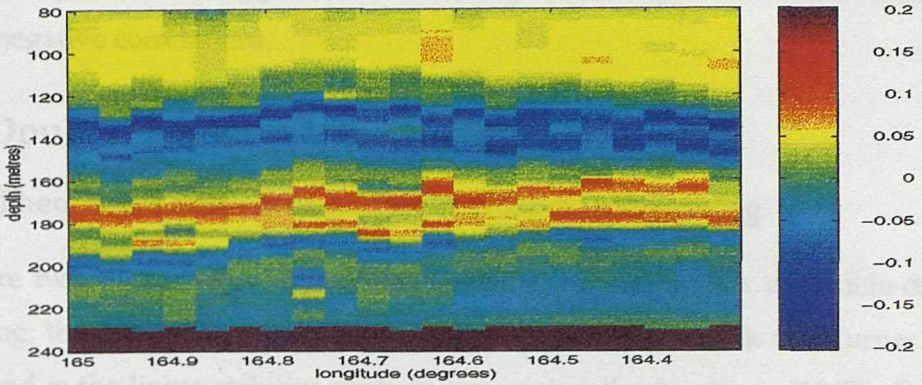

Figure 2.23: Spice anomaly as a function of longitude and depth during one zonal section of the CD32 survey.

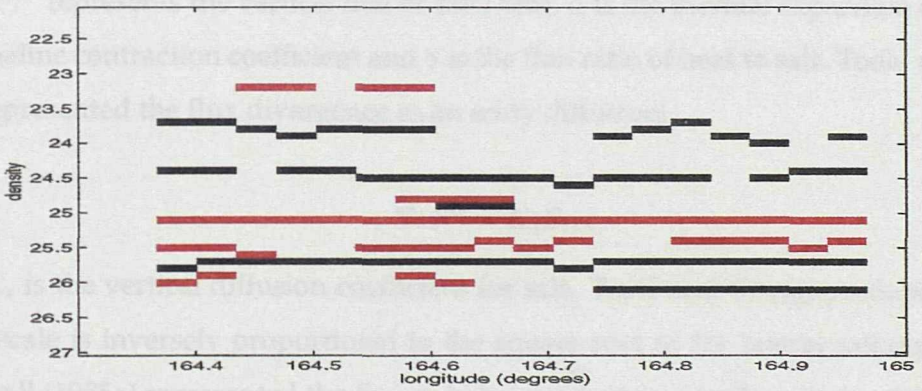

Figure 2.24: Positive (black) and negative (red) layers as a function of longitude and potential density during the same zonal section of the CD32 survey.

- the correlation between density anomaly and spice anomaly is consistent with both finger and diffusive regimes. In particular, during POI the correlation is generally positive in the region of the salinity front. Given that layers sink across isopycnals in this region this is suggestive of diffusively driven layers (advection would produce a negative correlation).

2.6 Double-diffusive interleaving

2.6.1 Theoretical models of double-diffusive interleaving

There are two classes of models which describe the mechanism of double-diffusive interleaving; the first is the energy argument proposed by Ruddick and Turner (1979) and the second is the linear stability analysis approach following Stern (1967). Ruddick and Turner assume that intrusions will redistribute heat and salt via finger fluxes but energy will be conserved. This argument predicts a vertical scale for the features which depends linearly on the lateral salinity gradient. The second class of models are based on a linear stability theory assuming smooth isopycnal gradients of heat and salt. Isopycnal surfaces are assumed to be initially horizontal and the system is at rest. The vertical fluxes of heat and salt are parameterised in such a way as to represent double-diffusive fluxes, i.e.

$$\alpha F^T = \gamma \beta F^S$$

where $F^{S,T}$ represents the vertical flux of salt/heat, α is the thermal expansion coefficient, β is the saline contraction coefficient and γ is the flux ratio of heat to salt. Toole and Georgi (1981) represented the flux divergence as an eddy diffusion:

$$-\nabla.F^S = K_s S_{zz}, \tag{2.12}$$

where K_s is the vertical diffusion coefficient for salt. Toole and Georgi predicted that the vertical scale is inversely proportional to the square root of the lateral salinity gradient. McDougall (1985a) represented the flux as being proportional to the salinity difference

$$-\nabla.F^S = -BmS' \tag{2.13}$$

where m is the vertical wavenumber and B is a coefficient for the vertical flux of salt. Using this formulation McDougall predicted that the vertical scale is inversely proportional to the lateral salinity gradient.

The functional form of the scales predicted by the two classes of models (the energy argument model and the linear stability models) is very different but depends on the same parameter - the lateral salinity gradient. Niino (1986) suggested from numerical experiments that the results can be reconciled by considering the frontal width; the Ruddick and Turner result is applicable to a narrow front, while the linear stability analysis results are applicable to wider fronts. Kuz'mina (1990) has extended the linear stability analysis by looking for solutions which are the superposition of two disturbances. This represents features which have a quasiperiodic structure in the cross-front direction with scales smaller than the frontal width and predicts vertical scales with the same functional form as the Ruddick and Turner mechanism. McDougall (1986) has shown however, that for heat and salt the Ruddick and Turner mechanism would not develop alternating finger and diffusive interfaces and that most oceanic intrusions (such as those described above) must have their origins in smooth thermoclinic fronts. If a front which is initially diffuse (or smooth) does not develop intrusions then the front will sharpen and the Ruddick and Turner mechanism should take place. Finally, if, as the front sharpens, double-diffusive interleaving does not develop, the kinematic process described by Onken et al. (1990) will ensue. Woods et al. (1986) showed that intrusions could be produced simply by differential advection of temperature along isopycnals. However, the numerical results only show one intrusion in the frontal zone, which is unlikely to account for the multiple structures which are commonly observed.

2.6.2 Comparison with theory

The linear stability theory for double-diffusive interleaving (Richards 1991) predicts the growth rate, the vertical wavelength and the meridional 'trapping' scale for the fastest-growing intrusions. While other models of this type assume that f, the Coriolis parameter, is constant, the introduction of variable $f = \beta_{eq} y$ results in a so-called 'trapping' scale. These variables can be expressed in dimensional terms as:

$$\lambda = \frac{N \epsilon_y}{4 \sigma_{pr}^{\frac{1}{2}}} \tag{2.14}$$

$$h = \pi \frac{4 B \sigma_{pr}^{\frac{1}{2}}}{N |\epsilon_y|} \tag{2.15}$$

$$\psi = \left(\frac{2D}{|\epsilon_y| \beta_{eq}} \right)^{\frac{1}{2}} \tag{2.16}$$

when the McDougall parameterization for the fluxes across interfaces is used (equation 2.13), and:

$$\lambda = \frac{N\epsilon_y}{4\sigma_{pr}{}^{\frac{1}{2}}} \tag{2.17}$$

$$h = \pi\left(\frac{4K_s\sigma_{pr}{}^{\frac{1}{2}}}{N|\epsilon_y|}\right)^{\frac{1}{2}} \tag{2.18}$$

$$\psi = \left(\frac{K_v N\sigma_{pr}^{\frac{1}{2}}}{|\epsilon_y|\beta_{eq}{}^2}\right)^{\frac{1}{4}} \tag{2.19}$$

when the Laplacian formulation for the interface fluxes is used (equation 2.12), where λ is the growth rate, h is the vertical scale and ψ is the meridional 'trapping' scale, D is the coefficient for the vertical flux of momentum in the McDougall parameterization, K_v is the vertical diffusion coefficient for momentum in the Toole and Georgi formulation, σ_{pr} is the Prandtl number and N is the buoyancy frequency. The non-dimensional salinity gradient, ϵ_y, is given by:

$$\epsilon_y = \frac{(1-\gamma_f)g\beta\overline{S_y}}{N^2}$$

for finger driven layers, and

$$\epsilon_y = \frac{(1-\gamma_d)g\beta\overline{S_y}}{N^2}$$

for diffusive driven layers (using the transformation given by Ruddick and Walsh (1994) and taking $\alpha\theta_y = \beta S_y$). Richards (1991) compared the scales of the features observed during CD32 to those predicted for finger driven layers. In light of the previous section it appears that this is not an appropriate comparison, and instead we should use the scales predicted for the diffusive layers.

Table 2.4 summarises the predicted scales for diffusive layers with values of $|\epsilon_y|$ and N typical of those observed during CD32 and TOGA-COARE and compares them with the predicted scales. We define the averaged salinity gradient, $\overline{S_y}$, for computing the non-dimensional salinity gradient, ϵ_y, as the maximum value of the filtered salinity gradient at the depth of the salinity maximum. This is the large-scale gradient suggested by Toole and Georgi (1981) but different from the value used by Richards (1991), whose quoted value for the non-dimensional salinity gradient for CD32 is a factor of three larger than the gradient calculated here. We have taken $\sigma_{pr} = 0.1$, $K_s = 3\text{x}10^{-5}$ m^{2}s^{-1} and $B = 1\text{x}10^{-5}$.

Parameter	Observed	Predicted	
		McDougall	Laplacian
N	$0.02\ s^{-1}$		
ϵ_y	$7x10^{-5}$		
ψ		35 km	28 km
h	$27 \pm 3m$	33 m	16 m
λ^{-1}		10 days	10 days

Table 2.5: Observed and predicted scales for diffusive-driven layers.

The observations are in reasonable agreement with the predictions given the uncertainty in the appropriate salinity gradient, the Prandtl number and the diffusion coefficients. These uncertainties suggest that it is difficult to discriminate between the two representations of the interface fluxes. Taking the same large-scale gradients and assuming finger fluxes dominate, reduces the value of ϵ_y by a factor of 0.6. This increases the e-folding time (by a few days) and also the layer thickness and the trapping scale.

2.7 Discussion

The work presented here has documented the characteristics of intrusive features in the thermocline of the Equatorial Pacific during two periods which were characterised by distinct ocean states and separated by almost four years; the broad characteristics of the features were similar. The high resolution SeaSoar measurements allowed a two-dimensional picture to be presented which highlighted not only the regular vertical scale of the features, but also the meridional coherence. The correlation of the spice anomaly and the density anomaly in some regions, the double-diffusive nature of the Turner angle on interfaces and the coincidence of regions of high spice energy and large thermohaline gradients suggested that the intrusions may be driven by double-diffusion. The intrusion slopes and flux ratios appear to suggest that the diffusive interface may dominate the vertical fluxes.

McDougall (1985a) suggested that high resolution SeaSoar measurements, such as those which have been described, should allow us to test the analytic theory for processes such as double-diffusive interleaving. We have shown that in practice it is difficult to distinguish between different mechanisms near the Equator. We suggest that at least 60% of the features observed near the salinity front can be explained by double-diffusive interleaving. Toole's conclusion that internal waves (or advection) may also be responsible for the production

of finestructure is reiterated here. The observed scales of the features are close to the scales predicted by the linear stability analysis for double-diffusive interleaving. It would be coincidental if internal waves are imposing a vertical scale on the features as suggested by Toole and Georgi (1981).

McPhaden (1985) suggested that the bowing of the isopycnals, associated with the meridional circulation and the EUC, may provide a source of available potential energy for the instability associated with the intrusions. There has been very little theoretical work on baroclinic instability near the Equator (Philander 1990), but given the Charney model for baroclinic instability on a beta plane, it is possible to find a latitude, y_o, for which the predicted scales would agree with the scales of the features we observe (in this case the appropriate latitude would be one or two degrees away from the Equator). However, in this model the vertical scales of the features would decrease to zero as the Equator was approached, which is not consistent with observations.

Will the background shear and turbulence reduce the heat and salt fluxes across double-diffusive interfaces? At low Richardson number, heat and salt transfer by salt fingers is impeded (Linden 1971) and therefore, the source maintaining interleaving may no longer be present if salt fingers dominate over diffusive interfaces. While at high Richardson number we may expect that double-diffusion dominates. The only regions where we observe low Richardson number, in the depth ranges which have been analysed, are at 140 metres centred at about 0.5°N and south of the Equator below 200 metres. This may suggest that double-diffusive interleaving will be impeded in these regions.

Kuz'mina and Rodionov (1992) have included baroclinicity in their linear stability analysis for double-diffusive interleaving (although their analysis is somewhat different from the usual linear stability models). They introduce a parameter ϕ defined:

$$\phi = \frac{\delta}{\epsilon_y}. \tag{2.20}$$

where $\delta = \rho_y/\rho_z$ is the isopycnal slope. For $\phi \ll 1$ (large Richardson number), the instability is dominated by double-diffusive interleaving, while for $\phi \gg 1$ the intrusions are driven by baroclinic instability. Given the typical values of δ and ϵ_y in the Western Equatorial Pacific, this suggests that ϕ is O(1). Hence one might conclude that the observed interleaving may be the result of both baroclinic and thermohaline effects.

Even if other instabilities are taking place and acting to stir the field, it is probable

that double-diffusive interleaving is acting to mix the water masses. It is encouraging that we have found some evidence which supports double-diffusive interleaving despite the fact that the background state is rapidly varying in time and strongly sheared in both the horizontal and the vertical (which may explain some of the inconsistencies). We believe that an analysis of the full problem is required, including both baroclinic instability, double-diffusive interleaving and internal waves to establish the relative importance of the various contributions, since observations do not seem able to answer the many remaining questions. The complexity of the three-dimensional field suggests that this will only be possible through the use of a numerical model.

Chapter 3

Heat and salt fluxes produced by interleaving and their parameterization

3.1 Introduction

In large-scale numerical models of the ocean, the fluxes of heat, salt and momentum can only be explicitly modelled for processes that are resolved by the model grid. Fluxes produced by smaller scale processes must be parameterized. The sensitivity of the large-scale dynamics of the Equatorial Pacific to the representation of these parameterized fluxes (for example Maes (1996) and Schneider and Muller (1994)) suggests the importance of parameterizing the fluxes based on sound physical principles.

In the previous chapter we have examined the characteristics of the intrusive features in the thermocline of the Equatorial Pacific and the mechanism responsible for the features. We have shown that double-diffusive interleaving may be responsible for a significant proportion of the intrusive features which are observed in the thermocline of the Equatorial Pacific. The cross-frontal exchange of heat and salt effected by the intrusive features may be significant, as suggested by Stommel and Federov (1967), and these lateral fluxes are our primary concern; how important are the fluxes produced by interleaving and how should the fluxes be parameterized for large-scale numerical models?

Work on estimating lateral fluxes produced by interleaving began with Joyce (1977), who quantified the cross-frontal exchange by separating the small, medium and large scales of motion. We will consider a model similar to Joyce (1977), but extend it to produce a parameterization of interleaving induced fluxes in terms of the large-scale variables. To establish the importance of representing the fluxes produced by interleaving in a large

scale model, we need to compare estimates of the interleaving fluxes with those of the fluxes produced by other processes whose scales are not resolved by large scale models (e.g. mesoscale eddy motions).

The vertical fluxes have been examined by two previous authors; both Garrett (1982) and McDougall (1985b) have discussed the parameterization of the vertical fluxes due to double-diffusive intrusions in large-scale numerical models and we will briefly revisit their results here.

In chapter 1 we briefly outlined a method for modelling the fluxes in terms of a diffusion coefficient. To reiterate the introduction given there, we can represent the flux of a tracer, τ, in terms of a diffusion coefficient, κ:

$$\overline{u_i{}'\tau'} = -\kappa \frac{\partial \tau}{\partial x_i}. \tag{3.1}$$

This is the approach which will be taken here. Also in chapter 1 we summarised the estimates of the lateral diffusion coefficient in the Equatorial Pacific. While an estimate of the magnitude of the diffusion coefficient is useful, it is not obvious that the diffusion coefficient, κ, should be constant. We would like to be able to represent the diffusion coefficients due to double-diffusive interleaving in terms of the large-scale fields. This might be considered to be analogous to the work of Green (1970) and Stone (1972) in relation to baroclinic eddies, who prescribed the diffusion coefficient for tracers in terms of a velocity scale and a length scale. Of course, the use of a diffusive-like parameterization may be inappropriate. An alternative approach is to consider an advective-like parameterization (e.g. Gent and McWilliams (1990))

In section 3.2 we will estimate the fluxes of heat and salt produced by interleaving. These values will be compared with those produced by mesoscale eddies, calculated from mooring data in the Western Equatorial Pacific. In section 3.3 we will review the finite amplitude model of McDougall (1985b) which will be used with the results from Richards (1991) to develop a scheme for the parameterization of the fluxes produced by intrusions. Finally, in section 3.4 we will discuss the results and the possible implications.

3.2 Estimates of lateral fluxes

3.2.1 Fluxes produced by interleaving

Following the approach of Joyce (1977), we assume that medium-scale motions (at the intrusion scale) are produced by small-scale mixing across the double-diffusive interface. If layers are in a quasi-steady state then there will exist a balance between the vertical diffusion across the interface and the (almost) lateral advection along the layer:

$$\underbrace{v' \frac{\partial S}{\partial y}}_{medium-scale} \approx \underbrace{A_s \frac{\partial^2 S}{\partial z^2}}_{small-scale}$$

where A_s is the vertical diffusion coefficient and v' is the advective velocity along the layer. The vertical advection term ($w'S_z$) is assumed to be small. Taking A_s to be 3×10^{-5} $m^2 s^{-1}$ (Ruddick and Hebert 1988), dz to be 20.0 m, ΔS to be 0.2 psu and dy to be 150 km gives an estimate of v' of 0.01 m s^{-1}. If v' and S' are perfectly correlated (a reasonable approximation for intrusions), then we can estimate $\overline{v'S'}$ to be 0.002 psu m s^{-1} (implying $\overline{v'\theta'} \approx 0.006$ ^{o} C m s^{-1} with $\beta/\alpha \approx 3$). Assuming that the layers are diffusive in nature, we can estimate the lateral diffusion coefficient, A_{HS}, via the formulation given in equation 3.1. Taking S_y to be 2×10^{-6} psu m^{-1} and substituting for $\overline{v'S'}$ gives a value for A_{HS} equal to 1.0×10^3 $m^2 s^{-1}$. This value of the lateral diffusion coefficient, A_{HS}, is the same order of magnitude as the values which have been estimated by other authors and summarised in table 1.1.

With the meridional extent of the layers in excess of 100 kilometres in regions, the value of the intrusion velocity, v', suggests that layers take approximately 100 days to grow to finite amplitude. In the Equatorial Undercurrent (EUC), the typical eastward velocity is O(0.5 m s^{-1}), which implies that if layers start to grow at the origin of the EUC, close to the Indonesian throughflow, they will be at finite amplitude approximately 50 degrees longitude from the source. This suggests that, assuming a steady Undercurrent, the layers observed and documented in the previous chapter are newly formed and still growing. However, the estimate for v' is really only an order of magnitude estimate and an increase in v' by a factor of two or three (due to the uncertainty in the appropriate value of A_s) would significantly reduce the growth time and imply that the layers we observe are at finite amplitude.

Cross-equatorial salt flux

Taking the estimated values of $\overline{v'S'}$, we can estimate the meridional (across the Equator) freshwater flux, F_{fw}, due to interleaving as:

$$F_{fw} = -\int_{west}^{east}\int_{z_o}^{z_1}\frac{\overline{v'S'}}{S_o}dzdx$$

where the vertical extent of the layer is defined as the distance z_o to z_1, $west$ and $east$ are the zonal boundaries and S_o is the background salinity. Then taking $z_1 - z_o$ to be 40 metres (assuming only two opposing layers exist at any time), $east - west$ to be 1 x 10^7 metres (the zonal extent of the Pacific basin) and S_o to be 36 psu, we obtain an estimate of 0.02 Sv directed southwards. This value should be compared with the estimates of Baumgartner and Reichel (1975) who estimate a total freshwater flux of 0.78 Sv southwards and Wijffels et al. (1992) who estimate a freshwater flux of 0.02 Sv plus the flux of the Indonesian throughflow (which is uncertain) directed northwards. While the total freshwater flux due to the interleaving cannot account for a large proportion of the freshwater flux, it certainly cannot be discounted as a mechanism contributing to the total flux.

3.2.2 Comparison with fluxes produced by mesoscale eddies

To compare the estimates of the fluxes of heat and salt produced by interleaving with the fluxes produced by eddylike motions we have followed the approach of Lukas (1987) and Bryden and Brady (1989). These authors estimated the eddy fluxes of heat and momentum from mooring data in the Central and Eastern Equatorial Pacific respectively. We will focus on a 421 day time series at 156°E from 12th March 1993 to 27th April 1994.

The temperature measurements derive from the TAO mooring with thermistors at 50, 75, 100, 125, 150, 200 and 250 metres averaged daily and the velocity measurements derive from an upward looking ADCP corrected for variations in the sound velocity, averaged daily and into 5m bins (we will utilise only the measurements at the same depth as the thermistors). Figure 3.1 shows the mean profiles of zonal velocity, meridional velocity and temperature. The maximum in the zonal velocity is associated with the EUC at a depth of 200m. Temperature measurements were sparse at depths of 125 m and 250 m and therefore we will not discuss the eddy fluxes for those depths.

In the upper three panels of figure 3.2 we show the zonal velocity, meridional velocity and temperature records at a depth of 150 m in the thermocline. The zonal velocity has

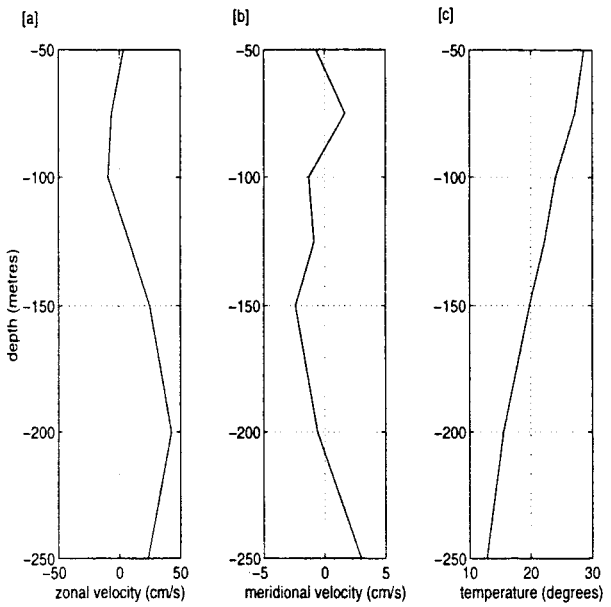

Figure 3.1: [a] Mean zonal velocity, [b] mean meridional velocity and [c] mean temperature profile for the mooring located on the Equator at 156°E from March 12th 1993 to April 27th 1994.

a strong seasonal cycle which is not apparent in either the temperature or the meridional velocity record. In order to remove this seasonality we have low-pass filtered the records with a 146 day cut-off (Lukas 1987). The record can now be divided into two parts:

$$u = u_s + u_{hf}$$

where u_s is the fluctuating seasonal signal and u_{hf} is the fluctuating high frequency signal on timescales shorter than 146 days. The records of meridional velocity and temperature have also been filtered although the seasonal signal in these records is much smaller. With the seasonal and high frequency signal separated, we have calculated the eddy kinetic energy, the directionality, the eddy momentum and heat fluxes and their skewness and the integral timescales. The eddy kinetic energy is defined:

$$KE = \frac{1}{2}(\overline{u'^2} + \overline{v'^2})$$

,the directionality is defined:

$$d = \frac{\overline{u'^2}}{\overline{v'^2}}$$

and the integral timescales (Davies 1976) are calculated:

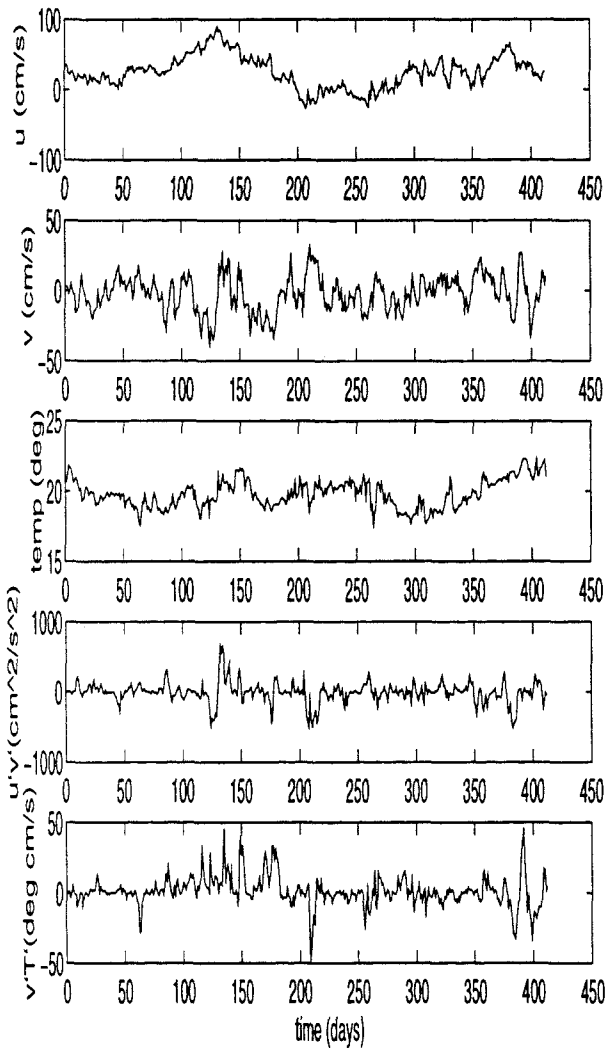

Figure 3.2: Upper panel shows the zonal velocity, second panel shows the meridional velocity, third panel shows the temperature, fourth panel shows the momentum fluxes and lower panel shows the heat fluxes for the mooring located on the Equator at 156°E at a depth of 150 m from March 12th 1993 to April 27th 1994.

$$\tilde{\tau} = (1 + 2\sum_{i=1}^{M} C_{u'}(i\Delta t)C_{v'}(i\Delta t))\Delta t$$

where C is the autocorrelation and M is chosen such that $\tilde{\tau}$ does not increase when M is increased. It should be noted that the use of integral timescales can be dubious (Davis et al. 1996).

The results are tabulated in table 3.1, where the subscript s refers to the seasonal contribution, hf refers to the high frequency contribution and no subscript refers to the total.

depth		50m	75m	100m	150m	200m
KE	$(10^{-2}ms^{-1})^2$	823	696	519	348	131
KE_s	$(10^{-2}ms^{-1})^2$	344	346	293	182	41
KE_{hf}	$(10^{-2}ms^{-1})^2$	472	365	189	141	74
d		4.00	3.13	4.57	3.18	1.59
d_s		13.82	32.97	298	23.56	8.76
d_{hf}		2.35	1.37	1.10	0.84	0.66
$\overline{u'v'}$	$(10^{-2}ms^{-1})^2$	-91.85	-143.80	-86.59	-42.15	-41.99
$\overline{u'_s v'_s}$	$(10^{-2}ms^{-1})^2$	-109.99	-81.66	-10.65	-14.48	-21.29
$\overline{u'_{hf} v'_{hf}}$	$(10^{-2}ms^{-1})^2$	-23.64	-38.09	-57.60	-10.73	-9.69
$skew_{hf}$		0.63	-0.25	-2.62	-0.22	-0.57
$\tilde{\tau}$	days	9.06	7.04	5.70	9.35	11.18
$\overline{v'T'}$	10^{-2} °C m s^{-1}	5.24	7.14	0.60	2.08	-0.26
$skew$		0.22	0.31	0.53	0.22	-0.81
$\tilde{\tau}$	days	13.05	8.23	4.90	9.37	11.36

Table 3.1: Table of calculated variables at each mooring depth. See text for definition of the variables.

The total eddy kinetic energy exhibits a maximum in the near surface waters decreasing with depth and is almost equally partitioned between its seasonal and high frequency components. However, the seasonal eddy kinetic energy is highly anisotropic (as shown by its directionality) and dominated by the zonal component while the high frequency energy is almost isotropic ($d \approx 1$). This is similar to the pattern which is observed in the central Equatorial Pacific. In contrast, the eddy momentum fluxes suggest a different scenario; the fluxes are always negative which is indicative of a northward flux of westward momentum or a southward flux of eastward momentum and are largely dominated by the seasonal component. The timeseries in figure 3.2 shows that the fluxes are intermittent with the skewness suggesting that the events were skewed towards negative excursions. The

integral timescales calculated are longer than those at other longitudes varying between 6 and 11 days (Lukas reported eddy time scales between 3 and 9 days at 152°W and Bryden and Brady reported eddy time scales between 4 and 7 days at 110°W). However, the records did not exhibit any dominant frequencies when spectra were calculated. Similar integral timescales are also observed for the eddy heat fluxes which above 200 m are predominantly positive and skewed towards positive excursions, indicating northward heat fluxes. The eddy heat fluxes which are significantly different from zero at the 95% confidence interval are those at 50, 75 and 150 m. The eddy heat and momentum fluxes are not significantly correlated at the 95% confidence level, which implies that we should be cautious when interpreting the results as the same mechanism may not be responsible for both fluxes.

The direct estimates of the eddy heat flux do not include the fluxes produced by interleaving. The eddy heat fluxes are approximately 1×10^{-2} ° C m s^{-1}. This is of the same order of magnitude as the estimates of the fluxes produced by interleaving. In the Eastern Equatorial Pacific, Bryden and Brady report southward eddy heat fluxes O(1×10^{-1} ° C m s^{-1}) while in the Central Equatorial Pacific the magnitude and pattern of the eddy heat fluxes is similar to those reported here. It then becomes a question of determining the mechanism which produces the eddy fluxes and addressing the more difficult issue of whether models will represent the mechanism and the fluxes correctly. In the Central and Eastern Equatorial Pacific it is believed that barotropic instability and tropical instability waves with a period O(20 days) are largely responsible for the observed eddy heat and momentum fluxes (Brady 1990). The analysis of Gouriou and Toole (1993) showed that the mean circulation of the Western Equatorial Pacific does not satisfy the necessary conditions for barotropic instability (that the absolute vorticity ($\beta_{eq} - u_{yy}$) changes sign). In addition, there is no observational evidence to support tropical instability waves penetrating as far westward as the warm pool. Eddy resolving numerical models show some evidence for tropical instability waves penetrating west of the dateline but the role of instability waves in the Western Pacific remains largely undetermined. A plausible explanation may be that the observed fluxes at 150 m are due to meanders of the EUC which fluxes westward momentum and warmer water northward or westward momentum and warmer water southward, while those at shallower depths may be due to changes in the atmospheric forcing. This would seem to be consistent with the longer integral timescales. If this is the case then a model with realistic forcing and sufficient grid resolution should represent these processes. To explicitly resolve double-diffusive interleaving, high grid resolution

is required in both the vertical (several metres) and horizontal (O(10 km)) directions. At current grid resolution limits it is not possible to explicitly resolve double-diffusive interleaving in large-scale models and a parameterization scheme is required to represent the fluxes produced by interleaving.

3.3 Parameterization of the fluxes due to interleaving

Finite amplitude model for double-diffusive interleaving

When double-diffusive interleaving first takes place, the layers are driven by either the finger or the diffusive fluxes across one of the interfaces. Here, we assume that after several e-folding times (approximately 20-30 days), a steady state will exist in which the fluxes across the other double-diffusive interface become important; the vertical fluxes of heat and salt due to the double-diffusive interfaces now balance the advective fluxes. McDougall (1985b) has discussed the evolution of intrusive features to such a steady state and Walsh and Ruddick (1996) have examined the steady state in a one dimensional model. Figure 3.3 illustrates the evolution of the initial instability to the steady-state; as the initial instability develops, driven in this example by the diffusive interface, the opposite interface then tends to be in the finger sense. Eventually, we can envisage that a steady state will exist.

The main assumption of the finite amplitude model is that the vertical wavelength of the intrusions and the slopes of the intrusions across isopycnals are the same as those given by the linear stability analysis. The fastest growing instability has a vertical wavenumber given in chapter 2 (McDougall 1985a). For finger fluxes we assume that the slopes of the intrusions across isopycnals in θ-S space are those given by McDougall (1985a), namely:

$$\frac{\alpha\theta_l}{\beta S_l}\,|_{finger} = 1 - (1-\gamma_f)[1+(1+\epsilon_z)^{\frac{1}{2}}]^{-2} \tag{3.2}$$

This can be extended to diffusive fluxes, in the manner of Walsh and Ruddick (1995), to give:

$$\frac{\alpha\theta_l}{\beta S_l}\,|_{diffusive} = [1-(1-\gamma_d)[1+(1+\epsilon_z)^{\frac{1}{2}}]^{-2}]^{-1} \tag{3.3}$$

where ϵ_z is the non-dimensional vertical salinity gradient, γ_f is the finger flux ratio, γ_d is the diffusive flux ratio and derivatives denoted with the subscript l represent the advective

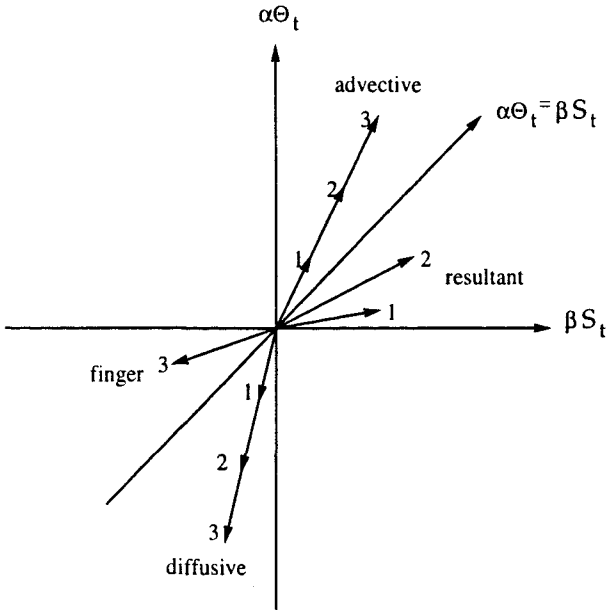

Figure 3.3: Evolution of the double-diffusive intrusion to the steady-state. Initially the diffusive fluxes and the advective fluxes produce a resultant change in the $\theta - S$ structure (arrows 1 and 2). When the finger fluxes begin to play a role the resultant change in the $\theta - S$ is reduced to zero (arrow 3).

parts of the Lagrangian derivatives. Taking ϵ_z to be equal to 0.5 (McDougall 1985a), the model predicts slopes of 0.9 and 1.2 for the finger and diffusive cases respectively.

The slopes which would be predicted from the simple advective-diffusive balance (the limits described in the previous chapter) are much larger than those which we observe in the Equatorial Pacific. However, the observed slopes in the Western Equatorial Pacific appear to be closer to 1.8 (analogous to features dominated by the diffusive interface) than the value of 1.2 predicted by theory. In Ruddick's (1992) analysis of intrusions in a Meddy which was observed for two years, the slopes of the intrusions were found to be very close to those given by the linear stability analysis. Although observations and theory are not in perfect agreement in the Western Equatorial Pacific, for consistency in developing this parameterization we will use the values predicted by the linear stability analysis.

In the steady-state the conservation equations are given by:

$$V\overline{S_y} + W\overline{S_z} = -BmS \tag{3.4}$$

$$V\overline{\theta_y} + W\overline{\theta_z} = -\frac{\beta}{\alpha}B\gamma_s mS \tag{3.5}$$

where γ_s is the flux ratio for the steady state and is equivalent to the slopes given by

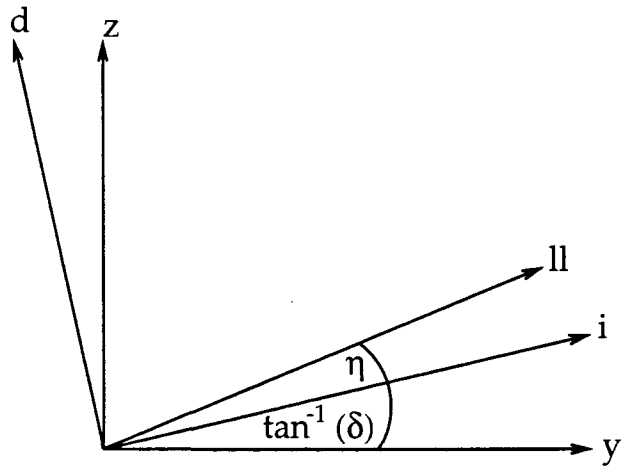

Figure 3.4: Sketch of the geometry of the system; the geodesic coordinates are given by y and z, isopycnal coordinates by i and d and the direction of the layers by $\|$. The layers slope at an angle η to isopycnals and isopycnals at an angle $\arctan(\delta)$ to the geodesic coordinates.

equations 3.2 and 3.3. When the Laplacian formulation for the fluxes across the interface is used rather than the McDougall formulation, $Bm \rightarrow K_s m^2$ and when diffusive fluxes dominate, S and θ change roles. In the steady-state, both finger and diffusive interfaces are important and the values of B and K_s are increased (McDougall 1985b).

From these two equations, we can now derive an expression for W in terms of V:

$$W = V \frac{\overline{S_y}}{\overline{S_z}} \frac{(1-\gamma_s)}{(\gamma_s - R_\rho)}. \tag{3.6}$$

This equation can be used to verify that W is positive/negative for γ_s less than/greater than one, which is in agreement with the finger/diffusive regime.

Functional form of the fluxes

In order to derive the functional form of the fluxes, we extend the advective-diffusive model of Joyce (1977). We first consider the various scales of motion (Joyce 1977); salt-fingers, diffusive interfaces and turbulent patches are defined as small-scale, intrusions are defined as medium-scale and water mass variations (or averaged fields) are defined as large-scale. Then we wish to parameterize the medium-scale fluxes for the large-scale model.

We start with the conservation equations 3.4 and 3.5. Taking the salt equation first and assuming that salt fingers dominate, we have

$$V'_{\|} \nabla \overline{S_{\|}} = -BmS' \tag{3.7}$$

where the subscript || indicates the direction parallel to the layers and the overbar indicates the large-scale. The geometry we are considering is sketched in figure 3.4. The main assumption that we will make here is based on the hypothesis that the perturbation salinity S' can be related to the large-scale salinity gradient, such that:

$$S' \cong \Delta S \cong \nabla \overline{S_{\|}} \Delta Y$$

where ΔY is the extent of the frontal region. The model of Joyce (1977) does not make this assumption and therefore is unable to express the fluxes in terms of mean quantities since the fluxes still depend on the medium-scale variability. Then we can write an expression for the fluxes of tracers along layers as:

$$\overline{V'_{\|} S'} = -Bm \nabla \overline{S_{\|}} (\Delta Y)^2.$$

This can be split into the diapycnal and isopycnal fluxes by observing that the layers slope at an angle η to isopycnals, where η is given by McDougall (1985a) to be:

$$\eta = \arctan(|\frac{a}{m}|) = \arctan(\frac{\epsilon_y}{4})$$

where a is the wavenumber in the y direction. We define η to be positive for layers sloping downwards across isopycnals and negative for upwards sloping layers.
This gives:

$$\overline{V'S'} = -Bm \nabla \overline{S_{\|}} (\Delta Y)^2 \cos(\eta)$$
$$\overline{W'S'} = -Bm \nabla \overline{S_{\|}} (\Delta Y)^2 \sin(\eta).$$

Approximating $\nabla \overline{S_{\|}}$ by $\overline{S_i}$, and substituting for m and ΔY on the basis of the fastest growing solutions of Richards (1991) (using the equatorial trapping scale, ψ, as ΔY), one obtains the following results, to first order in η:

$$\overline{V'S'} \cong -\frac{ND}{2\sigma^{\frac{1}{2}}\beta_{eq}} \overline{S_i} \tag{3.8}$$

$$\overline{W'S'} \cong -\eta \frac{ND}{2\sigma^{\frac{1}{2}}\beta_{eq}} \overline{S_i} \tag{3.9}$$

$$A_{SH} \cong \frac{ND}{2\sigma^{\frac{1}{2}}\beta_{eq}} \tag{3.10}$$

$$A_{SV} \cong \eta \frac{ND}{2\sigma^{\frac{1}{2}}\beta_{eq}} \frac{\overline{S_i}}{\overline{S_d}} \tag{3.11}$$

when the McDougall parameterization is employed for the interface fluxes and:

$$\overline{V'S'} \cong -\left(\frac{N^3 K_v \epsilon_y}{16\beta_{eq}{}^2 \sigma_{pr}^{\frac{1}{2}}}\right)^{\frac{1}{2}} \overline{S_i} \tag{3.12}$$

$$\overline{W'S'} \cong -\eta\left(\frac{N^3 K_v \epsilon_y}{16\beta_{eq}{}^2 \sigma_{pr}^{\frac{1}{2}}}\right)^{\frac{1}{2}} \overline{S_i} \tag{3.13}$$

$$A_{SH} \cong \left(\frac{N^3 K_v \epsilon_y}{16\beta_{eq}{}^2 \sigma_{pr}^{\frac{1}{2}}}\right)^{\frac{1}{2}} \tag{3.14}$$

$$A_{SV} \cong \eta\left(\frac{N^3 K_v \epsilon_y}{16\beta_{eq}{}^2 \sigma_{pr}^{\frac{1}{2}}}\right)^{\frac{1}{2}} \frac{\overline{S_i}}{\overline{S_d}} \tag{3.15}$$

when the Laplacian parameterization for the interface fluxes is employed.

Assuming that the isopycnal angle, $\arctan(\delta)$, is zero (which allows us to replace $\overline{S_{i,d}}$ by $\overline{S_{y,z}}$) and letting

$$\overline{S_z} = \frac{N^2}{g\beta(R_\rho - 1)}$$

equation 3.15 becomes:

$$A_{SV} = \eta\left(\frac{K_v \epsilon_y}{16N\beta_{eq}{}^2 \sigma_{pr}^{\frac{1}{2}}}\right)^{\frac{1}{2}} \overline{S_y} g\beta(R_\rho - 1).$$

The parameterization schemes given by the Laplacian formulation suggest that mixing in all directions increases as the salinity gradient increases. This makes good physical sense since the thermohaline gradient is the source of potential energy for the exchange. The dependence on the buoyancy frequency, N, will be discussed in a following section.

Estimates of the fluxes

Taking equations 3.12– 3.15, assuming that the interfaces are diffusively dominated and substituting parameter values comparable to those observed in the Western Equatorial Pacific (N=0.02s^{-1}, K_v=3x10^{-5}m^{2}s^{-1}, γ_d=0.15, η=1x10^{-4}, S_y=2x10^{-6} psu m^{-1}, σ_{pr}=1 and R_ρ=2), we find:

$$\overline{V'S'} = 2 \times 10^{-3} psu\ m\ s^{-1}$$

$$\overline{W'S'} = 2 \times 10^{-7} psu\ m\ s^{-1}$$

$$A_{SH} = 1 \times 10^{3} m^2 s^{-1}$$

$$A_{SV} = 4 \times 10^{-6} m^2 s^{-1}.$$

The estimate of A_{SH} is similar to our previous estimate in section 3.2 and to some extent justifies our assumption that the perturbation salinity can be related to the large-scale lateral salinity gradient. The value of A_{SH} is such that we expect interleaving to make a significant contribution to horizontal mixing and therefore the large-scale dynamics (Maes et al. 1996). The vertical diffusion coefficient is smaller than the value usually assumed for the background vertical diffusion due to turbulence in large-scale models (10^{-5} m^2 s^{-1}).

Ratio of heat to salt fluxes

McDougall (1985a) gives the ratio of temperature to salinity perturbations as:

$$\frac{\alpha\theta}{\beta S} \mid_{finger} = 1 + \frac{1}{2} B(1 - \gamma_s) \tag{3.16}$$

for finger driven intrusions, which can be extended to the case of diffusive driven intrusions to yield the result:

$$\frac{\alpha\theta}{\beta S} \mid_{diffusive} = (1 + \frac{1}{2} B(1 - \gamma_s))^{-1}. \tag{3.17}$$

This implies that the cross-frontal heat fluxes are greater than the cross-frontal salinity fluxes for finger driven layers and the relationship is reversed for diffusive layers. This is due to the shortcut mechanism (Toole and Georgi 1981). When fingering is responsible for the intrusions, the vertical salinity fluxes across the interface drive the intrusion, but the flux of salt along the layers is reduced. When the diffusive interface dominates this applies to the heat fluxes. We are not concerned here with the exact ratio but substituting appropriate values suggests a ratio of $0.65 < A_\theta : A_S < 1.2$.

Lateral diffusion coefficient

Another way of viewing the proposed functional form for the lateral transfer coefficient is to suppose that:

$$A_{SH} \sim l^2 \lambda$$

where λ is the growth rate (or the inverse of the relevant characteristic timescale) and l is the characteristic length scale. If we assume that the characteristic length scale is ψ, the trapping scale, and λ is the growth rate given by Richards (1991), we obtain:

$$A_{SH} \sim (\frac{N^3 K_v \epsilon_y}{\beta_{eq}^2})^{\frac{1}{2}}$$

the same functional form as given by equation 3.12. One might argue that there are two other possible choices for the characteristic length scale; the Equatorial radius of deformation, L_ϵ, and the inverse of the wavenumber of the intrusion in the cross-front direction, a. Taking these choices for the length scale would lead to the following forms for the transfer coefficient:

$$A_{SH} \sim \frac{N^2 d \epsilon_y}{\beta_{eq}}$$

with $l = L_\epsilon$, where d is the vertical scale, and

$$A_{SH} \sim \frac{K_V}{\epsilon_y^2}$$

with $l = a^{-1}$. Taking into account that ϵ_y is proportional to the salinity gradient and the inverse of the buoyancy frequency N squared, we see that these choices for the characteristic length scale leads to a different functional form for the transfer coefficient. In particular, the latter predicts a coefficient proportional to the buoyancy frequency but inversely proportional to the salinity gradient, while the former is identical to the previous expressions if d is taken to be m^{-1}. The latter expression appears to be counterintuitive since it is the thermohaline gradient which is the source of potential energy for the intrusions and we shall therefore assume that our initial choice for l, ψ, is the preferred one.

Vertical diffusion coefficient

The vertical (diapycnal) fluxes of heat and salt produced by intrusions are dependent on the angle η, requiring layers to slope across isopycnals. Crucially, the difference between the diffusive and the finger driven layers is not in the difference in the factors of the isopycnal fluxes of heat and salt but in the direction of the vertical fluxes associated with the layers. With salinity unstably stratified and temperature stably stratified, finger and diffusive layers will drive downgradient fluxes of heat, salt and upgradient fluxes of buoyancy. This would imply that the large-scale potential vorticity (via the stratification) increases,

as suggested by Cherubin et al. (1996). With both components stably stratified, the fluxes of salt will be in the opposite direction and, since the effects on salinity and temperature are opposing, the resulting effect on the buoyancy (and the potential vorticity) is unclear. It may be possible to observe the change in the potential vorticity in the downstream direction of the Equatorial Undercurrent which would be characterised by an increase in the stratification below the salinity maximum. In practice, quantifying the changes in the stratification due to advection and those due to double-diffusive interleaving would be a difficult task.

McDougall (1985b) and Garrett (1982) both suggested functional forms for the vertical diffusion coefficient based on interleaving models. The approach of Garrett was to parameterize the vertical diffusion coefficient in terms of a vertical scale and a timescale. The vertical scale was chosen to be that given by Ruddick and Turner (1979) for rundown intrusions and the timescale was estimated assuming that the intrusions developed at the edges of mesoscale eddies. The approach of McDougall is similar; an expression for the local vertical diffusion coefficient is derived and a basin-averaged diffusion coefficient is estimated assuming the ocean is packed with mesoscale eddies. While the approaches are different to that presented here, it is interesting to note that by making the hypothesis that the perturbation fields are related to the large-scale frontal fields our results give a similar dependence for the vertical diffusion coefficient. Our results predict that the vertical diffusion coefficient is proportional to the salinity gradient and inversely proportional to the buoyancy frequency. McDougall (1985b) suggests that the advective fluxes dominate over the interface fluxes. This supports the assumption that the advective component is the main contribution to the vertical fluxes. This agreement should be interpreted somewhat cautiously since their results were intended to represent a basin wide average, while these results are applicable only to the frontal region.

The role of the buoyancy frequency

After analysing CTD data from the Caribbean, which suggested that in depth ranges with high vertical stability the horizontal distribution of salinity was far more homogenised than the depth ranges with low stability, Parr (1936) suggested that lateral (or isopycnal) mixing increased as the buoyancy frequency increased. Harvey (1995) hypothesised that the action of mesoscale eddies could also produce a similar dependence of the lateral diffusion

coefficient on the buoyancy frequency. It is worth noting that the functional dependence suggested here is also similar to that suggested by Gargett (1984)for the deep ocean. Gargett suggested that the vertical diffusion coefficient should be inversely proportional to the buoyancy frequency. It is interesting that the buoyancy frequency appears to play a similar role in determining the functional form of the diffusion coefficients even though the processes are different.

Kuz'mina (1990) suggests that double-diffusive interleaving will only dominate over baroclinic instability when the isopycnal slope, δ, is of the same order of magnitude as the non-dimensional salinity gradient, ϵ_y. Using the values calculated for the Equatorial Pacific, this suggests an upper limit on valid slopes of $O(10^{-3})$. It is unclear whether the formulations proposed by the authors mentioned above are only valid for small isopycnal slopes (i.e. $\delta \ll 1$). If this condition is not enforced then mixing would primarily take place along horizontal surfaces (in the geodesic sense), with diapycnal mixing dominating at small N and large isopycnal slope and isopycnal mixing dominating at large N and small isopycnal slope. Such a scenario may be representative for some parts of the ocean (e.g. convective chimneys where the slope is large and fluid may be exchanged laterally with the resting ocean).

3.4 Discussion

We have used the method of Joyce (1977) to infer the fluxes of heat and salt produced by interleaving. The lateral fluxes of heat (and salt) are estimated to be approximately 2-6 x 10^{-3} ^{o} C (psu) m s^{-1}. The inferred horizontal diffusion coefficient is approximately 1 x 10^{3} m^{2} s^{-1}. This is the same order of magnitude as the horizontal diffusion coefficients currently employed in models which are used to simulate the Equatorial ocean (Stockdale et al. 1993). Maes et al. (1996) found that at $O(10^{3}$ m^{2} $s^{-1})$ both the vertical and lateral diffusion coefficients played a role in the dynamical and thermodynamical balances of the Equatorial Pacific. Reducing the value by one order of magnitude leads to vertical mixing dominating, while increasing the value by one order of magnitude lead to lateral mixing dominating and a somewhat unrealistic Equatorial boundary layer forming. This interaction between vertical and lateral mixing suggests that their model produced as much mixing as was required to keep it in balance. It is therefore important that the relative contributions of lateral and vertical mixing are accurately estimated. Extending

the model of Joyce we have developed a parameterization scheme for the fluxes produced by interleaving for a large-scale numerical model. The parameterization predicts the functional form of the lateral diffusion coefficient, A_H:

$$A_H \sim (N S_y)^{\frac{1}{2}}$$

where N is the buoyancy frequency and S_y is the lateral salinity gradient. The inferred vertical diffusion coefficient is approximately $10^{-5}\ m^2\ s^{-1}$. This is also similar in magnitude to the values typically used in large-scale models. Horizontal mixing is usually thought of as being produced by mesoscale eddies and vertical mixing as being produced by turbulence. Interleaving produces both lateral and vertical mixing. In the next chapter we will discuss the implementation of the proposed scheme and its interaction with the existing vertical mixing schemes.

In an attempt to address the importance of these fluxes in comparison with the fluxes produced by other processes, we have calculated the eddy heat and momentum fluxes directly from mooring data in the Western Equatorial Pacific. The eddy heat fluxes were northward and the same order of magnitude as the estimates of the fluxes produced by interleaving and were associated with a negative momentum flux. We have suggested that the observations may be the result of meanders in the EUC or reversals in the currents due to atmospheric forcing but it is impossible to show this from the present dataset. High resolution moorings extending several degrees away from the Equator or a detailed study of the processes in a three-dimensional numerical model are necessary to quantify the importance of these processes. With sufficient grid resolution we suggest that the eddy fluxes may be explicitly represented in a large-scale numerical model.

An interesting issue regards the grid resolution when the parameterization applies. Double-diffusive interleaving can only be represented explicitly when the vertical resolution is high enough to parameterize the double-diffusive interface. At realistic grid resolutions for large-scale models the parameterization scheme will always be required to model the fluxes of heat and salt produced by interleaving. Presumably, the possibility of mesoscale eddies appearing in the thermocline of a model (regardless of the grid resolution) will be reduced by the lateral diffusion coefficient (which may be regarded as high for some grids). The upper and deep ocean should be fairly insensitive to the mixing in the thermocline and eddies should be able to form when appropriate.

We have not addressed the parameterization of the momentum fluxes. It is not clear

that the interleaving process is efficient in redistributing momentum (in fact the estimates of the meridional velocity associated with the interleaving probably suggests that it has little importance for the momentum). Further theoretical work or numerical experiments might help establish this. If this is to be attempted it is probably useful to recast the interleaving process in terms of its effects on the potential vorticity.

Above we have argued that models should represent the fluxes produced by processes which are not resolved by the model. If the fluxes estimated from the mooring are the result of resolved processes, interleaving and its associated fluxes should be important in the Western Equatorial Pacific. In the Eastern and Central Equatorial Pacific, tropical instability waves and barotropic instability are believed to be important in transferring heat and momentum. The next step in parameterization of lateral fluxes for a coarse resolution Equatorial model is to include a scheme which represents the fluxes produced by barotropic instability. The scheme proposed for interleaving may be useful for the entire extent of the Pacific basin given the similarity of the features which Toole (1981a) observed in the Eastern Equatorial Pacific and McPhaden (1985) observed in the Central Equatorial Pacific to those observed in the Western Equatorial Pacific.

Chapter 4

The influence of mixing on the large-scale structure of the Equatorial Ocean

4.1 Introduction

In the previous chapters we have determined that double-diffusive interleaving is one of the mechanisms responsible for many of the intrusive features observed in the Western Equatorial Pacific and we have developed a parameterization for the heat and salt fluxes produced by double-diffusive interleaving. Here we attempt to address the importance of sub-grid scale fluxes of heat, salt and momentum to the large-scale structure of the Equatorial ocean. In particular, how do they influence the dynamical and tracer fields and determine the large-scale balances of heat, salt and momentum?

Yin and Sarachik (1993) forced a two-dimensional model (in the vertical-meridional plane) with a zonal wind and were able to address some questions regarding the balance of a steady Equatorial Undercurrent; their experiments examined the effect of the zonal pressure gradient, the linear/nonlinear dynamic balance, the role of horizontal momentum diffusion and the heat balance. The model which we will use in this work is similar to that employed by Yin and Sarachik (1993), in that we prescribe a zonal pressure gradient, but the numerical approach is different.

Schneider and Muller (1994) also used a two-dimensional model, on shorter timescales, to examine the sensitivity of the Yoshida jet and upwelling in response to an easterly wind under different parameterizations of the vertical diffusion. They found that the parameterization schemes of vertical mixing were crucial to the dynamic balances. For one of the three parameterizations the upwelling was reversed.

Other numerical studies have focussed on three-dimensional models. Particularly relevant here are the experiments of Maes et al (1996), who examined the sensitivity of a General Circulation Model to the value of the (constant) lateral diffusion coefficient. They found that a non-linear interplay exists between lateral and vertical mixing; the vertical mixing scheme of Blanke and Delecluse (1993) switches on when the dissipation provided by the lateral mixing is not sufficient. The dynamical balances of the EUC in the model of Wacongne (1988) can be altered depending on the value of the lateral diffusion coefficient — lateral mixing can dominate the balances or play no role whatsoever.

The work of Maes et al. (1996) and Yin and Sarachik (1993) has confirmed the sensitivity of the structure and dynamics of the Equatorial ocean to lateral mixing. However we can identify outstanding questions regarding the role of sub-grid scale fluxes which have not been answered. Is momentum or tracer diffusion controlling the dynamics in numerical models? What role does the salinity play? How important is the heat-salt flux ratio (Gargett and Holloway 1992) in the Equatorial ocean? How important is the orientation of the mixing surfaces? In this chapter we will address these issues as a means of understanding the dynamics before we implement the parameterization scheme which has been proposed in the previous chapter for mixing due to double-diffusive intrusions.

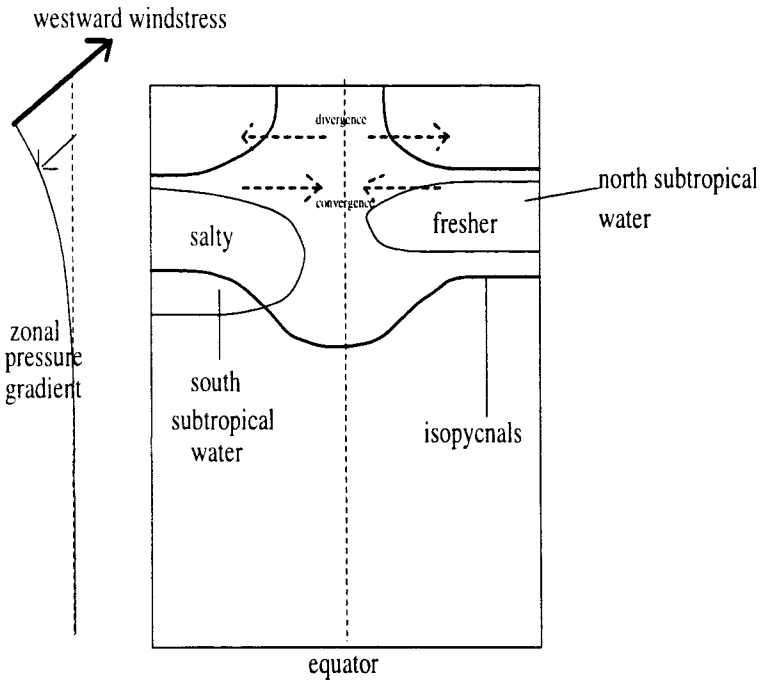

Figure 4.1: Schematic of the model experiments; the circulation is driven by an easterly wind at the surface balanced by a prescribed eastward pressure gradient.

We approach this work by comparing the quasi-steady state of a two-dimensional model in response to constant easterly winds, as shown schematically in figure 4.1. While the steady-state equilibrium is important in simulations of the Equatorial Ocean, it is also useful to consider the transients in the system. We do this here by examining the response of the ocean to a reversal in the zonal wind field (comparable to a Westerly Wind Burst (WWB)).

4.2 Numerical experiments

The numerical model we consider is a two-dimensional model (in the vertical-meridional plane) on an equatorial beta plane. Derivatives in the zonal direction are taken to be zero, except for the zonal pressure gradient and the zonal density gradient, which are prescribed. The pressure, p, and density, ρ, are given by:

$$p(x,y,z,t) = \overline{p}(x,z) + p'(y,z,t)$$
$$\rho(x,y,z,t) = \overline{\rho}(x,z) + \rho'(y,z,t)$$

where the overbar denotes the prescribed part of the pressure and density. Since the zonal gradients of density and pressure are prescribed, the prescribed part of the pressure and density can be written:

$$\overline{p}(x,z) = xf(z)$$
$$\overline{\rho}(x,z) = xg(z)$$

where f, g are functions describing the vertical structure of the zonal pressure gradient and zonal density gradient respectively .

The model equations are given by:

$$\frac{\partial u}{\partial t} + v\frac{\partial u}{\partial y} + w\frac{\partial u}{\partial z} - \beta_{eq} yv = -\frac{\partial P}{\partial x} + \frac{\partial}{\partial z}K_v\frac{\partial u}{\partial z} + \frac{\partial}{\partial y}K_h\frac{\partial u}{\partial y} \tag{4.1}$$
$$\frac{\partial v}{\partial t} + v\frac{\partial v}{\partial y} + w\frac{\partial v}{\partial z} + \beta_{eq} yu = -\frac{\partial P}{\partial y} + \frac{\partial}{\partial z}K_v\frac{\partial v}{\partial z} + \frac{\partial}{\partial y}K_h\frac{\partial v}{\partial y} \tag{4.2}$$
$$\frac{\partial v}{\partial y} + \frac{\partial w}{\partial z} = 0 \tag{4.3}$$

$$\frac{\partial\theta}{\partial t} + u\frac{\partial\theta}{\partial x} + v\frac{\partial\theta}{\partial y} + w\frac{\partial\theta}{\partial z} = \frac{\partial}{\partial z}A_{v\theta}\frac{\partial\theta}{\partial z} + \frac{\partial}{\partial y}A_h\frac{\partial\theta}{\partial y} \tag{4.4}$$

$$\frac{\partial S}{\partial t} + u\frac{\partial S}{\partial x} + v\frac{\partial S}{\partial y} + w\frac{\partial S}{\partial z} = \frac{\partial}{\partial z}A_{vS}\frac{\partial S}{\partial z} + \frac{\partial}{\partial y}A_h\frac{\partial S}{\partial y} \tag{4.5}$$

$$\frac{\partial P}{\partial z} = -\frac{g}{\rho_o}\rho \tag{4.6}$$

$$\rho = f(\theta, S) \tag{4.7}$$

where u, v and w denote the zonal, meridional and vertical velocities respectively, θ, S and ρ denote temperature, salinity and density and P is the hydrostatic pressure ,p, divided by the reference density, ρ_o. The density is calculated from temperature and salinity via the non-linear equation of state as prescribed by Friedrich and Levitus (1972). Prescribing $\frac{\partial P}{\partial x}$ also implies prescribing $\frac{\partial \rho}{\partial x}$ (the zonal density gradient) through the hydrostatic relation, although how the density gradient should be divided between temperature and salinity is not determined. We will return to this question in the next section.

Prescribing the pressure and density in this manner can be shown to be inconsistent. With the density separated into its prescribed and perturbation parts, the density equation becomes:

$$\frac{\partial\rho'}{\partial t} + uf(z) + v\frac{\partial\rho'}{\partial y} + wx\frac{\partial f}{\partial z} + w\frac{\partial\rho'}{\partial z} = x\frac{\partial}{\partial z}A_{v\rho}\frac{\partial f}{\partial z} + \frac{\partial}{\partial z}A_{v\rho}\frac{\partial\rho'}{\partial z} + \frac{\partial}{\partial y}A_h\frac{\partial\rho'}{\partial y}.$$

This equation shows that ρ' cannot be considered to be independent of x for f_z which is non-zero. However, for the function, $f(z)$ which is employed here, the vertical advection and vertical diffusion term (wxf_z, $x(A_{v\rho}f_z)_z$) are small for x less than 40 degrees longitude. We therefore consider the model to be valid only for small x.

The boundary conditions at the surface, z=0, are given by:

$$w = 0 \tag{4.8}$$

$$K_v\frac{\partial u}{\partial z} = \tau_x \tag{4.9}$$

$$A_v\frac{\partial\theta}{\partial z} = \Gamma^{-1}dz(\theta - \theta_0) \tag{4.10}$$

$$A_v\frac{\partial S}{\partial z} = \Gamma^{-1}dz(S - S_0) \tag{4.11}$$

and at the bottom of the domain, z=H, are given by:

$$w = 0 \tag{4.12}$$

$$K_v \frac{\partial u}{\partial z} = 0 \tag{4.13}$$

$$A_v \frac{\partial \theta}{\partial z} = 0 \tag{4.14}$$

$$A_v \frac{\partial S}{\partial z} = 0 \tag{4.15}$$

where τ_x (=-0.5 x 10^{-4} m^2 s^{-1}) is the zonal wind forcing, which is chosen such that it balances the vertical integral of the zonal pressure gradient, i.e.

$$\tau_x = \int_0^H \frac{\partial P}{\partial x} dz, \tag{4.16}$$

and Γ is equivalent to a relaxation timescale (given here as 30 days (Yin and Sarachik 1993)) for the Haney type boundary conditions (Haney 1971) imposed on temperature and salinity. The relaxation values are given by θ_0 = 29°C and S_0 = 34 psu.

We assume that vertical mixing takes place due to turbulence and shear instability and a suitable parameterization is given by the Pacanowski and Philander (1981) scheme, based on the Richardson number criteria:

$$K_v = \frac{K_{v0}}{(1 + 5Ri)^2} + K_{vb} \tag{4.17}$$

$$A_v = \frac{K_v}{(1 + 5Ri)} + A_{vb} \tag{4.18}$$

where K_{v0} = 50 $cm^2 s^{-1}$, K_{vb} = 1 $cm^2 s^{-1}$ and A_{vb} = 0.1 $cm^2 s^{-1}$ and the Richardson number, $Ri = N^2/(U_z^2 + V_z^2)$.

The details of the numerical method are described in the appendix. We solve for the meridional velocity field and infer the vertical velocity through continuity. The alternative is to solve for the streamfunction, ϕ, defined by $v = \phi_y, w = -\phi_z$. This was the method employed by Yin and Sarachik (1993). The domain considered here is 20°S to 20°N and the surface down to 800 m. Outside $\pm$ 10 ^{o} the lateral momentum diffusion is increased from its interior value to 1 x 10^5 m^2 s^{-1} at the northern and southern boundaries (the results are fairly insensitive to the width of this viscous layer). The vertical resolution is given as 10 m, the horizontal resolution is 25 km and the timestep is 1000 s (we chose this resolution to be comparable with the highest vertical and meridional resolution currently employed in OGCMs but still not sufficient to resolve double-diffusive interleaving). If the resolution is halved and the timestep doubled the results are unchanged.

The numerical scheme used is a leapfrog scheme with a forward timestep every ten steps. Convection is parameterized by the Yin and Sarachik (1994) scheme. The numerical experiments performed are summarised in table 4.1. The control experiment is labelled A1; the momentum diffusion, K_h, is set at a value of 5000 m^2 s^{-1} and the tracer (heat and salt) diffusion is set at the same value and prescribed to be along geodesic surfaces. The experiments labelled B are designed to test the sensitivity of the model to the values of the diffusion coefficients of both momentum and tracers; broadly there are two sets of experiments with the momentum diffusion held constant and the tracer diffusion allowed to vary and a set of experiments with the tracer diffusion held constant and the momentum diffusion allowed to vary. The experiments labelled D are designed to test the sensitivity of the model to the ratio of vertical diffusion of heat and salt; the ratio is given and also the parameter which is held at the value prescribed by equation 4.18 (Pacanowski and Philander scheme). The experiments labelled E are designed to test the sensitivity of the model to the prescription of the transfer surfaces for tracer diffusion, in particular to compare geodesic coordinates with isopycnal coordinates. The experiments labelled F are designed to study the impact of the parameterization scheme for double-diffusive intrusions on the system. We have examined the impact of the transfer direction and the effect of a low Prandtl number. Finally, the experiments labelled G are designed to examine the impact of tracer and momentum mixing on the transients. For each experiment, table 4.1 lists not only the experimental details but also, for comparison, a number of diagnostics: the maximum speed of the EUC (u_{EUC}), the maximum value of the overturning streamfunction (ψ_{max}), the maximum value of the upwelling velocity (w_{max}), the Sea Surface Temperature on the Equator (SST_{eq}) and the Sea Surface Salinity on the Equator (SSS_{eq}).

4.3 Spin-up to the quasi-steady state

For all the experiments we initialise the model with the density profile shown in figure 4.2 [a]. The isopycnals are initially flat, i.e. the background velocity is zero and there is no available potential energy. The salinity and temperature fields are initialised to be close to the observed mean fields. The $\theta - S$ profiles are shown in [b]; the profiles north and south of the front are chosen to be typical of the observed structure in the Western Equatorial Pacific. The maxima associated with Subtropical Thermocline Water (STW) can be seen in the thermocline and the salinity minimum associated with Antarctic Intermediate water

EXPT NO	spin-up time	K_h $m^2 s^{-1}$	A_h $m^2 s^{-1}$	γ	iso?	BR?	intrusion slope	u_{EUC} $cm\ s^{-1}$	ψ'_{max} $m^2\ s^{-1}$	w_{max} $cm\ s^{-1}$	SST_{eq} ^oC	SSS_{eq} psu
A1	1 year	5000	5000	1	no	no	0.0	121	5.9	0.0046	24.1	34.7
B1	1 year	1000	10000	1	no	no	0.0	171	5.4	0.0054	25.3	34.6
B2	1 year	1000	5000	1	no	no	0.0	196	5.0	0.0047	24.7	34.7
B3	1 year	1000	2000	1	no	no	0.0	218	4.6	0.0037	24.1	34.8
B4	1 year	1000	500	1	no	no	0.0	222	4.0	0.0025	23.5	34.9
B5	1 year	1000	1000	1	no	no	0.0	222	4.3	0.0030	23.8	34.8
B6	1 year	10000	1000	1	no	no	0.0	115	4.4	0.0029	23.0	34.8
B7	1 year	5000	1000	1	no	no	0.0	144	4.4	0.0031	23.0	34.8
B8	1 year	2000	1000	1	no	no	0.0	187	4.3	0.0029	23.4	34.8
B9	1 year	2000	4000	1	no	no	0.0	167	5.1	0.0044	24.2	34.7
B10	1 year	3000	3000	1	no	no	0.0	155	5.2	0.0040	23.8	34.7
B11	1 year	4000	2000	1	no	no	0.0	148	4.9	0.0034	23.4	34.8
B12	1 year	4000	500	1	no	no	0.0	157	4.1	0.0031	22.8	34.8
B13	1 year	4000	8000	1	no	no	0.0	118	6.2	0.0052	24.6	34.7
D1	1 year	5000	5000	0.5 (a)	no	no	0.0	122	5.4	0.0044	24.3	34.7
D2	1 year	5000	5000	2.0 (a)	no	no	0.0	119	5.9	0.0047	23.8	34.7
D3	1 year	5000	5000	2.0 (b)	no	no	0.0	121	5.6	0.0045	24.2	34.7
D4	1 year	5000	5000	0.5 (b)	no	no	0.0	120	5.9	0.0047	24.0	34.7
E1	1 year	5000	5000	1	yes	no	0.0	136	6.1	0.0040	22.0	34.8
E2	1 year	5000	2000	1	yes	no	0.0	139	5.0	0.0033	21.4	34.8
F1	1 year	5000	5000	1	no	yes	0.0	130	5.8	0.0048	23.4	34.8
F2	1 year	5000	5000	1	yes	yes	0.0	140	5.0	0.0036	21.6	34.9
F3	1 year	5000	5000	0.5	yes	yes	1×10^{-4}	138	6.0	0.0039	21.3	34.8
F4	1 year	5000	5000	2.0	yes	yes	-1×10^{-4}	135	4.3	0.0037	21.7	34.9
F5	1 year	5000	5000	1	yes	yes	$\delta \rightarrow \frac{1}{2}\sigma$	136	5.6	0.0041	22.5	34.9
F6	1 year	1000	5000	1	no	yes	0.0	206	5.0	0.0042	24.1	34.8
G1	WWB	5000	5000	1	no	no	0.0	102	5.8	0.0044	25.1	34.6
G2	WWB	5000	1000	1	no	no	0.0	123	6.2	0.0055	24.4	34.5
G3	WWB	5000	5000	1	no	yes	0.0	111	5.8	0.0061	24.6	34.6

Table 4.1: Details of the numerical experiments performed and reported in this chapter. K_h, A_h refer to the horizontal momentum, tracer diffusion respectively, γ denotes the heat-salt flux ratio, iso refers to mixing along isopycnals (if the entry is *no* mixing takes place along geodesic surfaces, if *yes* then the mixing is referenced to isopycnal surfaces) BR refers to the parameterization for intrusions and the intrusion slope is only non-zero when the entries in the columns iso and BR are both yes. (a) denotes A_{vS} is held constant, (b) denotes $A_{v\theta}$ is held constant.

is identifiable lower in the water column. The extent of the frontal zone is specified to be 500 km. The model is forced with a constant easterly wind stress of 0.05 N m^{-2} which is balanced by the zonal pressure gradient shown in [c]. The zonal preesure gradient is chosen such that its form is similar to those derived from observations (Mangum et al. 1990). The corresponding zonal temperature gradient is shown in [d]. The minimum in the zonal temperature gradient at the depth of the thermocline reflects the large scale slope of the thermocline towards the surface in the Eastern Equatorial Pacific (Bryden and Brady 1985). We have made the approximation that the zonal salinity gradient is small enough to allow us to regard the zonal advection of salt in the EUC as negligible. This is primarily motivated by the asymmetry in the salinity field with a maximum south of the Equator and a minimum north of the Equator. If the zonal salinity gradient is large and positive or large and negative the structure of the salinity field is changed. Since the initial conditions are close to the steady-state fields, this suggests that the zonal salinity gradient may well be small in its contribution to the zonal density gradient when compared with the zonal temperature gradient. The initial zonal and meridional velocity fields are at rest.

Figure 4.3 shows the zonal velocity field ten days after the windstress is switched on. The initial response of the ocean is characterised by a westward Yoshida jet at the surface, with a magnitude of 40 cm s^{-1}, which is forced directly by the zonal wind stress. At later times, the density and velocity structure begin to respond to the eastward zonal pressure gradient forcing the EUC at the depth of the thermocline. Figure 4.4 shows the speed of the EUC and the mean density of the section as a function of time along with their time derivatives for experiment A1. The EUC speed accelerates initially and continues to accelerate as it approaches the steady state. After one year the EUC is continuing to accelerate. At the end of the run the drift is equivalent to 30 cm s^{-1} per year, although there is indication that this drift is slowly decreasing. It is also worth noting that the drift is several orders of magnitude smaller than the terms which provide the major contributions to the momentum balance. The mean density of the section is persistently decreasing. This is due to the surface buoyancy flux which always acts to make the ocean warmer and fresher (i.e. less dense). The buoyancy flux is prescribed via the Haney relaxation term and therefore as the ocean surface becomes colder and saltier due to upwelling, the surface buoyancy flux increases, as the time derivative of the mean density shows. The ocean has not reached total equilibrium but we consider the resulting fields as representing a quasi steady-state. Extending the integration shows that on a diffusive timescale (several years)

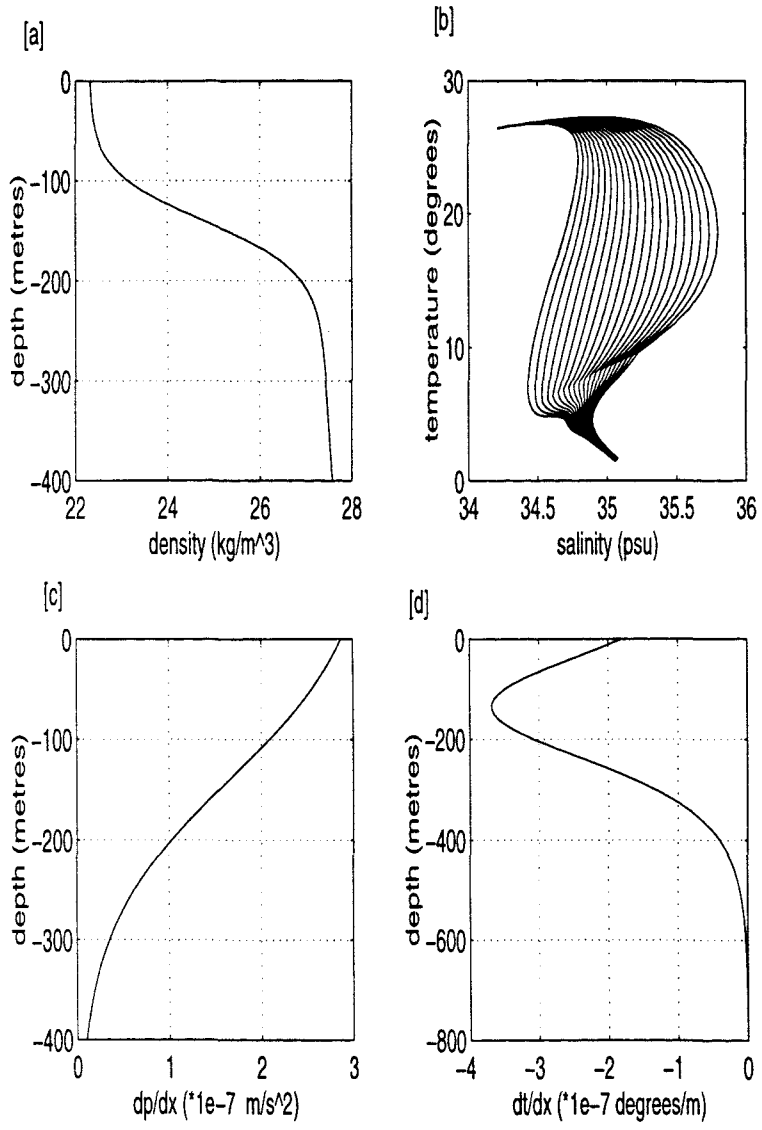

Figure 4.2: Initial conditions for experiments. [a] shows the vertical density profile, [b] shows the $\theta - S$ profiles, [c] shows the vertical structure of the zonal pressure gradient and [d] shows the zonal temperature gradient.

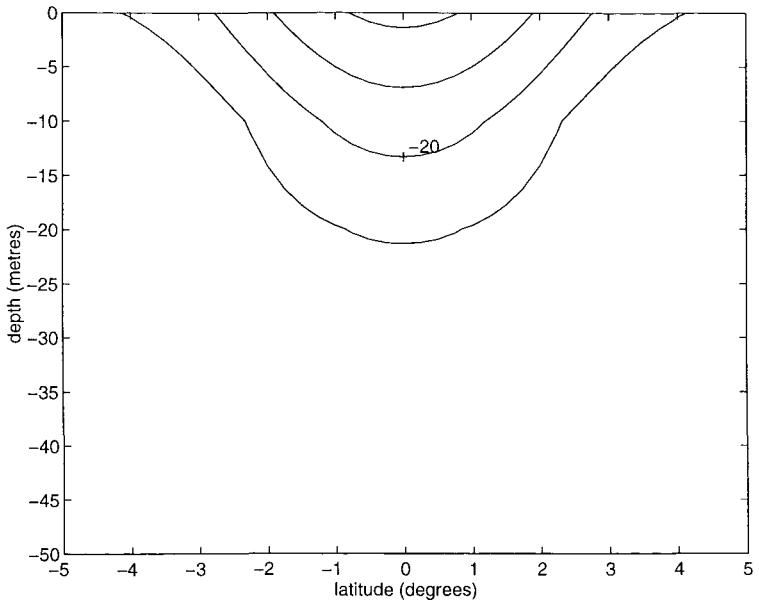

Figure 4.3: Zonal velocity field ten days after the start of the integration. At the surface the Yoshida jet is westward.

the density gradients are reduced and the EUC begins to spin down.

Figure 4.5 [a] shows the zonal velocity fields one year after the start of integration for experiment A1. The westward jet is reminiscent of the Yoshida jet but the presence of the Equatorial Undercurrent, which is centred at approximately 150 metres with a speed of 121 cm s^{-1}, penetrates into the westward jet at the surface. The solutions of Philander and Pacanowski (1980) showed that the structure of surface jets is dependent on whether the balance is linear or non-linear. With non-linear advective terms included, westward jets are shallower, while eastward jets are deeper. The effect of non-linear terms has also been shown by Yin and Sarachik (1993); when the balance was linear, the surface jet was reduced in depth near the Equator and the EUC had a more symmetric structure. Figure 4.5 [b] shows the streamfunction associated with the circulation with a maximum of 5.9 m^2s^{-1}. The temperature field [c] and salinity field [d] show clearly the effect of the upwelling on the tracer fields and the bulge in the thermocline associated with the EUC is also apparent.

Figure 4.6 shows the heat and salt budgets on the Equator and momentum budgets at 0.25^{o}N. In the upper 50 metres the balance in the heat budget (figure 4.6 [a]) is between vertical and meridional diffusion and vertical advection while the zonal momentum balance (figure 4.6 [c]) is between vertical diffusion, the zonal pressure gradient and vertical advection. At the depth of the EUC (approximately 150 metres), the heat balance can be

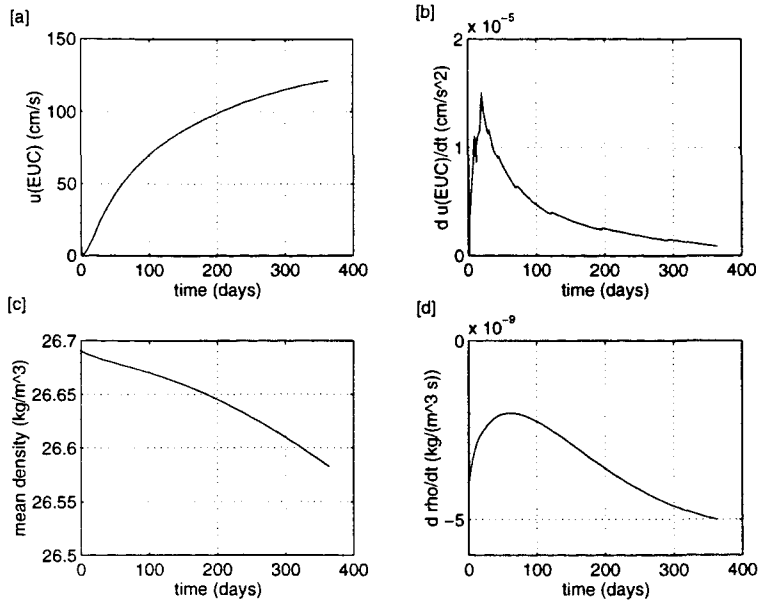

Figure 4.4: [a] shows the EUC speed as a function of time, [b] shows the rate of change of the EUC speed as a function of time, [c] shows the mean density of the ocean as a function of time and [d] shows the rate of change of the mean density as a function of time.

seen to be primarily between the vertical and zonal advection and the lateral diffusion, while the zonal momentum balance is between the zonal pressure gradient and lateral diffusion. The meridional momentum balance [d] is between the Coriolis term and the meridional pressure gradient, i.e. the circulation is in geostrophic balance. The salt budget [b] is qualitatively different from the heat budget with meridional advection, meridional diffusion and vertical advection making the major contributions to the balance.

4.4 Sensitivity to the magnitude of lateral mixing

In the previous section we looked at the steady state for one set of values for the lateral diffusion coefficients of momentum and tracers (heat and salt), with the Prandtl number, $\sigma_{pr} = K_h/A_h$, equal to one. Parameterization of the diffusion coefficients for both momentum and tracers may lead to situations when the Prandtl number is not identical to unity. One might envisage processes that may be more efficient at mixing tracers than momentum and vice versa, i.e. the implied diffusion coefficients for tracers and momentum may not be well correlated and the Prandtl number may vary. To understand how we might expect parameterizations to influence the circulation we will first explore the dynamics of the EUC in the parameter space of the lateral diffusion coefficients (experiments B).

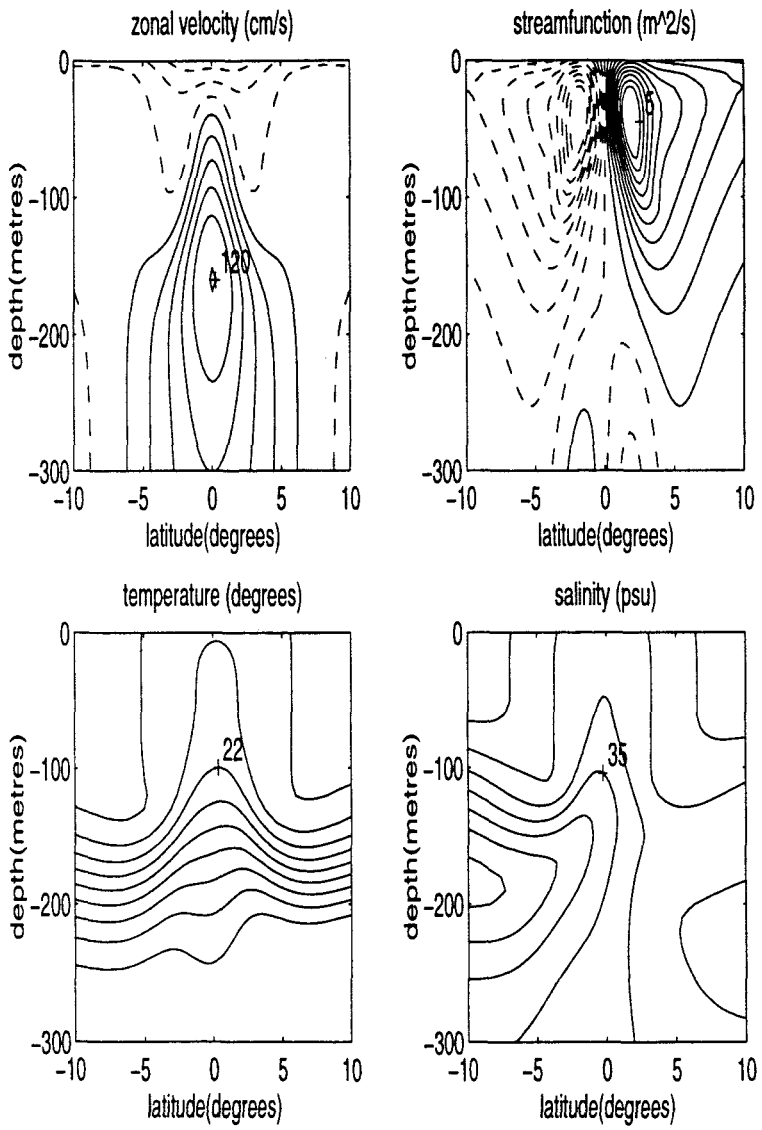

Figure 4.5: Experiment A1 [a] shows the zonal velocity field (the contour interval is 20 cm s^{-1} and dashed lines represent negative (westward) values), [b] shows the streamfunction (contour interval is 0.5 m^2 s^{-1}), [c] shows the temperature field (contour interval is 2 degrees), [d] shows the salinity field (contour interval is 0.2 psu).

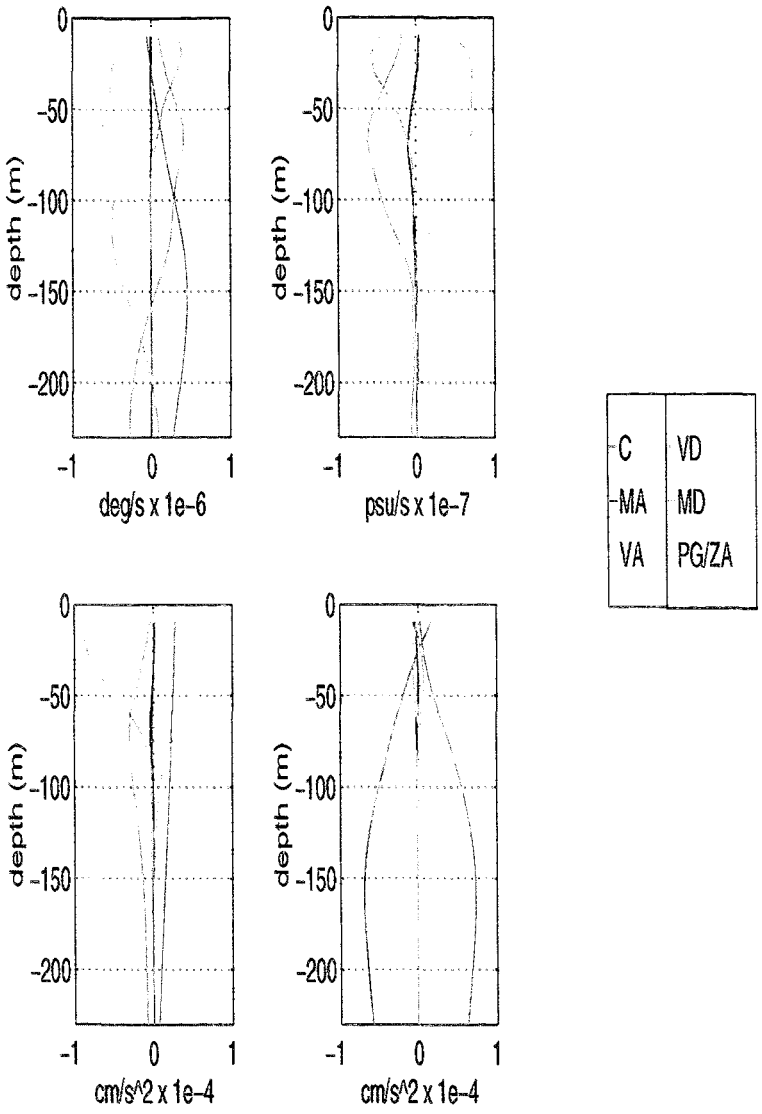

Figure 4.6: Experiment A1. [a] shows the heat budget (units are 1×10^{-6} ° C s^{-1}), [b] shows the salinity budget (units are 1×10^{-7} psu s^{-1}) on the Equator. [c] shows the zonal momentum budget (units are 1×10^{-6} m s^{-2}), [d] shows the meridional momentum budget (units are 1×10^{-6} m s^{-2}) at 0.25°N. The key is shown; VD represents vertical diffusion, MD meridional diffusion, PG pressure gradient, ZA zonal advection, C Coriolis, MA meridional advection, VA vertical advection.

In experiment B5 we have reduced the lateral diffusion of tracers and momentum by a factor of five. Figure 4.7 shows the zonal velocity, streamfunction, temperature and salinity for this experiment one year into the integration. The speed of the EUC has increased by almost a factor of two to 222 cm s^{-1} (the westward Yoshida jet is no longer present at the surface on the Equator and the surface velocity field is eastward), the overturning streamfunction has decreased to 4.3 m^2 s^{-1} and the SST has decreased from 24.1 °C to 23.8°C. Are the observed changes in the circulation due to the reduction in the lateral diffusion coefficient for tracers or the reduction in the lateral diffusion coefficient for momentum? In this section we will attempt to highlight the different roles that the two lateral diffusion coefficients play.

The control experiment described earlier (A1) suggested that there were two controls on the speed of the EUC; one exerted by the lateral diffusion of momentum and the other by the lateral diffusion of heat (we will use heat as our tracer in this section). Mathematically, we might express these balances in the following way:

$$\frac{\partial P}{\partial x} \simeq \frac{\partial}{\partial y} K_h \frac{\partial u}{\partial y} \tag{4.19}$$

$$u\frac{\partial \theta}{\partial x} + w\frac{\partial \theta}{\partial z} \simeq \frac{\partial}{\partial y} A_h \frac{\partial \theta}{\partial y}. \tag{4.20}$$

The first equation differs from the one discussed by Yin and Sarachik (1993); they asserted that at the depth of the EUC the zonal momentum balance was between the vertical advection and the meridional diffusion (although the zonal momentum budget they plotted is almost identical in character to the one shown in figure 4.6). Rewriting these balances as expressions for the EUC speed, we obtain:

$$u_{EUC} \sim \frac{P_x}{K_h} y'^2 \tag{4.21}$$

$$u_{EUC} \sim \frac{-A_h \theta_{yy} + w\theta_z}{-\theta_x} \tag{4.22}$$

where y' is a characteristic length scale. These relationships suggest that the EUC speed will be inversely proportional to K_h and decrease linearly as A_h increases. However, since w and θ_z are not necessarily invariant under changes of the diffusion coefficients, these equations can only be taken as an indication of the dependence on the parameters. Figure 4.8 [a] shows the EUC speed plotted against $1/K_h$ for experiments B5-8, where A_h

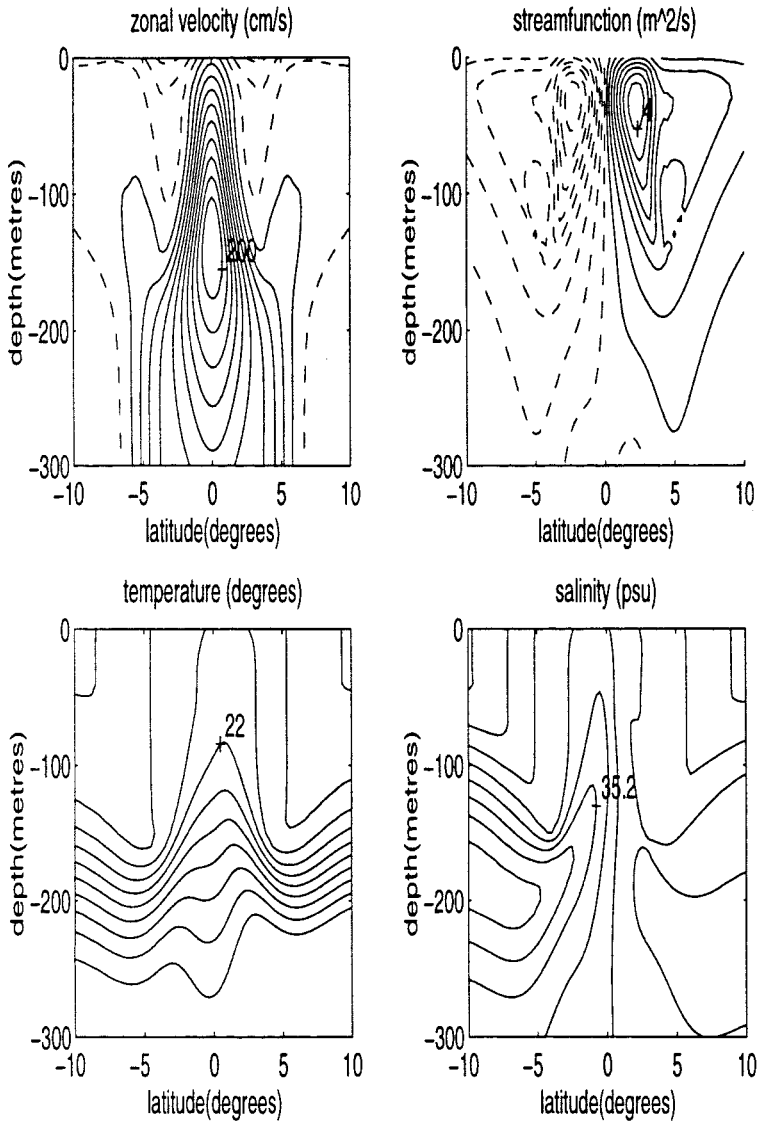

Figure 4.7: Experiment B5. [a] shows the zonal velocity field (the contour interval is 20 cm s^{-1} and dashed lines represent negative (westward) values), [b] shows the streamfunction (contour interval is 0.5 m^2 s^{-1}), [c] shows the temperature field (contour interval is 2 degrees), [d] shows the salinity field (contour interval is 0.2 psu).

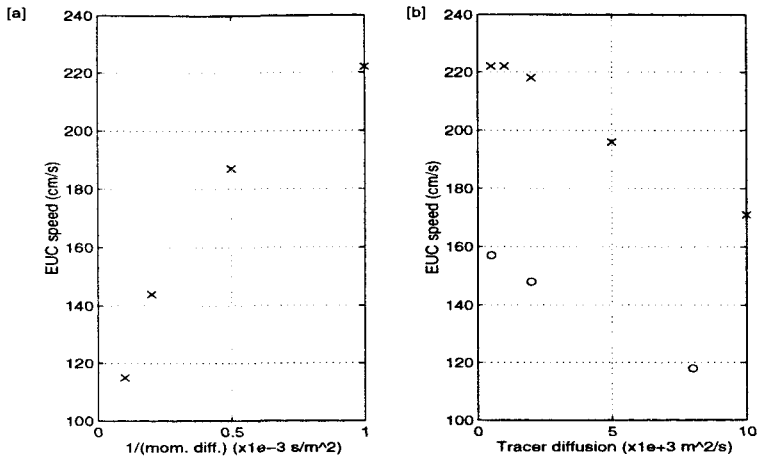

Figure 4.8: [a] shows the EUC speed plotted against $1/K_h$ for experiments B5-8 (A_h=1000 $m^2\ s^{-1}$). [b] shows the EUC speed plotted against A_h for experiments B1-5 (x) (K_h=1000 $m^2\ s^{-1}$) and for experiments B11-13 (o) (K_h=4000 $m^2\ s^{-1}$).

is held constant. The graph shows that the EUC speed is decreasing as K_h increases. The fit is not a straight-line fit which suggests that the relationship would be more accurately described as the EUC speed being proportional to $K_h^{\frac{-1}{n}}$, where n is greater than one. The reason for this lies in the definition of y'; defining y' as the meridional e-folding scale of the EUC, we find that y' increases as K_h increases. This implies that the inverse dependency of the EUC speed on K_h will be reduced. Figure 4.8 [b] shows the EUC speed plotted against A_h. The crosses indicate experiments B1-5 (where K_h is held constant at a value of 1000 $m^2\ s^{-1}$) and the circles indicate experiments B11-13 (where K_h is held constant at a value of 4000 $m^2\ s^{-1}$). The circles indicate that there is a one-to-one relationship between the EUC speed and the coefficient for the lateral diffusion of tracers. The gradient of the slope is estimated to be -5.2 $\times\ 10^{-7}\ cm^{-1}$. At high values of A_h, the crosses suggest a similar relationship, while at low values of A_h, there is some deviation from the relationship. The reason for this tendency of the points towards a common value for the EUC speed, rather than being proportional to the value of tracer diffusion, may suggest that a limit exists at which the value of the tracer diffusion is no longer important.

Figure 4.9 [a] shows the maximum value of the zonal current (the EUC core) on the Equator in $K_h - A_h$ parameter space for experiments A1, B1-13. It can be seen from the figure that the EUC speed decreases as both A_h and K_h increase. Unfortunately, at values of K_h less than 1000 $m^2 s^{-1}$ the model became unstable and we were unable to perform further experiments. The estimates of the lateral tracer diffusion coefficient due to intrusions, from

the previous chapter, suggest that the appropriate value of A_h is at least 1000 m^2 s^{-1}. Assuming that K_h is at least as large as this in magnitude (see table 1.1) we suggest that the experiments we have performed are in the correct region of parameter space.

Figure 4.9 [b] shows the maximum upwelling velocity on the Equator ($\times$ 10^{-3} cm s^{-1}) for experiments A1, B1-13. Figure 4.10 [a] shows the maximum value of the buoyancy frequency on the Equator ($\times$ 10^{-4} s^{-1}) and [b] shows the SST on the Equator ($^{\circ}$ C) for experiments A1, B1-13. The upwelling velocity, the stratification and the SST are approximately proportional to the magnitude of A_h. In figure 4.11, the upwelling velocity, the buoyancy frequency and the SST for experiments A1, B1-13 have been plotted against A_h and K_h. All three diagnostics are more closely related to A_h rather than K_h (A_h is also a better parameter to predict the three diagnostics than σ_{pr} or $A_h.K_h$). The diagnostics are not linearly related to A_h and generally show some indication of being multi-valued, which emphasises that we are examining a non-linear system. The relationships between A_h and the upwelling velocity and A_h and the stratification (as shown by figure 4.11 [a] and [c]) are most easily understood from expression 4.20. If we assume u, θ_x and θ_{yy} are invariant, then if A_h increases so must the vertical advection, $w\theta_z$. The results suggest that this is achieved via a change in both w and θ_z. Another important factor is the role of A_h on SST. At the surface, a decrease in A_h will reduce the exchange of the colder upwelled waters with the warmer waters off the Equator. This will decrease SST as A_h decreases (as observed in figure 4.11 [e]) and since the temperature below the thermocline is almost fixed, will lead to a decrease in stratification as A_h decreases (as observed in figure 4.11 [c]). This suggests that A_h is influencing the vertical structure of the Equatorial ocean both in the thermocline and in the surface layer.

Another consequence of varying the lateral tracer diffusion is the feedback on the vertical diffusion. The heat and zonal momentum balances for experiment B7 (the lateral diffusion reduced to a fifth of its value in the control experiment A1) are shown in figure 4.12. In a response to the reduction in the lateral mixing of heat and salt, the vertical mixing is increased between 100 and 150 m. Since the vertical diffusion coefficients for tracers and momentum are linked via the Pacanowski and Philander scheme, vertical mixing of momentum is also increased at this depth (as seen in the zonal momentum budget). Comparing with figure 4.6 we see that the vertical advection is the term which is most influenced by the interchange between vertical and lateral mixing. Maes et al. (1996) reported a similar result in their three-dimensional experiments using the Blanke and

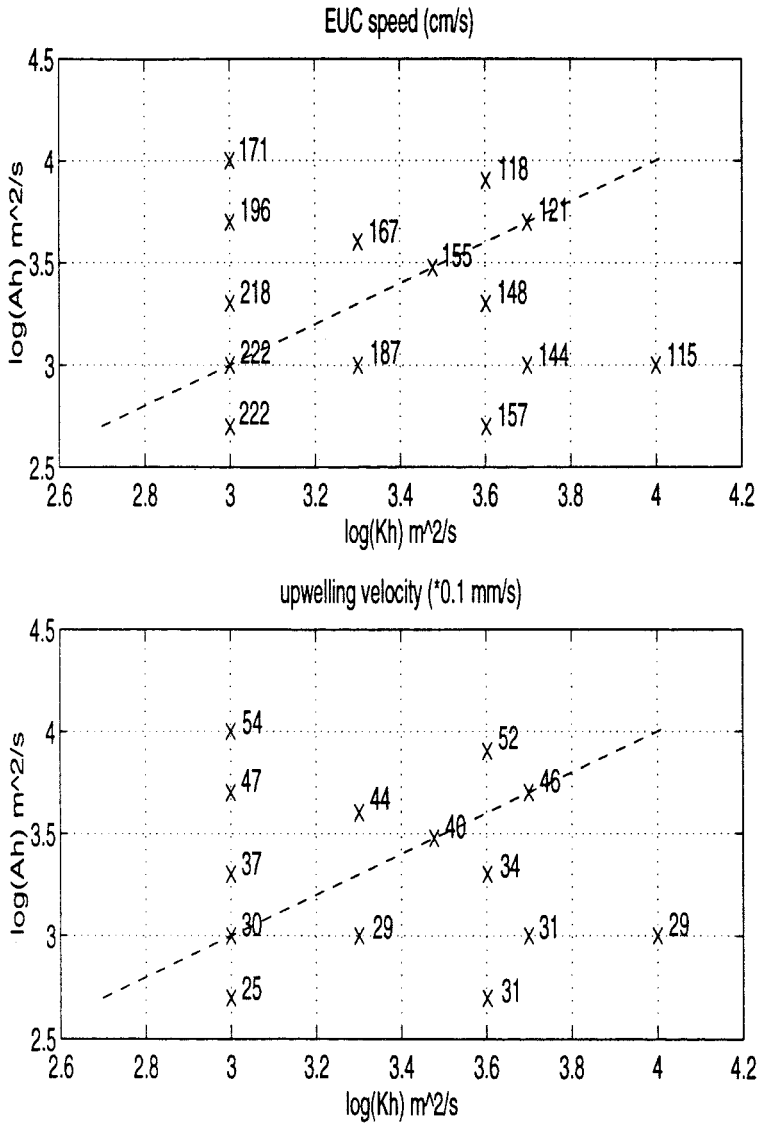

Figure 4.9: Experiments A1, B1-13. [a] Speed of the EUC at its core (cms^{-1}), [b] maximum value of upwelling velocity ($\times\ 10^{-3}\ cms^{-1}$) plotted in log($K_h$)-log($A_h$) parameter space. The dashed lines represent Prandtl number, $\sigma_{pr} = \frac{K_h}{A_h}$, equal to one.

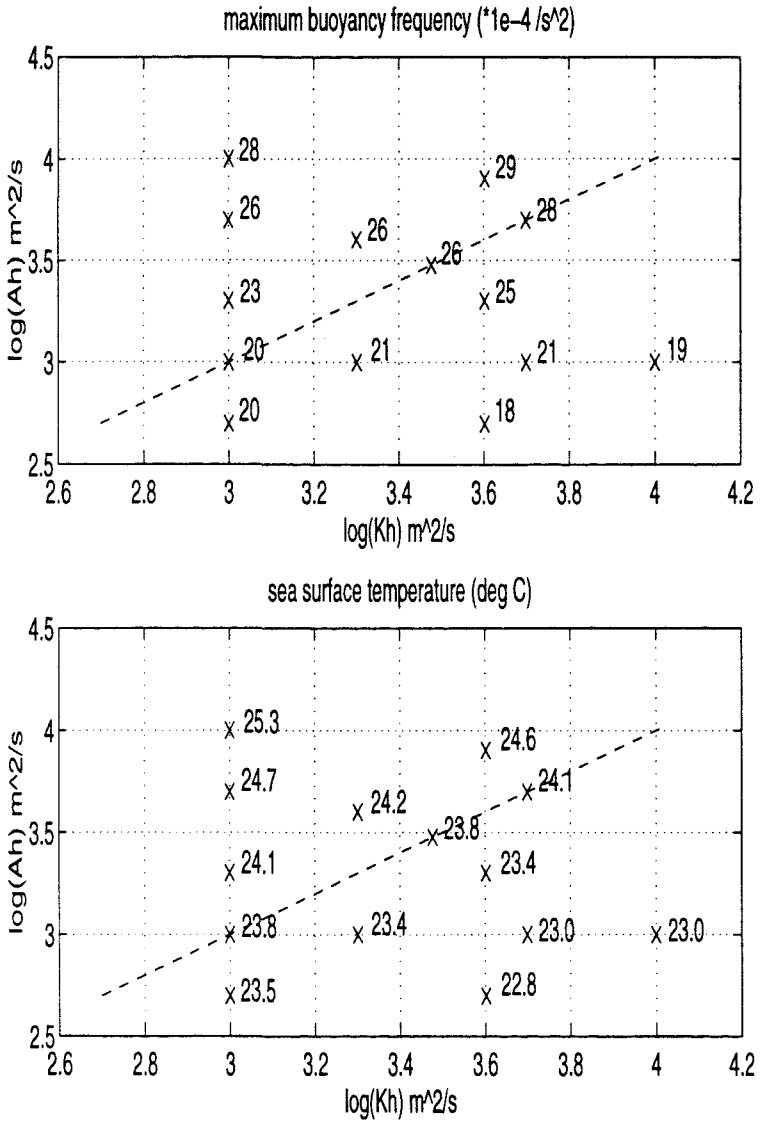

Figure 4.10: Experiments A1, B1-13. [a] Maximum value of the stratification ($\times\ 10^{-4}s^{-1}$), [b] SST on the Equator (^{o} C) plotted in log(K_h)-log(A_h) parameter space. The dashed lines represent Prandtl number, $\sigma_{pr} = \frac{K_h}{A_h}$, equal to one.

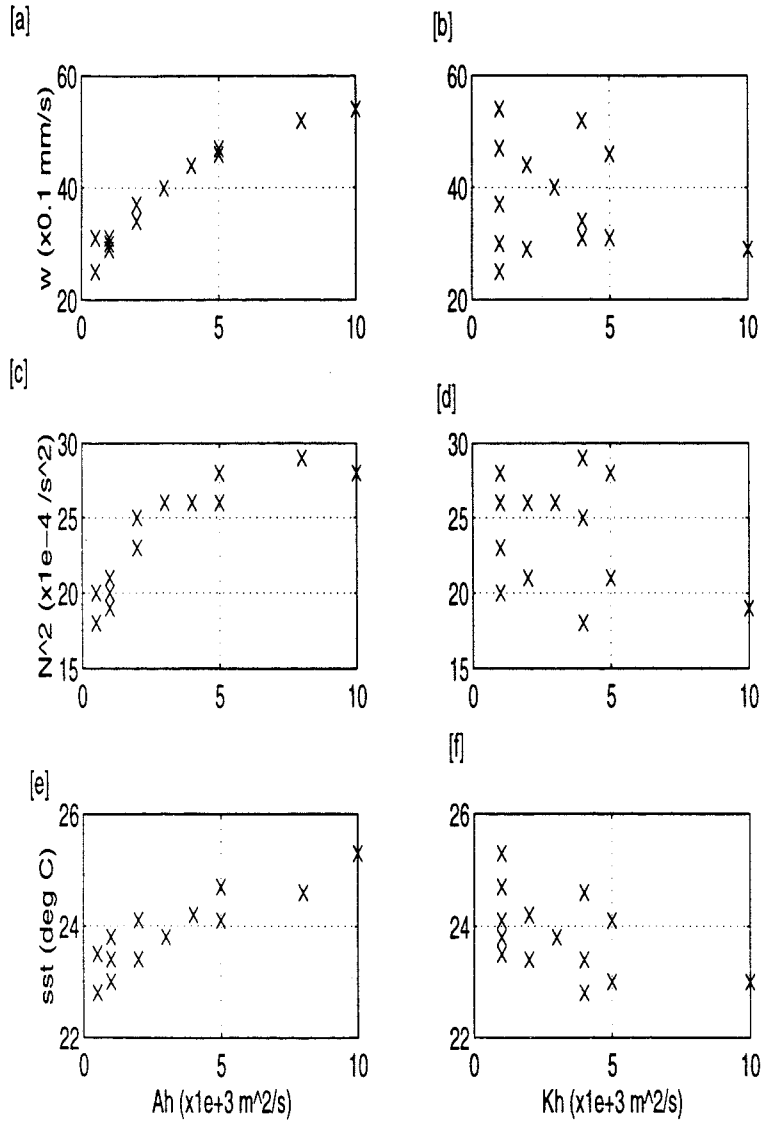

Figure 4.11: [a] shows the upwelling velocity plotted against the tracer diffusion, [b] shows the upwelling velocity plotted against the momentum diffusion, [c] shows the buoyancy frequency plotted against the tracer diffusion, [d] shows the buoyancy frequency plotted against the momentum diffusion, [e] shows SST plotted against the tracer diffusion and [f] shows SST plotted against momentum diffusion.

Delecluse scheme for vertical mixing. However a reduction in the lateral momentum diffusion (for example, experiment B2) does not appear to lead to a similar result. The reason for this is that the Richardson number is almost unchanged; the stratification is most strongly dependent on A_h, while even though the EUC speed increases as K_h decreases, the vertical gradient remains approximately constant (referring to figure 4.7 we see that the surface velocity field is also eastward).

So in our exploration of Prandtl number space we summarise the findings as follows:

- K_h acts directly on the EUC, with the EUC speed inversely proportional to K_h.
- A_h sets the upwelling velocity and the SST (which both influence the stratification) and influences the speed of the EUC which generally decreases as the magnitude of A_h increases.
- if A_h and K_h are sufficiently small, A_h no longer influences the speed of the EUC.
- reducing A_h leads to a corresponding increase in vertical mixing above the EUC core.

These results extend previous work on the role of the lateral diffusion coefficient suggesting that K_h and A_h can be chosen in such a way to set both the strength of the upwelling and the speed of the EUC by allowing $\sigma_{pr} \neq 1$. It is unclear whether the same results will hold in a three-dimensional model. In particular, non-linear feedbacks to the zonal pressure gradient (which is prescribed here) could add an extra degree of non-linearity in three dimensions.

4.5 Sensitivity to the heat-salt flux ratio

In experiments D1-4 we examine the importance of the ratio of vertical diffusion of heat to salt, γ. In D1 and D2, we keep the vertical diffusion coefficient of salinity the same as in the previous experiments (i.e. as given by equation 4.18) and prescribe the temperature diffusivity as a ratio of this, while in D3 and D4 we set the temperature diffusivity and prescribe the salinity diffusivity. The lateral diffusion coefficients of temperature and salinity are held constant and equal to 5 x 10^3 m^2s^{-1} as in experiment A1. Figure 4.13 shows profiles of the vertical temperature and salinity gradients, the vertical velocity and the zonal velocity on the Equator for the four experiments. The most apparent differences between the four experiments occur in the stratification of the upper 50 metres. The reason

for this is simply understood in terms of the surface boundary condition; if the diffusivity of heat/salt is increased/decreased then the change in the sea surface temperature/salinity is decreased/increased. This is because the tendency in the heat/salt budget is given by the difference between the surface heat/salt flux (the Haney term) and the vertical flux of heat/salt into the surface layer. Referring to figure 4.6 shows that vertical diffusion ceases to play a role in the tracer budgets below the upper 100 metres and therefore the primary effect of the diffusivity ratio is the change in the temperature/salinity stratification of the upper ocean, with small adjustments in the magnitude of the upwelling (O(7%)) and changes in the speed of the EUC being secondary (O(3%)). While applying this diffusivity ratio only to the vertical diffusion coefficient in the manner of Gargett and Holloway (1992) allows us to understand the influence of the surface boundary condition, it does not allow us to examine the effect of double-diffusion in the region we believe it to be important which is the thermocline. We will return to the heat-salt flux ratio in a later section.

Two further experiments (not included in the experiment list) were undertaken with the heat-salt flux ratio applied also to the lateral diffusion coefficient for tracers. The changes in the zonal velocity and upwelling velocity were dominated by changes in the diffusion coefficient for temperature. The only significant change in the fields due to the heat-salt flux ratio was a sharpening/ weakening of the salinity front.

4.6 The orientation of the mixing surfaces

In the previous sections we have assumed that the sub-grid scale transfer of heat and salt takes place along geodesic surfaces (i.e. parallel and perpendicular to the direction of acceleration due to gravity). Redi (1982) discussed the transfer of heat and salt along and across isopycnals, a representation which appeals more to physical intuition than geodesic coordinates. Introducing a parameter $\delta = \frac{\rho_y}{\rho_z}$ for the isopycnal slope, we can express the isopycnal and diapycnal diffusion of the tracer, τ, in the following way:

$$\frac{\partial}{\partial l}(A_i\frac{\partial \tau}{\partial l}) + \frac{\partial}{\partial n}(A_d\frac{\partial \tau}{\partial n}) =$$
$$\frac{1}{1+\delta^2}\frac{\partial}{\partial y}((A_i + \delta^2 A_d)\frac{\partial \tau}{\partial y} - \delta(A_i - A_d)\frac{\partial \tau}{\partial z}) +$$
$$\frac{1}{1+\delta^2}\frac{\partial}{\partial z}((A_d + \delta^2 A_i)\frac{\partial \tau}{\partial z} - \delta(A_i - A_d)\frac{\partial \tau}{\partial y})$$

where A_i and A_d are the isopycnal and diapycnal diffusion coefficients respectively. We

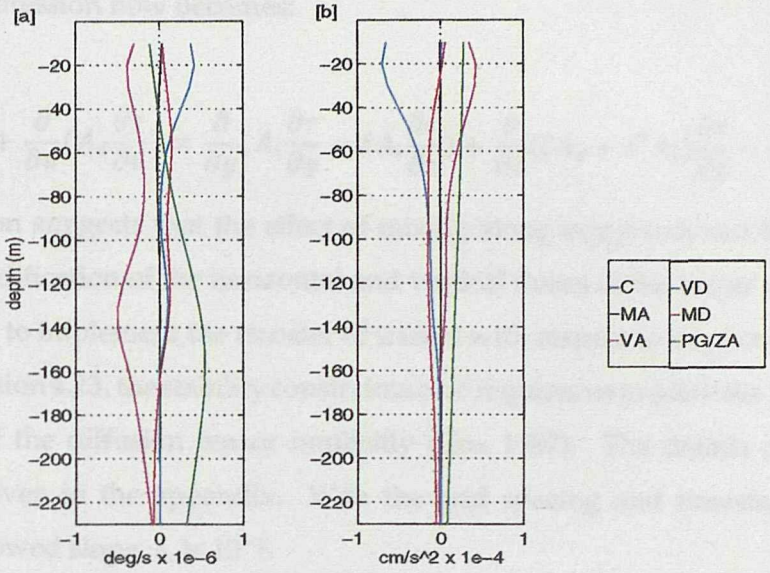

Figure 4.12: Experiment B7. [a] shows the heat budget (units are 1×10^{-6} ° C s^{-1}), on the Equator. [b] shows the zonal momentum budget (units are 1×10^{-6} m s^{-2}), at 0.25°N. The key is shown; VD represents vertical diffusion, MD meridional diffusion, PG pressure gradient, ZA zonal advection, C Coriolis, MA meridional advection, VA vertical advection.

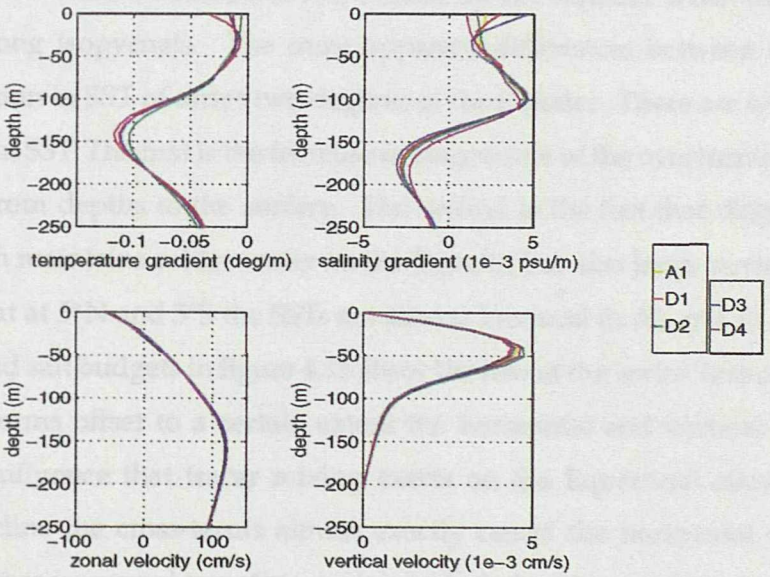

Figure 4.13: Comparison between the five experiments: A1, D1, D2, D3 and D4. [a] shows the vertical temperature gradient (°C m^{-1}), [b] shows the vertical salinity gradient ($\times 10^{-3}$ psu m^{-1}), [c] shows the zonal velocity (cm s^{-1}) and [d] shows the vertical velocity ($\times 10^{-3}$ cm s^{-1}).

can make two assumptions to simplify the above expression; that $A_d \ll A_i$ and that $\delta \ll 1$. The above expression now becomes:

$$\frac{\partial}{\partial l}(A_i \frac{\partial \tau}{\partial l}) + \frac{\partial}{\partial n}(A_d \frac{\partial \tau}{\partial n}) = \frac{\partial}{\partial y}(A_i \frac{\partial \tau}{\partial y} - \delta A_i \frac{\partial \tau}{\partial z}) + \frac{\partial}{\partial z}((A_d + \delta^2 A_i)\frac{\partial \tau}{\partial z} - \delta A_i \frac{\partial \tau}{\partial y}). \quad (4.23)$$

This expression suggests that the effect of mixing along isopycnals can be understood in terms of a modification of the horizontal and vertical fluxes of the tracer τ.

If we wish to implement the transfer of tracers with respect to isopycnal coordinates as given by equation 4.23, the stability constraints on δ requires us to solve the $A_{zz} (= A_d + \delta^2 A_i)$ component of the diffusion tensor implicitly (Cox 1987). The details of the numerical scheme are given in the appendix. With the grid spacing and timestep used here the maximum allowed slope, δ, is 10^{-2}.

Figure 4.14 shows the zonal velocity, [a], streamfunction, [b], temperature, [c], and salinity, [d], for experiment E1 where the parameters are the same as experiment A1 but the transfer of heat and salt is configured to be along isopycnals. There are differences between runs A1 (see figure 4.5) and E1 in all fields. The speed of the EUC increases by about 13% to 136 cm s^{-1} and the streamfunction increases in magnitude by approximately 3% to 6.1 m^2 s^{-1}. The thermocline is less diffuse off the Equator when the tracer transfer takes place along isopycnals. The most apparent differences between the fields is the marked reduction in SST of order two degrees at the Equator. There are two contributions to this change in SST. The first is the increase in magnitude of the overturning cell - bringing colder water from depths to the surface. The second is the fact that diapycnal mixing is reduced, which maintains colder water on the Equator but also large meridional gradients in SST such that at 5°N and 5°S the SSTs are almost identical in A1 and E1.

The heat and salt budgets in figure 4.15 show the role of the 'extra' terms in the diffusion tensor; these terms offset to a certain extent the horizontal and vertical diffusion terms reducing the influence that tracer mixing exerts on the Equatorial circulation. Indeed in the thermocline the cross-terms almost exactly cancel the horizontal diffusion terms, reducing the cross-isopycnal transfer which is included in the purely horizontal terms and acts to accelerate the EUC, as expected. If quasi-horizontal mixing is entirely isopycnal, it appears that its role in influencing the dynamics will be reduced and lateral diffusion of momentum will dominate. If the diapycnal mixing were identically zero then this would be true. In experiment E2, the isopycnal tracer diffusion was decreased to 2000 $m^2 s^{-1}$ (all

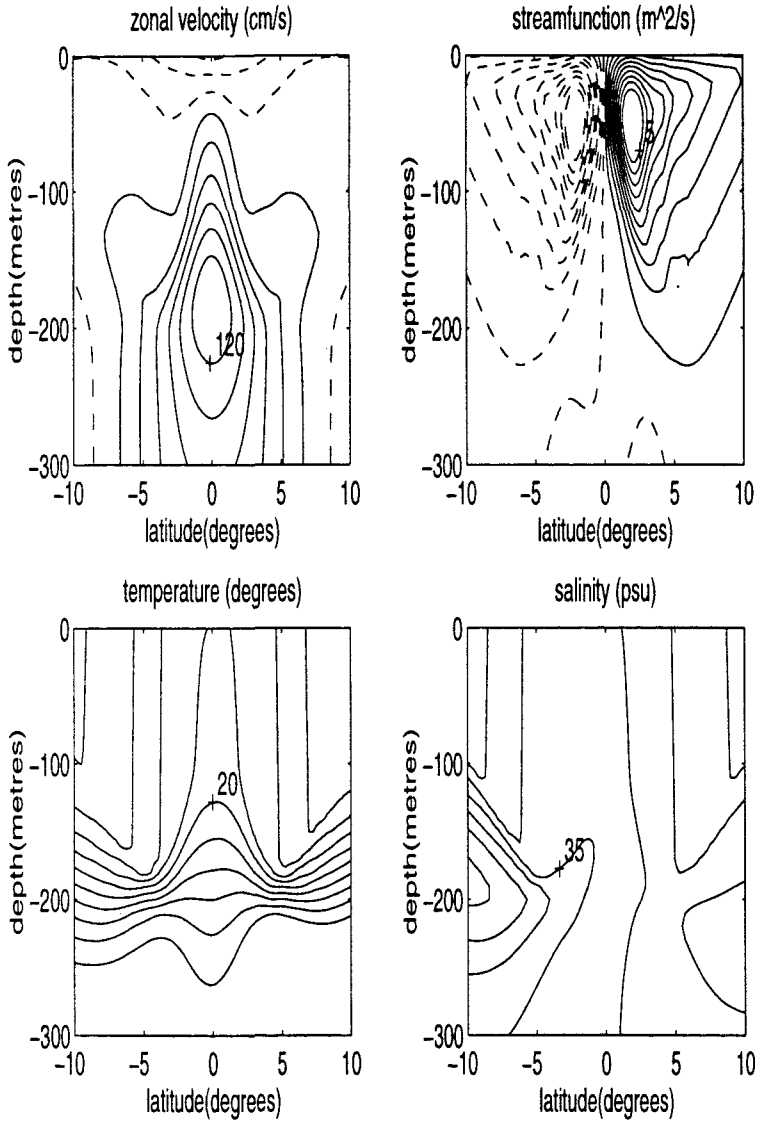

Figure 4.14: Experiment E1. [a] shows the zonal velocity field (the contour interval is 20 cm s^{-1} and dashed lines represent negative (westward) values), [b] shows the streamfunction (contour interval is 0.5 m^2 s^{-1}), [c] shows the temperature field (contour interval is 2 degrees), [d] shows the salinity field (contour interval is 0.2 psu).

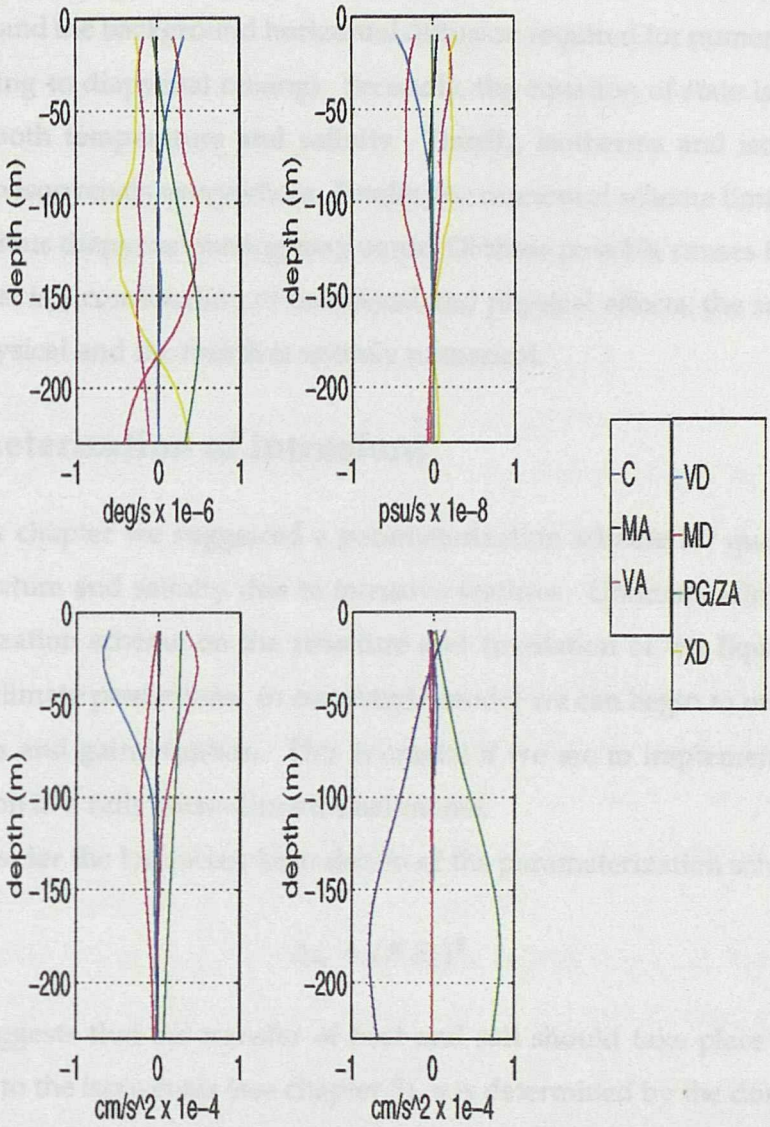

Figure 4.15: Experiment E1. [a] shows the heat budget (units are 1×10^{-6} ° C s^{-1}), [b] shows the salinity budget (units are 1×10^{-7} psu s^{-1}) on the Equator. [c] shows the zonal momentum budget (units are 1×10^{-6} m s^{-2}), [d] shows the meridional momentum budget (units are 1×10^{-6} m s^{-2}) at 0.25°N. The key is shown; VD represents vertical diffusion, MD meridional diffusion, XD off diagonal diffusion terms, PG pressure gradient, ZA zonal advection, C Coriolis, MA meridional advection, VA vertical advection.

other parameters were unchanged). This resulted in a small increase of the EUC speed to 139 cm s^{-1} and a decrease in the magnitude of the overturning cell to 5.0 m^2s^{-1}. What is the mechanism for this unexpected change? There are four distinct possibilities; firstly, the prescribed diapycnal diffusion is non-zero (the turbulent mixing prescribed by Pacanowski and Philander and the background horizontal diffusion required for numerical stability are both contributing to diapycnal mixing). Secondly, the equation of state is non-linear and a function of both temperature and salinity. Thirdly, isotherms and isohalines are not coincident with isopycnals everywhere. Finally, the numerical scheme limits the isopycnal slope and spurious diapycnal mixing may occur. Of these possible causes for the observed changes the first is a combination of numerical and physical effects, the second and third are entirely physical and the fourth is entirely numerical.

4.7 Parameterization of intrusions

In the previous chapter we suggested a parameterization scheme for quasi-lateral diffusion of temperature and salinity due to intrusive features. Understanding the impact of the parameterization scheme on the structure and circulation of the Equatorial ocean is paramount to climate predictions. In our simple model we can begin to understand some of these aspects and gain intuition. This is crucial if we are to implement the proposed parameterization in a fully three-dimensional model.

We will consider the Laplacian formulation of the parameterization scheme, i.e.

$$A_{br} \sim (NS_y)^{\frac{1}{2}}.$$

The scheme suggests that the transfer of heat and salt should take place along surfaces with a slope, η, to the isopycnals (see chapter 3). η is determined by the dominant 'source' interface and is positive (negative) for diffusive (finger) interfaces. We can prescribe the slope, δ, of the transfer surface by adding a pre-determined slope, η, to the calculated isopycnal slope, σ, in the isopycnal formulation of the code. Prescribing the mixing surface in this manner allows us to retain a turbulent parameterization (in this case Pacanowski and Philander) as the explicit diapycnal mixing scheme (A_d) and also prescribe additional diapycnal mixing via the slope to isopycnals η. We will discuss five implementations of this scheme. The simplest is where $A_h = A_{br}(y,z)$, i.e. the mixing takes place along geodesic surfaces (F1). In F2, $A_i = A_{br}(y,z)$, i.e. the mixing takes place along isopycnals. In F3,

A_i is given as for F2 but we make the transformation $\delta = \sigma + \eta$, i.e. diffusive interfaces dominate and γ is 0.5, i.e. the transfer of salt is greater than that of heat. In F4, $\delta = \sigma - \eta$, i.e. finger interfaces dominate and γ is 2.0, i.e. the transfer of heat is greater than that of salt. In F5, $\delta = \frac{1}{2}\sigma$ suggestive of diffusive interfaces dominating above the salinity maximum and finger interfaces dominating below. We note that the background stratification is in the finger sense below the salinity maximum but in the stable sense above the salinity maximum. Figure 4.16 is a schematic of the transfer surfaces for each of the experiments with the isopycnal surfaces also sketched. The constants are chosen such that the maximum value of the diffusion coefficient is approximately 5×10^3 m^{2}s^{-1}.

Figure 4.17 shows the zonal velocity fields and streamfunction fields for the experiment F1 along with experiments A1 and B7 (for comparison), figure 4.18 shows the temperature and salinity fields for the three experiments and figure 4.19 show the heat and salt budgets for the three experiments. Experiment F1 shows significant changes when compared to experiments A1 (where A_h = 5000 m^2 s^{-1}) and B7 (where A_h = 1000 m^{2}s^{-1}) in both the zonal velocity field and the overturning streamfunction (all three experiments have the same value K_h = 5000 m^2 s^{-1}). The maximum speed of the EUC is now 130 cm s^{-1} (inbetween the values of 121 cm s^{-1} for experiment A1 and 144 cm s^{-1} for experiment B7) and the strongest overturning is confined to nearer the Equator, although the maximum value of the overturning (5.8 m^2 s^{-1}) is similar to that described in experiment A1. The temperature and salinity fields are also similar to the results of experiment A1 with the sea surface values between those of experiments A1 and B7.

A similar result is also shown by the experiment F6 (not shown in figures 4.17 - 4.19). For experiment F6 the value of K_h is reduced to 1000 m^2 s^{-1} and should be compared with experiment B2 (A_h = 5000 m^2 s^{-1}) and experiment B5 (A_h = 1000 m^2 s^{-1}). The magnitude of the overturning streamfunction is identical to that of experiment B2 (confined to near the Equator) while the EUC speed, SST and SSS are between the observed values for experiments B2 and B5.

In the heat balances shown in figure 4.19 we see that by reducing A_h (comparing B7 to A1) the vertical mixing in the thermocline (150 m) is increased to compensate. Vertical advection is maximum in the thermocline for experiment B7 rather than at approximately 50 m for experiment A1. In both cases the maximum in lateral mixing is at a depth of approximately 50 m. When $A_h = A_{hr}$ (i.e. allowed to be variable in space), lateral mixing exhibits a different structure in the vertical compared with the constant diffusion case.

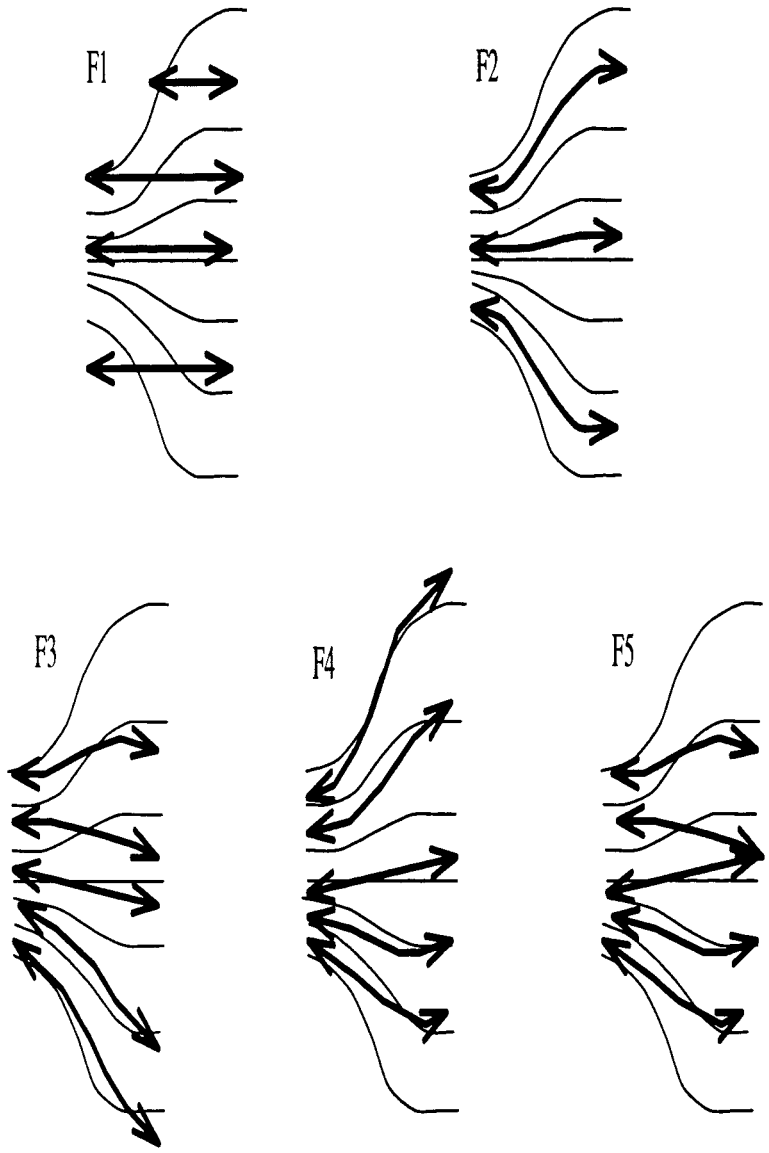

Figure 4.16: Schematic of the transfer surfaces in the five experiments with the parameterization. F1 shows the transfer surfaces being parallel to geodesic surfaces, F2 shows the transfer surfaces as isopycnal surfaces, F3 shows the transfer surfaces sloping downwards across isopycnals, F4 shows the transfer surfaces sloping upwards across isopycnals and F5 shows the transfer surfaces sloping in the opposite direction to isopycnal surfaces.

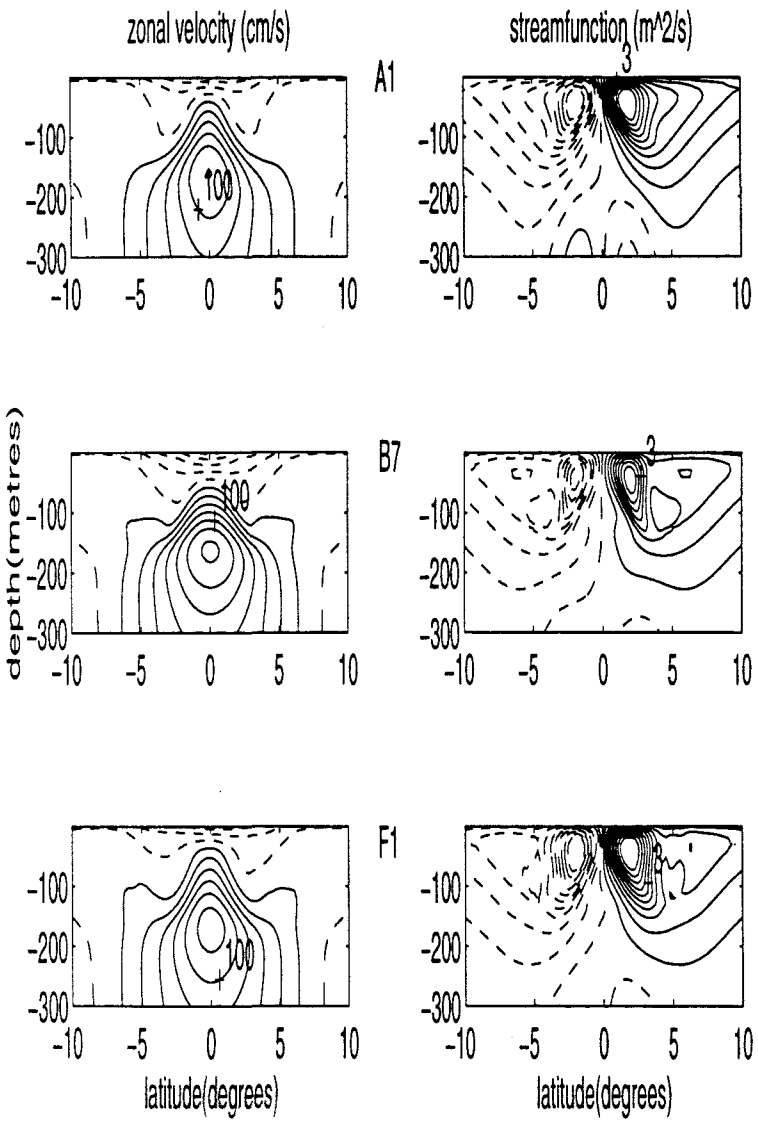

Figure 4.17: Left-hand panels show the zonal velocity field for experiments A1, B7, F1 (contour interval 20 cm s^{-1}). Right-hand panels show meridional streamfunction for experiments A1, B7, F1 (contour interval 0.5 $m^2 s^{-1}$).

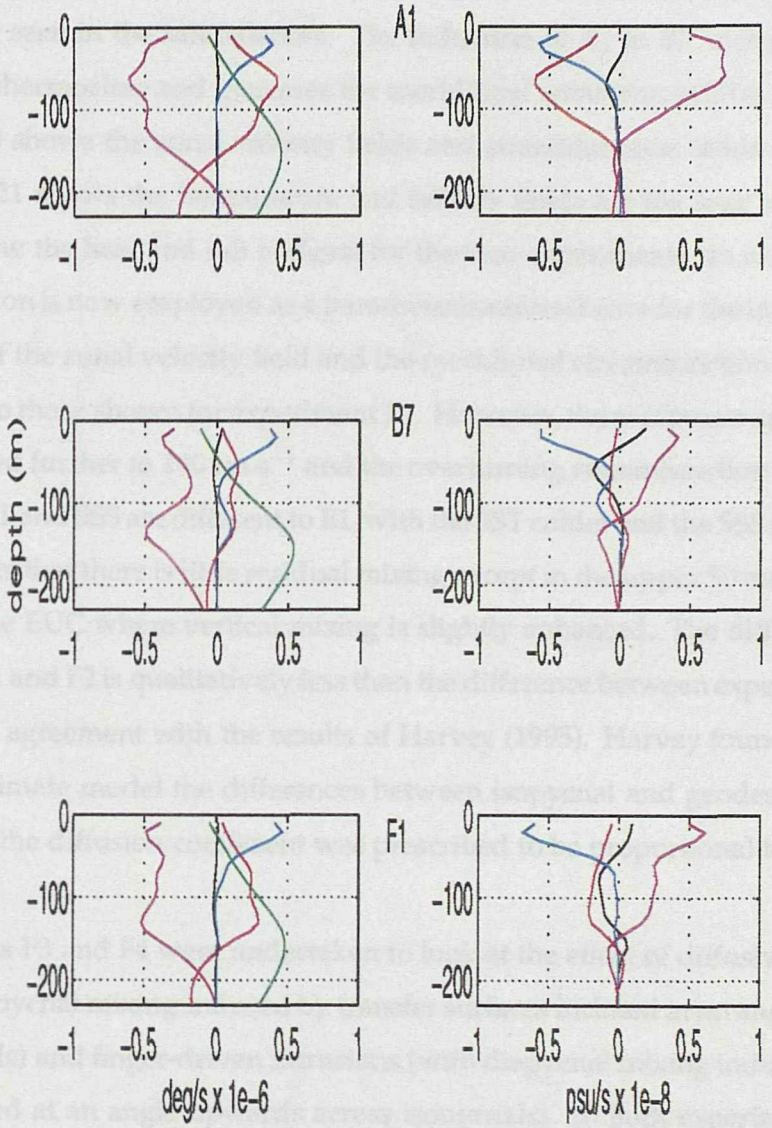

Figure 4.19: Left-hand panels show the heat budgets for experiments A1, B7, F1 (units are 1×10^{-6} ° C s^{-1}). Right-hand panels show salinity field for experiments A1, B7, F1 (units are 1×10^{-7} psu s^{-1}).

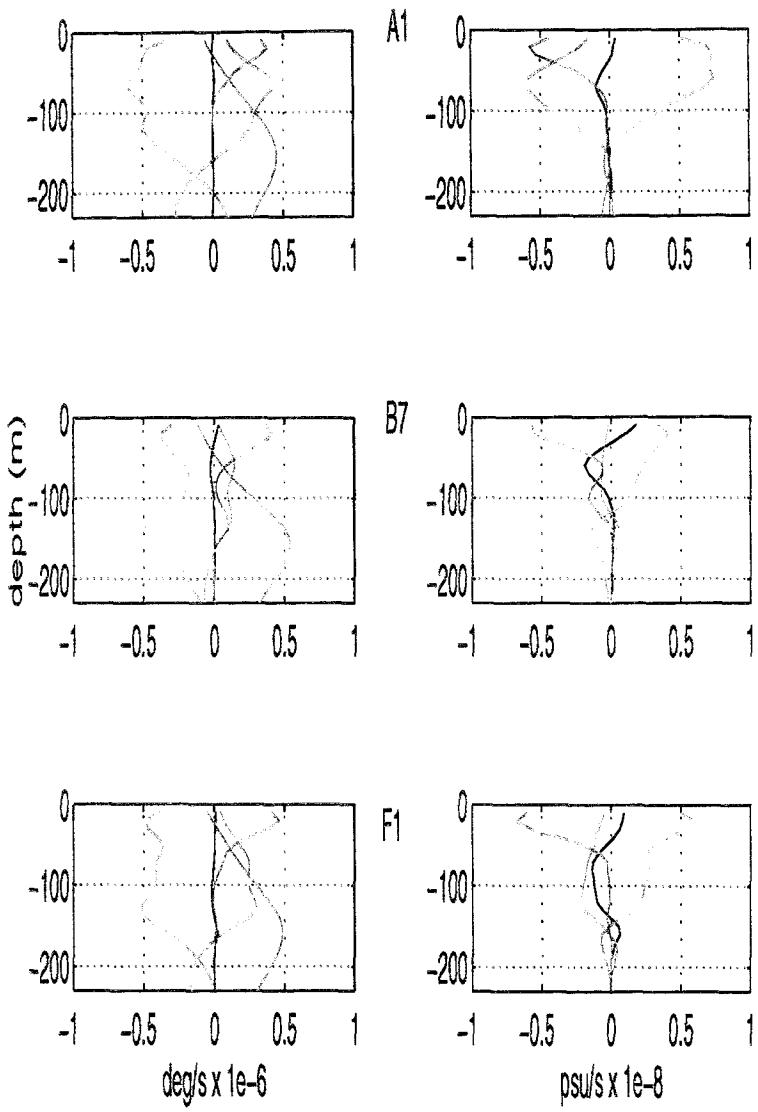

Figure 4.19: Left-hand panels show the heat budgets for experiments A1, B7, F1 (units are 1×10^{-6} ° C s^{-1}). Right-hand panels show salinity field for experiments A1, B7, F1 (units are 1×10^{-7} psu s^{-1}).

Lateral mixing is maximum in the thermocline with some extra vertical mixing (compared to experiment A1) at 100 m. The maximum value of A_h directly influences the vertical advection term, $w\theta_z$, while the EUC speed is influenced by a smaller value of A_h. Away from the Equator where the stratification in the upper 100 metres is weak, the vertical advection is reduced. This leads to the observed pattern in the streamfunction. A similar pattern can be seen in the salt balances. The reduction of A_h in B7, increases the vertical mixing in the thermocline and increases the meridional advection at 50 m.

Figure 4.20 shows the zonal velocity fields and streamfunction fields for experiments F2-5, figure 4.21 shows the temperature and salinity fields for the four experiments and figure 4.22 show the heat and salt budgets for the four experiments. In experiment F2 the parameterization is now employed as a parameterization scheme for the isopycnal mixing. The patterns of the zonal velocity field and the meridional streamfunction are similar (but not identical) to those shown for experiment F1. However, the maximum speed of the EUC is now increased further to 140 cm s^{-1} and the overturning streamfunction decreases to 5.0 m^2 s^{-1}. The SST and SSS are different to E1, with the SST colder and the SSS saltier. The heat budget suggests that there is little residual mixing except in the upper 50 metres and also at the depth of the EUC where vertical mixing is slightly enhanced. The difference between experiments F1 and F2 is qualitatively less than the difference between experiments A1 and E1, which is in agreement with the results of Harvey (1995). Harvey found that in a two-dimensional climate model the differences between isopycnal and geodesic mixing were reduced when the diffusion coefficient was prescribed to be proportional to the buoyancy frequency.

Experiments F3 and F4 were undertaken to look at the effect of diffusive-driven intrusions (with diapycnal mixing induced by transfer surfaces inclined at an angle downwards to the isopycnals) and finger-driven intrusions (with diapycnal mixing induced by transfer surfaces inclined at an angle upwards across isopycnals). In both experiments the zonal velocity fields have an inherent asymmetry which is induced by the asymmetric transfer surfaces; in figure 4.16 the transfer surfaces for experiments F3 and F4 do not have mirror images on the opposite side of the Equator (the Northern side is shown), while for experiments F1, F2 and F5 the transfer surfaces are mirror images. This asymmetry would be due to the transfer of tracers originating at the front of the salinity maximum water. Both experiments exhibit a decrease in the speed of the EUC; in F3 its speed is 138 cm s^{-1} and in F4 its speed is 135 cm s^{-1}. The structure of the streamfunction is similar in both cases

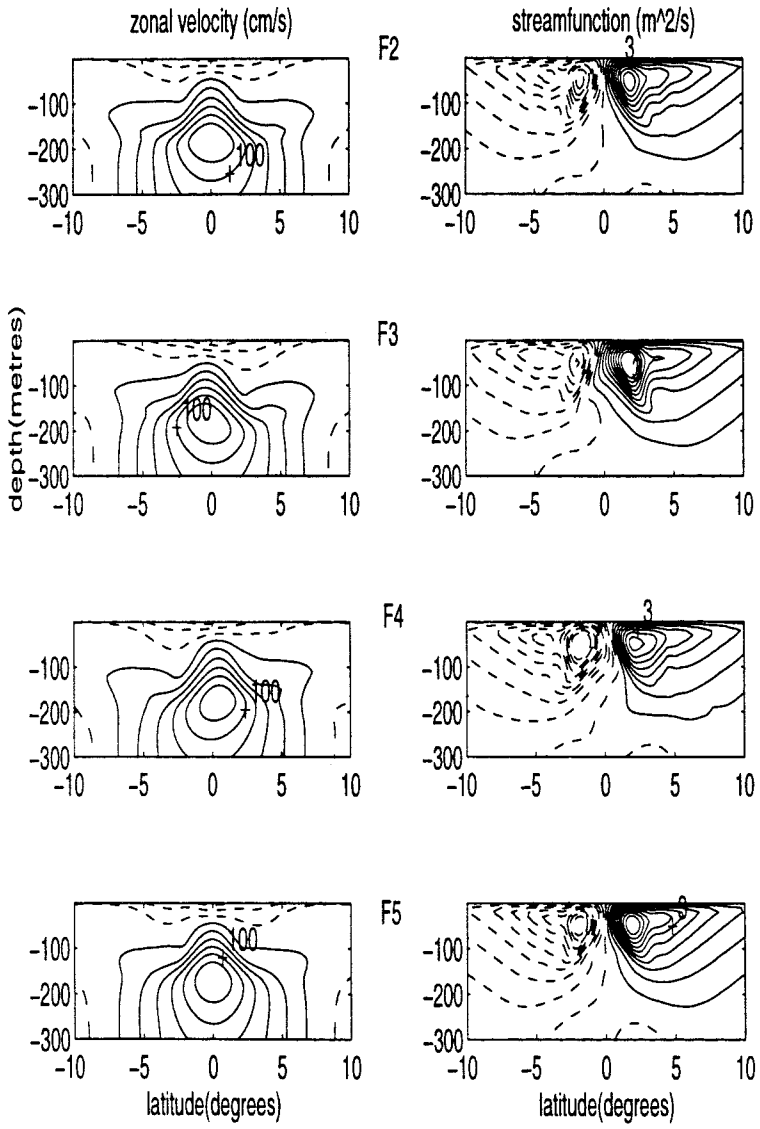

Figure 4.20: Left-hand panels show the zonal velocity field for experiments F2-5 (contour interval 20 cm s^{-1}). Right-hand panels show meridional streamfunction for experiments F2-5 (contour interval 0.5 $m^2 s^{-1}$).

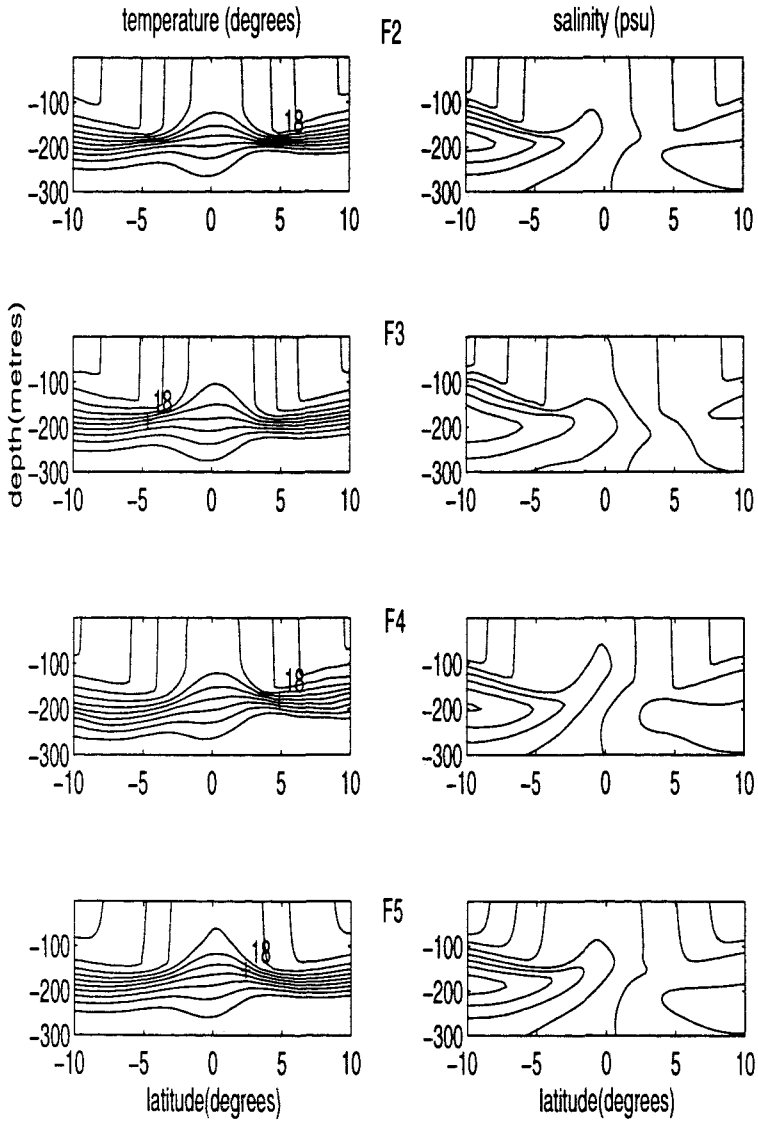

Figure 4.21: Left-hand panels show the temperature field for experiments F2-5 (contour interval 2 °). Right-hand panels show salinity field for experiments F2-5 (contour interval 0.2 psu).

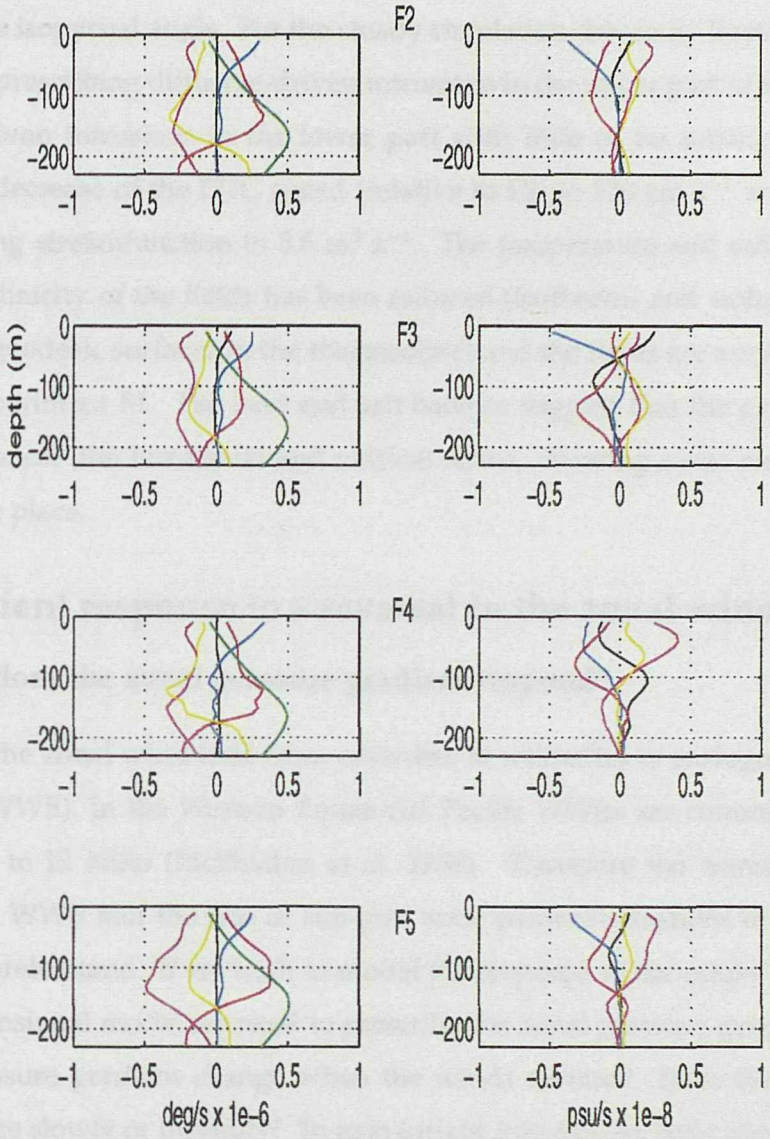

Figure 4.22: Left-hand panels show the heat budgets for experiments F2-5 (units are 1×10^{-6} ° C s^{-1}). Right-hand panels show salinity field for experiments F2-5 (units are 1×10^{-7} psu s^{-1}).

with the magnitude decreasing from 6.0 $m^2\ s^{-1}$ to 4.3 $m^2 s^{-1}$. The temperature and salinity fields are similar to those shown for experiment F2 except in the salinity fields where there is some evidence of the vertical gradients increasing due to upgradient transfer (north of the Equator for F2 and south of the Equator for F3).

In experiment F5 the transfer surfaces were prescribed to be at an angle which was half that of the isopycnal angle. For the steady circulation driven by Easterly winds this is equivalent to prescribing diffusive-driven intrusions in the upper part of the water column and finger-driven intrusions in the lower part with little or no mixing at depth. This resulted in a decrease of the EUC speed (relative to F2) to 136 cm s^{-1} and an increase in the overturning streamfunction to 5.6 $m^2\ s^{-1}$. The temperature and salinity fields show that the baroclinicity of the fields has been reduced (isotherms and isohalines are almost aligned with geodesic surfaces in the thermocline) and the fields are very similar to those shown for experiment F1. The heat and salt balance suggest that the extra terms do not completely 'cancel' the horizontal and vertical terms, allowing some residual diapycnal mixing to take place.

4.8 Transient response to a reversal in the zonal wind field

4.8.1 How does the zonal pressure gradient respond?

A reversal in the zonal wind field from easterlies to westerlies is analogous to a Westerly Wind Burst (WWB). In the Western Equatorial Pacific WWBs are commonly believed to be precursors to El Niño (McPhaden et al. 1988). Therefore the transient response of the ocean to a WWB and the role of sub-grid scale parameterizations in this response is important to understand. If we wish to model the response of the ocean to a WWB using this two-dimensional model we need to prescribe the zonal pressure gradient. How does the zonal pressure gradient change when the winds reverse? Does the zonal pressure gradient change slowly or instantly? To gain insight into this we have used the TAO array to look at the zonal pressure gradient and the zonal wind field on the Equator at 156°E. We have taken temperature measurements from two TAO moorings at 158°E and 154°E and the meteorological data from the IMET buoy at 156°E for a 100 day period starting 16th September 1992 and ending 23rd December 1992. This period was chosen for two reasons; firstly, WWBs were observed during this period (McPhaden 1993) and secondly, we were able to obtain concurrent meteorological and subsurface data during the period.

This period was the three months prior to the POI SeaSoar sections which were described in chapter 2. In figure 4.23 [a] we have plotted the zonal wind velocity at 156°E. During days 15-35 the zonal wind velocity is predominantly easterly (negative), while during subsequent times the wind field is predominantly westerly (positive) and punctuated by three strong events when the zonal wind velocity is in excess of 5 m s^{-1}.

We can evaluate the zonal pressure gradient using the hydrostatic relationship:

$$\frac{\partial P}{\partial x} = \int_{-\inf}^{0} \frac{g}{\rho_o} \frac{\partial \rho}{\partial x} dz.$$

If we make the assumption that density is a function only of temperature, then we can calculate the density gradient by calculating the temperature difference of the moorings at 158°E and 154°E. We then integrate the zonal temperature gradient upwards assuming a reference point where the zonal pressure gradient is zero at a depth of 300 m. In figure 4.23 [b] we show the evolution of the zonal pressure gradient (-P_x) between the surface and 300 metres during the 100 day period. The gaps in the figure indicate times when there was no temperature record at either 154°E or 158°E. Qualitatively, the easterly winds at the start of the record are balanced by a zonal pressure gradient which is predominantly positive at the surface. The subsequent westerlies are balanced by a negative zonal pressure gradient. At zero lag the zonal wind and the surface zonal pressure gradient are anti-correlated, with a correlation coefficient of -0.29. This is in accord with the three-dimensional numerical experiments performed by Zhang (1995) which showed the zonal pressure gradient reversing within a day to balance the zonal wind stress. Supported by the observational evidence, we will model the zonal pressure gradient as acting to balance the zonal wind stress at all times, i.e. when the wind field reverses so does the zonal pressure gradient.

4.8.2 The role of lateral mixing

In experiments G1-3 we spin the ocean up to a steady state for a year and then reverse the wind field. By examining the fields and the budgets we can diagnose the role of mixing in transients. Figure 4.24 shows the zonal velocity, meridional streamfunction, temperature and salinity fields after ten days for experiment G1 (where the values of A_h and K_h are constant and the same as those for experiment A1). The zonal velocity has reversed to eastward at the surface and the EUC, while weakened, is still maintained. There is a weak westward flow in between these two currents which is reminiscent of the SubSurface Reversing Current (SSRC). In the meridional streamfunction field we see that the original

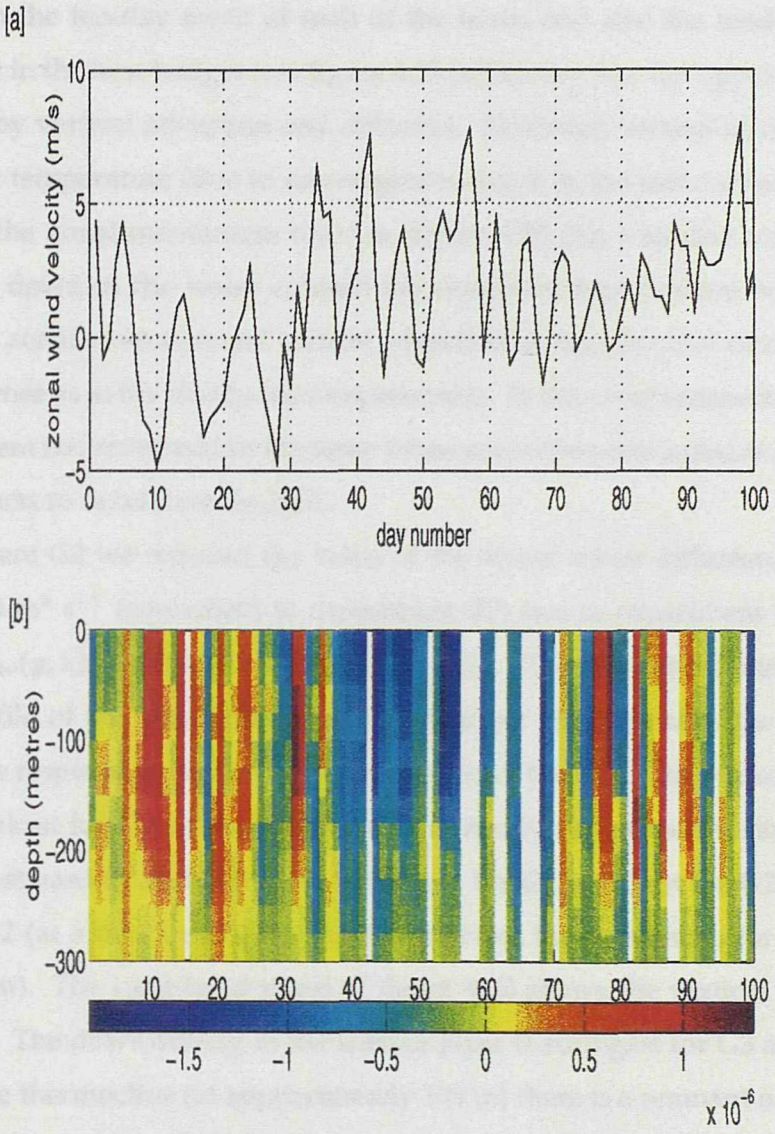

Figure 4.23: Upper panel shows the zonal wind velocity during a 100 day period from 16th September 1992 to 23rd December 1992 on the Equator at 156°E (m s^{-1}). Lower panel shows the zonal pressure gradient on the Equator at 156°E for the same time period (m s^{-2}). The zonal pressure gradient was calculated assuming that density is a function only of temperature, using the temperature measurements on the TAO array at 154°E and 158°E.

upwelling circulation has been pushed downward and a downwelling circulation cell overlies this. This cell caps the circulation with warmer, fresher surface waters and there is some evidence for decompression of the isotherms.

What is the dynamical and buoyancy balance of this transient state? To address this, we have taken the ten-day mean of each of the terms and also the tendency term. For experiment G1 in the heat budget (see figure 4.25 [a]) we see that the upper ocean response is dominated by vertical advection and diffusion. However, vertical advection now acts to increase the temperature (due to convergence) and is in the same sense as the vertical diffusion. In the zonal momentum balance (figure 4.25 [b]) a similar scenario is taking place. Lower down in the water column the dominant heat balance remains between lateral mixing, zonal advection and vertical advection, although zonal advection is now in the opposite sense as in the steady-state experiments. In the zonal momentum balance, the pressure gradient has reversed but the other terms are in the same sense as the steady-state balance. This acts to decelerate the EUC.

In experiment G2 we reduced the value of the lateral tracer diffusion, A_h, from 5000 $m^2\ s^{-1}$ to 1000 $m^2\ s^{-1}$ (equivalent to experiment B7) and in experiment G3 we allowed A_h to equal $A_{hr}(y,z)$ (equivalent to experiment F1). The left-hand panel of figure 4.26 shows the profile of the zonal velocity on the Equator ten days after the reversal of the wind field. The response is similar in each experiment; the EUC has weakened in all three cases (it is weakest for G1, as expected from the steady-state experiments). The surface currents are eastward in all three cases (strongest for G1, weakest for G2). The SSRC is just zero for G2 (at a depth of 70 m) and is eastward, but minimum, for G1 and G3 (at a depth of 80 m). The right-hand panel of figure 4.26 shows the vertical velocity profile at the Equator. The downwelling in the surface layer is strongest for G3 and weakest for G2, while in the thermocline (at approximately 100 m) there is a remnant of the upwelling driven by easterly winds. This upwelling is strongest for G2 and weakest for G1. The larger magnitude of the upwelling for experiment G2 appears to be directly connected to the contribution of turbulent mixing in the thermocline. The heat and momentum budgets for experiment G2 (figure 4.25 [c] and [d]) show almost a doubling of magnitude of vertical advection of heat and zonal momentum. The budgets for experiment G3 are similar to those shown for experiment G1, which is due to the fact that lateral mixing dominates everywhere below the surface layer. The crucial factor in determining the response of the ocean to the reversal in the wind field, as far as the mixing of heat and momentum is

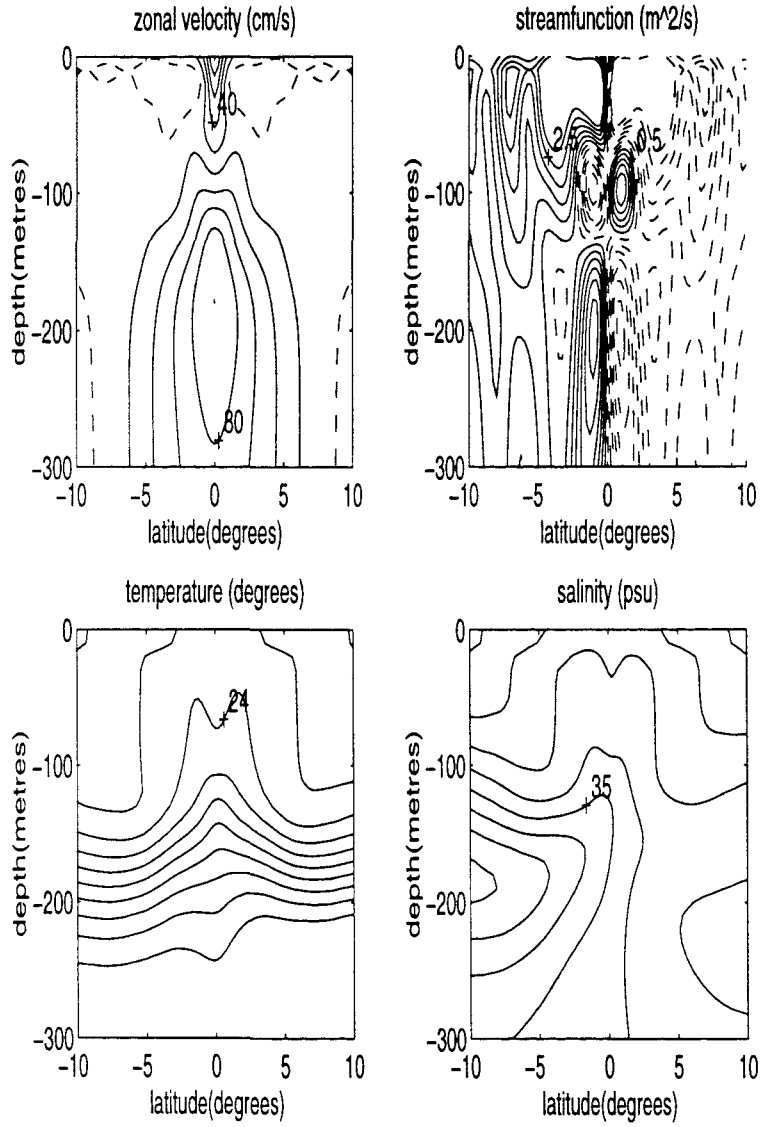

Figure 4.24: Experiment G1: 10 days after the winds reverse from easterly to westerly. [a] shows the zonal velocity field (the contour interval is 20 cm s^{-1} and dashed lines represent negative (westward) values), [b] shows the streamfunction (contour interval is 0.5 m^2 s^{-1}), [c] shows the temperature field (contour interval is 2 degrees), [d] shows the salinity field (contour interval is 0.2 psu).

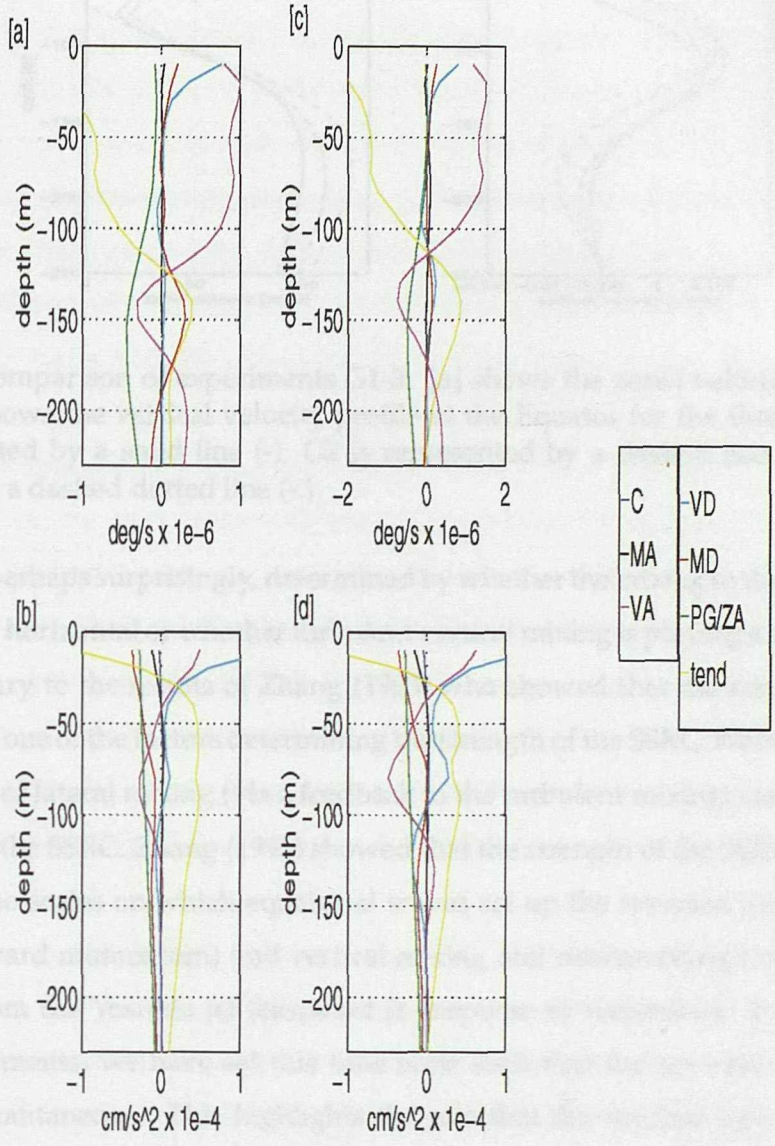

Figure 4.25: Experiment G1: 10 day mean of the heat, salt and momentum budgets during the period of reversed windstress. [a] shows the heat budget (units are 1×10^{-6} ° C s^{-1}), on the Equator. [b] shows the zonal momentum budget (units are 1×10^{-6} m s^{-2}), at 0.25°N. Experiment G2: 10 day mean of the heat, salt and momentum budgets during the period of reversed windstress. [c] shows the heat budget (units are 1×10^{-6} ° C s^{-1}), on the Equator. [d] shows the zonal momentum budget (units are 1×10^{-6} m s^{-2}), at 0.25°N. The key is shown; VD represents vertical diffusion, MD meridional diffusion, PG pressure gradient, ZA zonal advection, C Coriolis, MA meridional advection, VA vertical advection, tend tendency term.

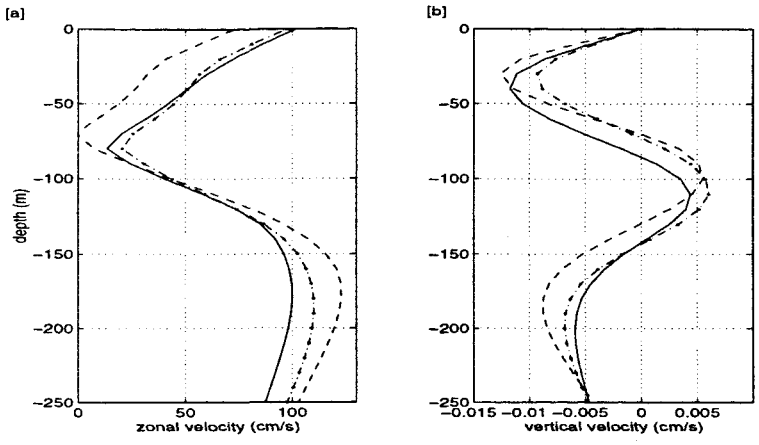

Figure 4.26: Comparison of experiments G1-3. [a] shows the zonal velocity profile at the Equator, [b] shows the vertical velocity profile at the Equator for the three experiments. G1 is represented by a solid line (-), G2 is represented by a dashed line (—) and G3 is represented by a dashed dotted line (-.).

concerned, is, perhaps surprisingly, determined by whether the mixing in the thermocline is predominantly horizontal or whether turbulent vertical mixing is playing a role. This result is complimentary to the results of Zhang (1995) who showed that the zonal width of the windburst was one of the factors determining the strength of the SSRC. We have shown that the magnitude of lateral mixing (via a feedback to the turbulent mixing) can also influence the strength of the SSRC. Zhang (1995) showed that the strength of the SSRC depended on the relative time scales on which equatorial waves set up the reversed pressure gradient (driving westward momentum) and vertical mixing and downwelling transfer eastward momentum from the Yoshida jet (eastward in response to westerlies). In the context of Zhang's experiments, we have set this time scale such that the reversal of the pressure gradient is instantaneous. This highlights the role that the residual upwelling plays in adding westward momentum between the surface and the thermocline and accelerating the SSRC.

4.9 Discussion

The two-dimensional numerical model is able to represent a simplified version of dynamical and thermodynamical Equatorial processes. It would be naive to believe that all the results will translate directly to three-dimensional experiments. The robustness of the results from the two-dimensional model remains to be examined in three-dimensional

experiments. There are three main shortcomings of the two-dimensional model. Firstly, the zonal advection of zonal momentum (uu_x) term is absent and this term was shown to be important in all the dynamical regimes identified by Wacongne (1988). Secondly, the vertical velocity due to the zonal slope of the thermocline is absent (Bryden and Brady 1985). Thirdly, Equatorial Kelvin and Rossby waves are absent, which implies that effects due to wave-mean flow interaction are not included (Johnson and McPhaden 1993). The reduction by one dimension however, allows us to gain insight into the interaction between the mixing prescriptions and the dynamics and also to run a large number of sensitivity experiments. The results presented in this chapter represent those results which are most relevant to this thesis and the questions which have arisen in the light of the previous chapters.

The experiments varying the magnitude of the constant lateral diffusion coefficients for tracers and momentum in Prandtl number space clarify many points which appear to have been overlooked in previous work. The experiments of Maes et al. (1996) treated the lateral diffusion coefficient as one parameter. Our experiments suggest that there are two parameters: the lateral diffusion coefficient for tracers and the lateral diffusion coefficient for momentum. These two parameters play different roles in influencing the dynamics and vertical structure of the ocean. Extending the experiments of Maes et al. (1996) to Prandtl numbers greater and less than unity would establish the robustness of these results for OGCMs.

We have shown that diffusing tracers along isopycnals alters the large-scale dynamical and tracer fields. In these experiments the role of the diffusion coefficient for tracers is similar to its role when mixing of tracers takes place along geodesic surfaces, although to a lesser extent. The possible reasons for this result were presented earlier. In the previous chapter we discussed the heat-salt flux ratio. It seemed important to establish whether this ratio was an important parameter for setting the dynamics. We have only discussed the results when the ratio was applied to the vertical diffusion coefficient, since it is the vertical mixing which is most likely to be found in ratios such as 2:1. The results in this case suggest that it is not an important parameter in the Equatorial region (at least with the parameterization scheme employed here). This is in agreement with the results of Gargett and Holloway (1992) who found that the ratio was only of consequence at high latitudes.

The intrusion parameterization scheme, while it remains to be tested in a three- dimensional model, may potentially be important in influencing the large-scale dynamics. The

SSTs were much warmer away from the Equator than when constant geodesic mixing was implemented and the circulation cell appeared less broad. Parameterizing as a function of the buoyancy frequency meant that the differences between isopycnal and geodesic mixing were reduced in agreement with the results of Harvey (1995). In contrast, prescribing cross-isopycnal fluxes in the sense of finger or diffusive intrusions created an asymmetry in the large-scale circulation and large changes in the temperature and salinity fields. Prescribing the mixing in the sense of diffusive (finger) intrusions above (below) the salinity maximum was effective at reducing the baroclinicity of the system and the results were comparable with those when geodesic mixing was employed. It is difficult to assess which implementation is best since we do not know what we should use as a measure. Observations might be one choice, but it is difficult to reproduce the complex structure of the Equatorial region using our simplified model. Personal preference lies with the implementation employed in experiment F5 since from an intellectual view point it does things 'right' for the right reasons. The mixing is prescribed across isopycnals in a manner consistent with the dominant interface being a function of the background stratification of salt. For simplicity we have prescribed the change in the direction of cross-isopycnal transfer to occur when the isopycnal slope changes sign. However, for transient experiments, an appropriate prescription of the transfer surfaces may be one where the orientation of the surface is related to the vertical salinity gradient. It is coincidental that for these steady-state experiments the two prescriptions should be almost identical.

Our parameterization was implemented in such a way as to allow the Pacanowski and Philander (1981) scheme for turbulent mixing to be retained in the vertical direction. This was done in order to parameterize the turbulent shear-induced, Richardson number dependent, mixing in the upper ocean (mixed layer). The Pacanowski and Philander scheme produces little vertical mixing below 50 m for experiment A1, but when the lateral mixing of tracers is reduced (experiment B7) vertical mixing in the thermocline is increased, reminiscent of the result of Maes et al. (1996). The scheme of Blanke and Delecluse (1993), based on a 1.5 turbulence closure model, is far more effective at producing shear-induced mixing in the core of the EUC. The parameterization scheme we are concerned with is designed to represent the fluxes produced by double-diffusive interleaving. If turbulence is high in the region where interleaving may take place (i.e. in the thermocline where the lateral salinity gradients are large), then it is likely that the double-diffusive interfaces will be broken down and interleaving will be weak (Linden 1971). The one-dimensional

model of Walsh and Ruddick (1996) assumes that turbulent and double-diffusive fluxes are additive. Their model requires some background turbulence to produce steady-state double-diffusive intrusions and even when the turbulence is intense the character of the intrusions is unchanged. In the thermocline, the magnitude of our parameterized lateral mixing is large enough to suppress turbulent mixing (via the Pacanowski and Philander scheme), thus avoiding any possible contradiction. Yet the question still remains – how should we reconcile our parameterization of double-diffusive interleaving with parameterizations of shear-induced turbulent mixing? The experiments of Maes et al. (1996) and those performed here give some clue as to how this may be possible. When the lateral diffusion coefficient is low, turbulent mixing in the EUC core is high, while when the lateral diffusion coefficient is high, turbulent mixing in the EUC core is low. This suggests that using the two schemes together the possibility of an interaction occurring between double-diffusive interleaving induced diapycnal mixing and turbulence induced diapycnal mixing should exist. Presumably as the thermocline/ salinity gradients weaken turbulent mixing could dominate and as they strengthen interleaving could dominate. Yet the parameterization schemes will allow the transition to be smooth between the two sources of diapycnal mixing and this may be inappropriate. A parameterization scheme which encompasses both mechanisms may solve this problem.

Finally, while all previous experiments dealt with the role of mixing in the steady state, our final experiment also established that both vertical and lateral mixing appear to play a role in the response of the ocean to a WWB. Lateral mixing is a dominant contribution only below the surface layer but is one of the factors controlling the strength not only of the EUC but also the SSRC. In particular, the reduction in the magnitude of lateral mixing, to be replaced by turbulent mixing, enhanced the SSRC. This leads us to suggest (tentatively) that prescribing the mixing based on the physical processes taking place may have profound effects not just on the steady state but also on the transients of the system, which are of utmost importance when predicting climatic events such as ENSO.

Chapter 5

Conclusions

5.1 Summary and major findings

This thesis has focussed on intrusive features in the Western Equatorial Pacific and the role of mixing on the large-scale circulation of the Equatorial Pacific. This encompassed describing the characteristics of the intrusions and understanding the mechanism producing the features. In addition, we prescribed the representation of the sub-grid scale fluxes produced by intrusive features (which are not explicitly resolved by the grid scale in numerical models) and addressed the importance of these fluxes compared to mesoscale eddy fluxes. Further, we developed intuition into the effect this parameterization has on the large-scale dynamics in a simplified model of the Equatorial Pacific. We now summarize the major results from each chapter and synthesize the results to discuss their wider implications.

5.1.1 The characteristics and mechanism of intrusions

In chapter 2, the intrusive features in the thermocline of the Western Equatorial Pacific were documented extensively. The features have vertical scales O(20m), meridional scales O(>30km) and zonal scales O(100km) and slope both upward and downward across isopycnals. The evidence from the spice anomaly, density anomaly, Turner angle and temperature-salinity ratio is consistent with a mechanism of double-diffusive interleaving producing approximately fifty per cent of the observed features with the diffusive interface dominating the features. Those features which are clearly not produced by this mechanism may be the result of advection and baroclinic instability. Our results extend the work of Toole (1981a), McPhaden (1985) and Richards (1991) and in particular provide details of the observations to motivate further theoretical work. We propose that the intrusive features may have their origins in the Western Equatorial Pacific and be advected downstream by

the Equatorial Undercurrent (EUC). If this statement is true, then by the time layers reach the Eastern Equatorial Pacific, they may be distorted due to the presence of meridional shear in the EUC. Combining the results of this analysis with those of Toole (1981a), who suggested that approximately 30 % of the observed features in the Eastern Equatorial Pacific were consistent with double-diffusive interleaving, one might conclude that such a distortion (or a subsequent instability) of the features takes place. There exists a need to attribute the remaining features to a possible mechanism and to describe the downstream evolution of the features. This calls for work to continue on instability processes in the vicinity of the Equator. A major problem confounding progress for observationalists is the difficulty in identifying the signal associated with different mechanisms. Indeed that we have identified structures consistent with double-diffusive interleaving is a major step forward.

5.1.2 Parameterization of intrusive features

In chapter 3, we compared the fluxes of heat and salt produced by interleaving with the fluxes produced by other mechanisms, as estimated from a mooring array. The fluxes are of the same order of magnitude and give a diffusion coefficient $O(10^3\ m^2\ s^{-1})$. This value is significant in large-scale models of the Equatorial ocean. Which processes should be represented by sub-grid scale parameterizations? We have argued that while processes such as mesoscale eddies, baroclinic instability and advective effects may be explicitly represented with sufficient grid resolution, producing the resolution required to explicitly represent double-diffusive interleaving is not, at present, a feasible prospect for large-scale models. Therefore the fluxes produced by this mechanism must be parameterized. We have developed a parameterization scheme for double-diffusive interleaving based on three assumptions. These assumptions are:

- double-diffusive interleaving acts in a 'diffusive' (rather than 'advective') manner on the large-scale tracer fields.
- linear stability theory can be used to prescribe the functional form of the relevant scales.
- the perturbation salinity and temperature of a feature can be related to the large-scale cross-frontal gradients.

The parameterization predicts that the functional form of the lateral diffusion coefficient, A_H:

$$A_H \sim (N S_y)^{\frac{1}{2}}$$

i.e. the lateral diffusion coefficient is proportional to both the large-scale lateral salinity gradient and the buoyancy frequency. Intrusions slope across isopycnals which also suggests that there is a diapycnal component to the fluxes. No previous authors have attempted to parameterize the lateral diffusion coefficient due to interleaving. In particular, in the implementation of the scheme we have been able to incorporate both the diapycnal and isopycnal components of the mixing and still allow background turbulent mixing. Simultaneous measurements of turbulence and thermohaline finestructure would be helpful in determining how double-diffusive interleaving and turbulence interact. Ideally, the parameterization scheme for double-diffusive interleaving should be flexible enough to allow turbulent mixing to take place and eddies to form (with sufficient horizontal grid resolution) when the interleaving is weak. On the other hand, when the conditions for interleaving prevail (i.e. stratification and the salinity gradient are strong) interleaving should be allowed to dominate.

5.1.3 Large-scale modelling of the Equatorial Ocean

In chapter 4, we performed experiments to determine the effect of mixing due to intrusive features on the large-scale structure of the Equatorial ocean. A large amount of preliminary work was devoted to the development of a suitable model for these experiments. The model was a two-dimensional meridional-vertical section forced by an easterly wind stress and balanced by a prescribed eastward zonal pressure gradient.

The major results from the experiments can be summarized:

- the geodesic lateral diffusion of temperature (or density) is the major control on the magnitude of the upwelling and the stratification of the thermocline.
- the strength of the EUC is directly controlled by the lateral diffusion of momentum (at least in this two-dimensional model) with the geodesic lateral diffusion of temperature playing a secondary role (possibly via the potential vorticity).
- the heat-salt flux ratio (even of vertical diffusion) plays an almost negligible role in setting the dynamics.

- diffusing tracers (heat and salt) along isopycnals leads to a sharper thermocline and a faster EUC. The EUC is influenced only by the diapycnal component of mixing. However, the model does reproduce the interplay between isopycnal and diapycnal mixing reported by Maes et al. (1996).

- prescribing the functional form of the lateral diffusion coefficient (geodesically and isopycnally) alters both the large-scale structure of the temperature and salinity fields and the dynamics. The upwelling cell is now confined more closely to the Equator, SST is reduced by O(1 $^{\circ}$ C) and the strength of the EUC is increased by O(10%).

- prescribing the cross-isopycnal component of the intrusive mixing can lead to asymmetry in the Equatorial circulation and alter the diagnostics significantly.

- lateral mixing also plays a role in determining the transients of the system via its interaction with vertical mixing and vertical advection.

The implications of these results for GCMs of the Equatorial Ocean are diverse. At the simplest level the experiments in Prandtl number space for lateral diffusion suggest that models might be 'tuned' to produce the 'correct' upwelling and EUC strength. Although this approach may not be entirely scientific, it may be useful in correcting some anomalous features of the present models. Our experiments suggest very strongly that lateral diffusion of tracers and momentum are linked to different aspects of the circulation. The applicability of these results to three-dimensional models could be easily checked by extending the experiments of Maes et al. (1996) to Prandtl numbers greater and less than one. At a higher level of sophistication, the intrusion parameterization appears to be effective at changing the circulation pattern and SST. The consequences for models used for ENSO prediction needs to be explored.

5.1.4 Synthesis of results

Can we put these results into a wider perspective? The modelling results of chapter 4 confirm that the prescription of the sub-grid scale fluxes is highly influential on the large-scale circulation of the Equatorial Pacific, in particular on the diagnostics used by Equatorial modellers. It is crucial that these fluxes are prescribed on the basis of the observed physical processes which are taking place, rather than hypothesized processes. We found evidence which supported double-diffusive interleaving as one of the mechanisms producing in-

trusive features (and therefore mixing heat and salt) in the thermocline and proposed a parameterization scheme for the fluxes due to the process, which are as large as mesoscale eddy fluxes. Implementing the proposed scheme rather than constant horizontal diffusion is an intellectual step forward and has some influence on the horizontal and vertical structure of our simplified Equatorial ocean. Future work implementing the parameterization in an Equatorial OGCM could quantify the flexibility of the scheme in regimes where interleaving is both weak and intense. Our parameterization may (with an amendment to the horizontal scale) be useful in other frontal regions where double-diffusive interleaving has been observed (for example, Antarctic Polar front (Joyce et al. 1978)).

5.2 Future work

While the work undertaken here has addressed certain issues, there are many issues outstanding. The most obvious of these are listed here:

- What is the precise role of advection and baroclinic instability in the production of intrusive features?
- Does the 'diffusive' parameterization assumed in this thesis capture the physics of the intrusive features?
- Does the intrusive parameterization influence the diagnostics employed by three-dimensional models used to simulate the Equatorial ocean and predict ENSO?

Further analysis of the available datasets in the Equatorial Pacific might shed further light on the first two questions. However, the present datasets combine temporal and spatial variability. Further theoretical and modelling work would be a more appropriate starting point. The proposal of Richards (1995) suggests the use of a high resolution non-hydrostatic model in a two-dimensional plane (similar to the model employed in chapter 4). By parameterizing the double-diffusive interface fluxes in the manner of Walsh and Ruddick (1996), it will be possible to model double-diffusive intrusions. Double-diffusive intrusions at finite amplitude with non-linearities included could be examined. To establish the exact role of baroclinic instability, internal waves and turbulence we suggest that a series of experiments could be performed in different regimes of parameter space. The results of these experiments will be useful in suggesting the characteristics of various mechanisms and their interactions. This may lead to a reanalysis of the datasets. It should also be

possible to establish whether the features are predominantly diffusive or advective in their effects on the large-scale structure. This could be done by comparing the fields produced by the high resolution experiments with those produced by different schemes implemented in a low resolution model (e.g. the model of chapter 4), in a similar manner to the work of Visbeck et al. (1996).

The only way to establish the effect of the proposed parameterization scheme on the three-dimensional circulation is to implement it in a General Circulation Model (GCM). This work is planned in collaboration with the Delecluse team at LODYC (allowing direct comparison with the results of Maes et al. (1996)) and the results will be reported elsewhere.

The possibility exists to make significant headway in the representation of intrusions in the Equatorial Pacific in GCMs and possibly to extend the results to encompass other regions of the ocean. While this thesis has not by any means completed this difficult task, we believe that the work presented here has made a significant contribution which others can extend.

Appendix A

Numerical Model

A.1 Finite difference equations

The variables $(u, v, w, \theta, S, \rho, P)$ are discrete functions of the (t, y, z). The subscripts j, k indicate the meridional and vertical position of each variable and the superscript n indicates the time.

The grid used for the finite difference equations is the B-grid. This grid is shown schematically in figure A.1. The tracer (T, S, ρ) and velocity (u, v) points are offset to the left, while the vertical velocity points associated with the tracer (wt) and velocity (wv) are offset upwards. The vertical separation is denoted by Δz, the meridional separation by Δy and the timestep by Δt.

A.1.1 Vertical velocities

The continuity equation:

$$\frac{\partial v}{\partial y} + \frac{\partial w}{\partial z} = 0 \tag{A.1}$$

can be written in finite difference form to give the vertical velocity, wv:

$$\frac{wv_{j,k+1} - wv_{j,k}}{\Delta z} = \frac{v_{j+1,k} - v_{j-1,k}}{2\Delta y} \tag{A.2}$$

and the vertical velocity, wt:

$$\frac{wt_{j,k+1} - wt_{j,k}}{\Delta z} = \frac{v_{j,k} - v_{j-1,k}}{2\Delta y}. \tag{A.3}$$

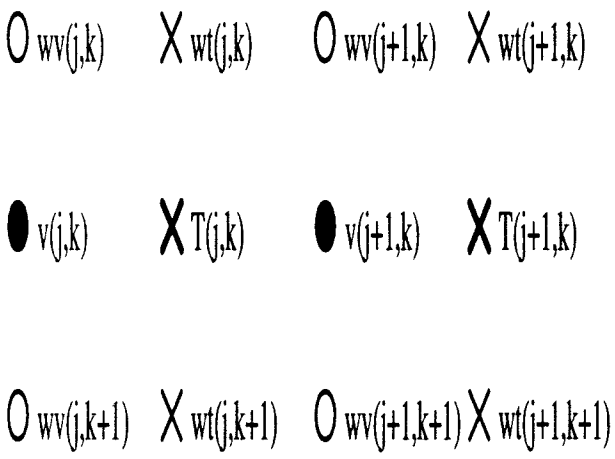

Figure A.1: Schematic of the model grid.

A.1.2 Momentum equations

The equation for the zonal velocity is given by:

$$\frac{\partial u}{\partial t} + v\frac{\partial u}{\partial y} + w\frac{\partial u}{\partial z} - \beta yv = -\frac{\partial P}{\partial x} + \frac{\partial}{\partial z}(K_v\frac{\partial u}{\partial z}) + \frac{\partial}{\partial y}(K_h\frac{\partial u}{\partial y}) \tag{A.4}$$

$$\frac{\partial v}{\partial t} + v\frac{\partial v}{\partial y} + w\frac{\partial v}{\partial z} + \beta yu = -\frac{\partial P}{\partial y} + \frac{\partial}{\partial z}(K_v\frac{\partial v}{\partial z}) + \frac{\partial}{\partial y}(K_h\frac{\partial v}{\partial y}). \tag{A.5}$$

We will consider each of the terms independently.

Acceleration terms

The acceleration terms are represented in the finite difference form as:

$$\frac{u' - u^m}{(n+1-m)\Delta t} \tag{A.6}$$

$$\frac{v' - v^m}{(n+1-m)\Delta t} \tag{A.7}$$

where m denotes the 'old' timestep (in the leapfrog scheme m is $n-1$ except for every tenth step when it is given by n) and u', v' contribute towards the solution at time $n+1$.

Then at timestep $n+1$,

$$u^{n+1} = u'$$

and

$$v^{n+1} = v' - \overline{v}'$$

with the barotropic velocity subtracted from the meridional velocity to ensure no net meridional flow.

Advection terms

Using the continuity equation, we can represent the advective terms as:

$$\frac{\partial uv}{\partial y} + \frac{\partial uw}{\partial z} \tag{A.8}$$

$$\frac{\partial vv}{\partial y} + \frac{\partial vw}{\partial z} \tag{A.9}$$

and the finite difference form becomes:

$$\frac{(v_{j+1,k} + v_{j,k})(u_{j+1,k} + u_{j,k}) - (v_{j,k} + v_{j-1,k})(u_{j,k} + u_{j-1,k})}{4\Delta y} + \frac{wv_{j,k}(u_{j,k-1} + u_{j,k}) - wv_{j,k+1}(u_{j,k} + u_{j,k+1})}{2\Delta z} \tag{A.10}$$

$$\frac{(v_{j+1,k} + v_{j,k})(v_{j+1,k} + v_{j,k}) - (v_{j,k} + v_{j-1,k})(v_{j,k} + v_{j-1,k})}{4\Delta y} + \frac{wv_{j,k}(v_{j,k-1} + v_{j,k}) - wv_{j,k+1}(v_{j,k} + v_{j,k+1})}{2\Delta z} \tag{A.11}$$

where all velocities are defined at timestep n.

Coriolis terms

The Coriolis terms are dealt with semi-implicitly and given by:

$$-\beta y \alpha u' - \beta y(1-\alpha)u^m \tag{A.12}$$

$$\beta y \alpha v' + \beta y(1-\alpha)v^m \tag{A.13}$$

where α is chosen to be 0.55.

Pressure gradient

The zonal pressure gradient, P_x, is prescribed. The meridional pressure gradient, P_y, is calculated via the hydrostatic approximation:

$$\frac{\partial P}{\partial y} = -\frac{g}{\rho_o}\int_z^0 \frac{\partial \rho}{\partial y} dz. \tag{A.14}$$

At the level k=1 this is given by:

$$\frac{\partial P_{j,1}}{\partial y} = -\frac{g\Delta z(\rho_{j+1,1} - \rho_{j,1})}{2\Delta y \rho_o} \tag{A.15}$$

and at other levels k by:

$$\frac{\partial P_{j,k}}{\partial y} = \frac{\partial P_{j,k-1}}{\partial y} - \frac{g\Delta z(\rho_{j+1,k-1} + \rho_{j+1,k} - \rho_{j,k-1} - \rho_{j,k})}{2\Delta y \rho_o}. \tag{A.16}$$

Mixing terms

The finite difference form of the mixing (or diffusion) terms is given by:

$$\begin{aligned}
&\frac{1}{\Delta z^2}(K_{vj,k-\frac{1}{2}}(u_{j,k-1} - u_{j,k}) - K_{vj,k+\frac{1}{2}}(u_{j,k} - u_{j,k+1}) + \\
&\quad \frac{1}{\Delta y^2}(K_{hj+\frac{1}{2},k}(u_{j+1,k} - u_{j,k}) - K_{hj-\frac{1}{2},k}(u_{j,k} - u_{j-1,k})
\end{aligned} \tag{A.17}$$

$$\begin{aligned}
&\frac{1}{\Delta z^2}(K_{vj,k+\frac{1}{2}}(v_{j,k-1} - v_{j,k}) - K_{vj,k+\frac{1}{2}}(v_{j,k} - v_{j,k+1}) + \\
&\quad \frac{1}{\Delta y^2}(K_{hj+\frac{1}{2},k}(v_{j+1,k} - v_{j,k}) - K_{hj-\frac{1}{2},k}(v_{j,k} - v_{j-1,k})
\end{aligned} \tag{A.18}$$

where all velocities are determined at timestep m.

A.1.3 Tracer equations

The conservation equation for temperature is given by:

$$\frac{\partial \theta}{\partial t} + u\frac{\partial \theta}{\partial x} + v\frac{\partial \theta}{\partial y} + w\frac{\partial \theta}{\partial z} = \frac{\partial}{\partial z}A_v\frac{\partial \theta}{\partial z} + \frac{\partial}{\partial y}A_h\frac{\partial \theta}{\partial y} \tag{A.19}$$

with the same equation applying for salinity with S replacing θ.

Tendency terms

The finite difference form of the tendency equation is:

$$\frac{\theta^{n+1} - \theta^m}{(n+1-m)\Delta t} \tag{A.20}$$

where m is defined as before.

Advection terms

The finite difference form of the advection terms are:

$$\begin{aligned} &\frac{1}{2}(u_{j-1,k}\frac{\partial\theta_{j-1,k}}{\partial x} + u_{j,k}\frac{\partial\theta_{j,k}}{\partial x}) + \\ &\frac{1}{2\Delta y}(v_{j,k}(\theta_{j+1,k} - \theta_{j,k}) + v_{j-1,k}(\theta_{j,k-1} - \theta_{j,k})) + \\ &\frac{1}{2\Delta z}(wt_{j,k}(\theta_{j,k-1} - \theta_{j,k}) + wt_{j,k+1}(\theta_{j,k} - \theta_{j,k+1})) \end{aligned} \tag{A.21}$$

where the tracer and velocity terms are defined at timestep n.

Mixing terms

The mixing (or diffusion) of tracers is given in finite difference form as:

$$\begin{aligned} &\frac{1}{\Delta z^2}(A_{vj,k-\frac{1}{2}}(\theta_{j,k-1} - \theta_{j,k}) - A_{vj,k+\frac{1}{2}}(\theta_{j,k} - \theta_{j,k+1})) + \\ &\frac{1}{\Delta y^2}(A_{hj+\frac{1}{2},k}(\theta_{j+1,k} - \theta_{j,k}) - A_{hj-\frac{1}{2},k}(\theta_{j,k} - \theta_{j-1,k})) \end{aligned} \tag{A.22}$$

where the tracer terms are defined at timestep m.

A.1.4 Stability criteria

There are three stability criteria to be fulfilled which we address:

1. the semi-implicit calculation of the Coriolis term requires that $\alpha > 0.5$ (Mesinger and Arakawa 1976). This is satisfied since we set α to be 0.55.

2. the advection terms have a stability criteria given by:

$$\Delta t \leq \frac{1}{\frac{v}{\Delta y} + \frac{w}{\Delta z}}$$

which gives a fairly weak constraint on the timestep (on the order of days).

3. the diffusion terms have a stability criteria given by:

$$\Delta t \leq \frac{1}{\frac{4K_h}{\Delta y^2} + \frac{4K_v}{\Delta z^2}}$$

which constrains the timestep to be less than one hour.

A.2 Convective parameterisation

The convective scheme implemented in the model is the convective adjustment scheme of Yin and Sarachik (1994). The scheme is explicit and guarantees the removal of static instability in the water column in one iteration.

The method can be broken down into four steps. These are summarised below.

- The total number (N) of unstable vertical regions and the beginning (b_n) and end (e_n) index of each region n ($n = 1, N$) are identified. This is acheived by comparing the density of adjacent points.
- Within each unstable region the new (mean) temperature and salinity values are calculated. If necessary the region is extended until it is marginally stable relative to the regions above and below (this is done by recalculating the means with the extra points included).
- If two regions overlap, then if one is contained by the other, the one with the smaller vertical extent is discarded, while if they partially overlap then the new region contains both the regions and temperature, salinity and density are mixed between the two.
- The adjustment is completed. Within the regions, the temperature and salinity are the calculated values while outside the regions they are the existing values.

A.3 Isopycnal mixing

When the mixing is prescribed along isopycnals the model equations become:

$$\frac{\partial}{\partial l}(A_i\frac{\partial \tau}{\partial l}) + \frac{\partial}{\partial n}(A_d\frac{\partial \tau}{\partial n}) = \frac{\partial}{\partial y}(A_i\frac{\partial \tau}{\partial y} - \delta A_i\frac{\partial \tau}{\partial z}) + \frac{\partial}{\partial z}((A_d + \delta^2 A_i)\frac{\partial \tau}{\partial z} - \delta A_i\frac{\partial \tau}{\partial y}).$$

where $\delta = \rho_y/\rho_z$. We evaluate $\delta_{j,k}Ai_{j,k}$ at the Ah points (velocity points) and at the Av points (the tracer vertical velocity points) and ${\delta_{j,k}}^2 Ai_{j,k}$ at the Av points (the tracer vertical velocity points).

Then the finite difference form of the above expression is given by:

$$
\begin{aligned}
&Ai_{j+\frac{1}{2},k}\left(\frac{T_{j+1,k}-T_{j,k}}{\Delta y^2}\right) - Ai_{j-\frac{1}{2},k}\left(\frac{T_{j,k}-T_{j-1,k}}{\Delta y^2}\right) + \\
&(\delta Ai)_{j+\frac{1}{2},k}\left(\frac{T_{j+1,k-1}+T_{j,k-1}-T_{j+1,k+1}-T_{j,k+1}}{4\Delta y\Delta z}\right) - \\
&(\delta Ai)_{j-\frac{1}{2},k}\left(\frac{T_{j-1,k-1}+T_{j,k-1}-T_{j-1,k+1}-T_{j,k+1}}{4\Delta y\Delta z}\right) + \\
&(\delta Ai)_{j,k-\frac{1}{2}}\left(\frac{T_{j+1,k-1}+T_{j+1,k}-T_{j-1,k-1}-T_{j-1,k}}{4\Delta y\Delta z}\right) - \\
&(\delta Ai)_{j,k+\frac{1}{2}}\left(\frac{T_{j+1,k+1}+T_{j+1,k}-T_{j-1,k+1}-T_{j-1,k}}{4\Delta y\Delta z}\right) + \\
&(\delta^2 Ai)_{j,k-\frac{1}{2}}\left(\frac{T_{j,k-1}-T_{j,k}}{\Delta z^2}\right) - (\delta^2 Ai)_{j,k+\frac{1}{2}}\left(\frac{T_{j,k}-T_{j,k+1}}{\Delta z^2}\right).
\end{aligned}
$$

The stability constraints limit the isopycnal slope, δ, to be less than 10^{-2} when the vertical component of the mixing is evaluated implicitly (Cox 1987). This is done by solving a tridiagonal matrix (Richtmyer and Morton 1967). The boundary conditions are given as $\partial/\partial z = 0$, except for the diapycnal component of Ad which is given as the Haney boundary condition.

References

Armi, L., D. Hebert, N. Oakey, J. Price, P. Richardson, T. Rossby and B. Ruddick, 1989: Two years in the life of a mediterranean salt lens, *Journal of Physical Oceanography*, **19**, 354–370.

Barton, E. D., and P. Hughes, 1982: Variability of water mass interleaving off n.w. africa, *Journal of Marine Research*, **40**, 963–984.

Baumgartner, A., and E. Reichel, 1975: *The World Water Balance*, p. 179, Elsevier.

Blanke, B., and P. Delecluse, 1993: Variability of the tropical atlantic ocean simulated by a general circulation model with two different mixed layer physics, *Journal of Physical Oceanography*, **23**, 1363–1388.

Brady, E. C., 1990: Observations of wave-mean flow interaction in the pacific equatorial undercurrent, Ph.D. thesis, MIT/WHOI.

Bryden, H. L., and E. C. Brady, 1985: Diagnostic model of the three-dimensional circulation in the upper equatorial pacific ocean, *Journal of Physical Oceanography*, **15**, 1255–1273.

Bryden, H. L., and E. C. Brady, 1989: Eddy momentum and heat fluxes and their effects on the circulation of the equatorial pacific ocean, *Journal of Marine Research*, **47**, 55–79.

Calman, J., 1977: Experiments on high richardson number instability of a rotating stratified shear flow, *Dynamics of Atmosphere and Oceans*, **1**, 277–297.

Chen, D., L. M. Rothstein and A. J. Busalacchi, 1994: A hybrid vertical mixing scheme and its application to tropical ocean models, *Journal of Physical Oceanography*, **24**, 2156–2179.

Cherubin, L., D. G. Dritschel and X. J. Carton, 1996: Stability of the mediterranean undercurrent on the iberian shelf and canyons in the gulf of cadiz, *Annales Geophysicae*, **14**, C411.

Cox, M. D., 1980: Generation and propogation of 30-day waves in a numerical model of the pacific, *Journal of Physical Oceanography*, **10**, 1168–1186.

Cox, M. D., 1987: Isopycnal diffusion in a z-coordinate model, *Ocean Modelling*, **74**, 1–5.

Crawford, W. R., 1982: Pacific equatorial turbulence, *Journal of Physical Oceanography*, **12**, 1137–1149.

Davies, R., 1976: Predictability of sea surface temperature and sea level pressure anomalies over the north pacific ocean, *Journal of Physical Oceanography*, **6**, 249–266.

Davis, R. E., P. D. Killworth and J. R. Blundell, 1996: Comparison of autonomous lagrangian circulation explorer and fine resolution antarctic model results in the south atlantic, *Journal of Geophysical Research*, **101**, 855–884.

Eckart, C., 1948: An analysis of the stirring and mixing processes in incompressible fluids, *Journal of Marine Research*, **7**, 265–275.

Eldin, G., T. Delcroix, C. Henin, K. J. Richards, Y. du Penhoat, J. Picaut and P. Rual, 1994: Large-scale current and thermohaline structures along 156°e during the coare iop, *Geophysical Research Letters*, **21**, 2681–2684.

Fofonoff, N. P., and R. B. Montgomery, 1955: The equatorial undercurrent in light of the vorticity equation, *Tellus*, **7**, 518–521.

Friedrich, H., and S. Levitus, 1972: An approximation to the equation of state for sea water, suitable for numerical ocean models, *Journal of Physical Oceanography*, **2**, 514.

Gargett, A., 1984: Vertical eddy diffusivity in the ocean interior, *Journal of Marine Research*, **42**, 359–393.

Gargett, A. E., and G. Holloway, 1992: Sensitivity of the gfdl model to different diffusivities for heat and salt, *Journal of Physical Oceanography*, **22**, 1158–1177.

Garrett, C., 1982: On the parameterization of diapycnal fluxes due to double-diffusive intrusions, *Journal of Physical Oceanography*, **12**, 952–959.

Gent, P. R., and J. C. McWilliams, 1990: Isopycnal mixing in ocean circulation models, *Journal of Physical Oceanography*, **20**, 150–155.

Gouriou, Y., and J. Toole, 1993: Mean circulation of the upper layers of the western equatorial pacific ocean, *Journal of Geophysical Research*, **98**, 22,495–22,520.

Graham, A., and A. J. Hall, 1996: The horizontal distribution of bubbles in a shallow sea, *Continental Shelf Research*.

Green, J. A., 1970: Transfer properties of the large-scale eddies and the general circulation of the atmosphere, *Quarterly Journal of the Royal Meteorological Society*, **96**, 157–185.

Gregg, M. C., 1980: The three-dimensional mapping of a small thermohaline intrusion, *Journal of Physical Oceanography*, **12**, 954–959.
Gregg, M. C., H. Peters, J. C. Wesson, N. S. Oakey and T. J. Shay, 1985: Intensive measurements of turbulence and shear in the equatorial undercurrent, *Nature*, **318**, 140–144.
Haney, R. H., 1971: Surface thermal boundary conditions for ocean circulation models, *Journal of Physical Oceanography*, **1**, 241–248.
Harrison, D. E., 1978: On the diffusion parameterization of mesoscale eddy effects from a numerical ocean experiment, *Journal of Physical Oceanography*, **8**, 913–918.
Harvey, L. D. D., 1995: Impact of isopycnal diffusion on heat fluxes and the transient response of two-dimensional ocean model, *Journal of Physical Oceanography*, **25**, 2166–2176.
Hebert, D., 1988: A mediterranean salt lens, Ph.D. thesis, Dalhousie University, Halifax, Nova Scotia.
Hisard, H., and J. Merle, 1970: The equatorial undercurrent at 170°e in march and april 1967, *Journal of Marine Research*, **28**, 281–303.
Jackett, D. R., and T. J. McDougall, 1985: An oceanographic variable for characterisation of intrusions and water masses, *Deep-Sea Research*, **32**, 1195–1207.
Johnson, E. S., and M. J. McPhaden, 1993: Effects of a three-dimensional mean flow on intraseasonal kelvin waves in the equatorial pacific ocean, *Journal of Geophysical Research*, **98**, 10185–10194.
Joyce, T. M., 1977: A note on lateral mixing of water masses, *Journal of Physical Oceanography*, **7**, 626–629.
Joyce, T. M., W. Zenk and J. M. Toole, 1978: The anatomy of the antarctic polar front in the drake passage, *Journal of Geophysical Research*, **83**, 6093–6113.
Killworth, P. D., 1991: Cross-equatorial geostrophic adjustment, *Journal of Physical Oceanography*, **21**, 1581–1601.
Kraus, E. B., and J. S. Turner, 1967: A one-dimensional model of the seasonal thermocline. ii: The general theory and its consequences, *Tellus*, **19**, 98–105.
Kuz'mina, N. P., 1990: Vertical scales for thermohaline intrusions in the ocean, *Oceanology*, **30**, 534–538.
Kuz'mina, N. P., and V. B. . Rodionov, 1992: Influence of baroclinicity on formation of thermohaline intrusions in ocean frontal zones, *Izvestiya, Atmospheric and Oceanic Physics*, **28**, 804–810.
Legeckis, R., 1977: Long waves in the eastern equatorial pacific ocean: A view from a geostationary satellite, *Science*, **197**, 1179–1181.
Linden, P. F., 1971: Salt fingers in the presence of grid-generated turbulence, *Journal of Fluid Mechanics*, **49**, 611–624.
Lukas, R., 1987: Horizontal reynolds stresses in the central equatorial pacific, *Journal of Geophysical Research*, **92**, 9453–9463.
Maes, C., G. Madec and P. Delecluse, 1996: Sensitivity of an equatorial pacific ogcm to the lateral diffusion coefficient, Monthly Weather Review, in press.
Mangum, L. J., S. P. Hayes, J. M. Toole, Z. Wang, S. Pu and D. Hu, 1990: Thermohaline structure and zonal pressure gradient in the western equatorial pacific, *Journal of Geophysical Research*, **95**, 7279–7288.
McCreary, J. P., and D. L. T. Anderson, 1991: An overview of coupled ocean-atmosphere models of El Niño and the southern oscillation, *Journal of Geophysical Research*, **96**, 3125–3130.
McDougall, T. J., 1985a: Double-diffusive interleaving. part i: linear stability analysis, *Journal of Physical Oceanography*, **15**, 1532–1541.
McDougall, T. J., 1985b: Double-diffusive interleaving. part ii: finite, amplitude , steady state interleaving, *Journal of Physical Oceanography*, **15**, 1542–1556.
McDougall, T. J., 1986: Oceanic intrusions: some limitations of the ruddick and turner(1979) mechanism, *Deep-Sea Research*, **33**, 1653–1664.
McIntyre, M. E., 1970: Diffusive destablisation of the baroclinic circular vortex, *Geophysical Fluid Dynamics*, **1**, 19–57.
McPhaden, M. J., 1985: Fine-structure variability observed in ctd measurements from the central equatorial pacific, *Journal of Geophysical Research*, **90**, 11,726 – 11,740.
McPhaden, M. J., 1993: Toga-tao and the 1991-93 El Niño -southern oscillation event, *Oceanography*,

6, 36–44.

McPhaden, M. J., H. P. Freitag, S. P. Hayes, B. Taft, Z. Chen and K. Wyrtki, 1988: The response of the equatorial pacific to a westerly wind burst in may 1986, *Journal of Geophysical Research*, **93**, 10589–10603.

McPhaden, M. J., S. P. Hayes and L. J. Mangum, 1990: Variability in the western equatorial pacific ocean during the 1986–1987 El Niño /southern oscillation event, *Journal of Physical Oceanography*, **20**, 190–208.

Mesinger, F., and A. Arakawa, 1976: Numerical methods used in atmospheric models, *Tech. rep.*, WMO/ICSU Joint organising committee, GARP Publications series No. 17, 64pp.

Miller, L., R. E. Cheney and B. C. Douglas, 1988: Geosat altimeter observations of kelvin waves and the 1986-1987 El Niño , *Science*, **239**, 52–54.

Moum, J. N., et al., 1989: Mixing in the equatorial surface layer and thermocline, *Journal of Geophysical Research*, **94**, 2005–2021.

Munk, W. H., and E. R. Anderson, 1948: Notes on a theory of the thermocline, *Journal of Marine Research*, **7**, 276–295.

Neelin, J. D., et al., 1992: Tropical air-sea interaction in general circulation models, *Climate Dynamics*, **7**, 73–104.

Niino, H., 1986: A linear stability theory of double-diffusive horizontal intrusions in a temperature-salinity front, *Journal of Fluid Mechanics*, **171**, 71–100.

Onken, R., J. Fischer and J. D. Woods, 1990: Thermohaline finestructure and its relation to frontogenesis dynamics, *Journal of Physical Oceanography*, **20**, 1379–1394.

Pacanowski, R., and S. G. H. Philander, 1981: Parameterisation of vertical mixing in numerical models of tropical oceans, *Journal of Physical Oceanography*, **11**, 1443–1451.

Parr, A. E., 1936: On the probable relationship between vertical stability and lateral mixing processes, *J. Cons. Int. Explor. Mer.*, **11**, 308–313.

Peters, H., M. C. Gregg and J. M. Toole, 1988: On the parameterisation of equatorial turbulence, *Journal of Geophysical Research*, **93**, 1199–1218.

Philander, S. G., 1990: *El Niño , La Niña and the Southern Oscillation*, p. 290, Academic Press, inc.

Philander, S. G. H., and R. C. Pacanowski, 1980: The generation of equatorial currents, *Journal of Geophysical Research*, **85**, 1123–1136.

Price, J. F., R. A. Weller and R. Pinkel, 1986: Diurnal cycling: observations and models of the upper ocean response to diurnal heating, cooling and wind mixing, *Journal of Geophysical Research*, **91**, 8411–8427.

Redi, M. H., 1982: Oceanic isopycnal mixing by coordinate rotation, *Journal of Physical Oceanography*, **12**, 308–313.

Reid, J. L., 1965: *Intermediate waters of the Pacific Ocean*, p. 85, Johns Hopkins Press.

Richards, K. J., 1991: Double-diffusive interleaving at the equator, *Journal of Physical Oceanography*, **21**, 933–938.

Richards, K. J., 1995: Interleaving in the equatorial pacific ocean and its effect on the largescale dynamics, NERC grant proposal.

Richards, K. J., et al., 1988: Rrs charles darwin cruise 32, 3 april - 2 may 1988. a study of the upper density and current structure of the western equatorial pacific, *Tech. rep.*, Southampton University, Department of Oceanography.

Richards, K. J., M. E. Inall and S. Keene, 1993: Coare–poi cruise report: Seasoar data collection, processing and calibration, *Tech. rep.*, University of Southampton, The University, Highfield, Southampton, UK.

Richards, K. J., and R. T. Pollard, 1991: Structure of the upper ocean in the western equatorial pacific, *Nature*, **350**, 48.

Richtmyer, R. D., and K. W. Morton, 1967: *Difference methods for initial value problems*, New York: Wiley-Interscience.

Rual, P., F. Gallois, R. Lukas, G. Muckenhaupt, L. Stratton and P. Verlaan, 1995: Rapport de la campagne coare 156-1 a bord du n. o. le noroit du 20 aout au 16 septembre 1991 de 20°s a 10°n le long du meridien 156°e et en mer du corail, *Tech. rep.*, Noumea: ORSTOM.

Ruddick, B., 1992: Intrusive mixing in a mediterranean salt lens: intrusion slopes and dynamical

mechanisms, *Journal of Physical Oceanography*, **22**, 1274–1285.
Ruddick, B. R., and D. Hebert, 1988: The mixing of meddy 'sharon', in *Small scale turbulence and mixing in the ocean*, edited by J. Nihoul, and B. Jamart, pp. 249–261, Elsevier, Amsterdam.
Ruddick, B. R., and J. S. Turner, 1979: The vertical length scale of double-diffusive intrusions, *Deep-Sea Research*, **26**, 903–913.
Ruddick, B. R., and D. Walsh, 1994: Observations of the density perturbations which drive thermohaline intrusions, in *Double-diffusive convection*, edited by A. Brandt, and H. J. S. Fernando, pp. 329–334, American Geophysical Union.
Schmitt, R. W., 1994: Double diffusion in oceanography, *Annual Review of Fluid Mechanics*, **26**, 255–285.
Schneider, N., and P. Müller, 1994: Sensitivity of the surface equatorial ocean to the parameterization of vertical mixing, *Journal of Physical Oceanography*, **24**, 1623–1640.
Schopf, P. S., and M. A. Cane, 1983: On equatorial dynamics, mixed layer physics and sea surface temperature, *Journal of Physical Oceanography*, **13**, 917–935.
Semtner, A. J., and W. R. Holland, 1980: Numerical simulation of equatorial circulation. part i: A basic case in turbulent equilibrium, *Journal of Physical Oceanography*, **10**, 667–693.
Stern, M. E., 1967: Lateral mixing of water masses, *Deep-Sea Research*, **14**, 747–753.
Stockdale, T., D. Anderson, M. Davey, P. Delecluse, A. Kattenberg, Y. Kitamura, M. Latif and T. Yamagata, 1993: Intercomparison of tropical pacific ocean gcm's, *WCRP 79, WMO/TD-545,43pp.*
Stommel, H., and N. K. Federov, 1967: Small scale structure in temperature and salinity near timor and mindinao, *Tellus*, **19**, 306–325.
Stone, P., 1972: Baroclinic instability under non-hydrostatic conditions, *Journal of Atmospheric Sciences*, **29**, 405–418.
Thorpe, S. A., P. K. Hutt and R. Soulsby, 1969: The effects of horizontal gradients on thermohaline convection, *Journal of Fluid Mechanics*, **38**, 375–400.
Toole, J. M., 1981a: Anomalous characteristics of equatorial thermohaline structure, *Journal of Physical Oceanography*, **11**, 871–876.
Toole, J. M., 1981b: Intrusion characteristics in the antarctic polar front, *Journal of Physical Oceanography*, **11**, 780–793.
Toole, J. M., and D. T. Georgi, 1981: On the dynamics and effects of double-diffusively driven intrusions, *Progress in Oceanography*, **10**, 123–145.
Tsuchiya, M., R. Lukas, R. A. Fine, E. Firing and E. Lindstrom, 1989: Source waters of the pacific equatorial undercurrent, *Progress in Oceanography*, **23**, 101–147.
Visbeck, M., J. Marshall, T. Haine and M. Spall, 1996: On the specification of eddy transfer coefficients in coarse resolution ocean circulation models, *Journal of Physical Oceanography*.
Wacongne, S., 1988: Dynamics of the equatorial undercurrent and its termination, Ph.D. thesis, MIT/WHOI.
Walsh, D., and B. Ruddick, 1995: Double-diffusive interleaving: the influence of non-constant diffusivities, *Journal of Physical Oceanography*, **25**, 348–358.
Walsh, D., and B. Ruddick, 1996: Nonlinear evolution of thermohaline intrusions, In preparation.
Wijffels, S. E., R. W. Schmitt, H. L. Bryden and A. Stigebrandt, 1992: Transport of freshwater by the oceans, *Journal of Physical Oceanography*, **22**, 155–162.
Williams, A. J., 1981: The role of double-diffusion in a gulf stream frontal intrusion, *Journal of Geophysical Research*, **86**, 1917–1928.
Woods, J. D., R. Onken and J. Fischer, 1986: Thermohaline intrusions created isopycnically at oceanic fronts are inclined to isopycnals, *Nature*, **322**, 446–449.
Wyrtki, K., and B. Kilonsky, 1984: Mean water and current structure during the hawaii to tahiti shuttle experiment, *Journal of Physical Oceanography*, **14**, 242–254.
Yin, F. L., and E. S. Sarachik, 1993: Dynamics and heat balance of steady equatorial undercurrents, *Journal of Physical Oceanography*, **23**, 1647–1669.
Yin, F. L., and E. S. Sarachik, 1994: An efficient convective adjustment scheme for ocean general circulation models, *Journal of Physical Oceanography*, **24**, 1425–1431.
Zhang, Q., 1995: The oceanic response to atmospheric forcing in the western equatorial pacific, Ph.D. thesis, University of Rhode Island.